

High-resolution observations of a complete sample of twenty-seven FR II radio galaxies and quasars with $0.3 < z < 0.6$

G. M. Gilbert,¹ J. M. Riley,^{1*} M. J. Hardcastle,² J. H. Croston,² G. G. Pooley,¹ and P. Alexander,¹

¹*Astrophysics Group, Cavendish Laboratory, Madingley Road, Cambridge, CB3 0HE*

²*Department of Physics, University of Bristol, Royal Fort, Tyndall Avenue, Bristol BS8 1TL*

Accepted 00 January 0000. Received 00 January 0000; in original form 16 March 2004

ABSTRACT

We present high-resolution VLA and MERLIN observations of the twenty-seven FR II radio galaxies and quasars with $0.3 < z < 0.6$ from the sample of Laing, Riley & Longair (1983). The jet detection rate is similar to that found in the lower-power, lower-redshift studies carried out using similar observing conditions. A wide range of lobe and hotspot structures is observed in both the radio galaxies and quasars in the sample. Interestingly, a high proportion of the quasars exhibit structures and asymmetries markedly different from those of the radio galaxies; this is difficult to explain using arguments based upon projection effects alone.

Key words: galaxies: active - radio continuum: jets - radio continuum; galaxies.

1 INTRODUCTION

Over the past ten years, in a series of papers (e.g. Black et al. 1992, hereafter B92; Leahy et al. 1997, hereafter L97; Hardcastle et al. 1997, hereafter H97), we have presented the results of a systematic programme to image samples of FR II (Fanaroff & Riley 1974) radio galaxies selected from the 3CR Catalogue (Bennett 1962; Spinrad et al. 1985) and from the complete sample of Laing, Riley & Longair (1983, hereafter LRL) with $z < 0.3$. These flux-limited samples are selected from a low-frequency (178 MHz) survey and so are largely free from orientation-dependent biases, provided that the lobe emission (by far the dominant contribution to the total source luminosity at a frequency of 178 MHz) is not relativistically beamed. The original aim of this programme was to study the detailed structure of the hotspots in FR II sources in order to understand the underlying physics of these regions; however, the presence of jets in many of the sources has allowed us, in addition, to investigate jet speeds and to test the predictions of unified models of radio sources.

The objects in the samples studied by B92 and L97 had $z < 0.15$ and were mainly low-power FR II sources. The high-resolution images showed a wide range of complex hotspot structures. These results contrasted with those of earlier studies of more luminous objects (e.g. Laing 1989; Perley 1989) which indicated that most hotspots were simple

entities with, at most, two components, a compact ‘primary’ hotspot and, in some cases, a diffuse ‘secondary’. Jets were detected in ~ 70 per cent of sources in contrast to previous observations of samples of FR II radio galaxies (e.g. Muxlow & Garrington 1991) in which relatively few were found. It was not clear, however, whether these differences in hotspot and jet properties were due to the proximity in power of the sources to the canonical FR I / II boundary ($P_{178} \sim 2 \times 10^{25}$ W Hz⁻¹ sr⁻¹) or to the higher quality and resolution of the observations.

These issues were addressed by H97 who imaged a sample with $0.15 < z < 0.3$. They confirmed the presence of multiple hotspots in these higher-power sources, and they also detected jets or possible jets in ~ 75 per cent of them.

Hardcastle et al. (1999) presented a statistical analysis of the data for all 50 sources with $z < 0.3$. They argued that the sample is intrinsically unbiased by the effects of relativistic beaming and used this to conclude that the prominence of the jets on kpc-scales can be explained using a simple relativistic beaming model. The results are consistent with a bulk jet speed of $\sim 0.6 - 0.7c$, and a very efficient jet with a kinetic power which is approximately proportional to the source luminosity.

In the work described here we extend the sample of H97 to larger redshifts. We have selected all 27 FR II radio galaxies and quasars in the LRL sample with $0.3 < z < 0.6$; the sources are listed in Table 1. This sample differs from that of B92, L97 and H97 not only in probing sources of higher lu-

* E-mail: julia@mrao.cam.ac.uk (JMR)

minosity, but also in including a significant number of quasars. Using a systematic observing strategy for all 27 objects allows direct and unbiased comparisons between the properties of radio galaxies and quasars. We can thus both examine the dependence of hotspot structure and jet prominence on source luminosity and test the extent to which the differences between radio galaxies and quasars can be explained in terms of relativistic beaming models. We can also compare our data with analytical models of radio sources (e.g. Kaiser & Alexander 1997, Komissarov & Falle 1998) and numerical simulations (e.g. Reynolds, Heinz & Begelman 2002, Saxton et al. 2002, Krause 2003). A programme with fairly similar aims has been carried out by Fernini, Burns & Perley (1997) and Fernini (2001, 2002) using two matched samples of quasars and galaxies from the 3CR sample. The most notable difference between our sample and theirs is that they have only included sources in the angular size range from 10 to 100 arcsec; they also consider some sources with $z > 0.6$.

In this paper we present the high-resolution images of the 27 sources in the sample. The observing strategy and the data reduction methods are discussed in Section 2. The images are presented in Section 3 and the structural characteristics of each source are discussed. The lobe, jet and hotspot properties of the sample are summarized in Section 4. The data will be analysed in conjunction with those from B92, L97 and H97 in later papers.

In common with B92, L97 and H97, throughout this paper we take $H_0 = 50 \text{ km s}^{-1} \text{ Mpc}^{-1}$ and $q_0 = 0$. Spectral index α is defined in the sense $S \propto \nu^{-\alpha}$. B1950 coordinates are used. Position angles are defined east of north.

2 OBSERVATIONS AND DATA REDUCTION

Observations of the sources in the sample were made using the VLA and, for those sources with largest angular size (LAS) less than 15 arcsec, MERLIN. Data at suitable frequencies and resolutions already existed for several sources and these were kindly made available to us by the observers, as indicated in Table 2.

2.1 VLA data

We adopted a VLA observing strategy similar to that described by H97. In general, the 8-GHz receivers were used, both for consistency with the results of H97 and because their high sensitivity makes them ideal for observations of this type. We observed each source using VLA configurations chosen both to sample the uv plane adequately on the shortest baselines necessary and to provide good resolution when mapping the detailed source structure. Consequently sources with largest angular sizes (LAS) less than 30 arcsec were not observed in the D configuration. Sources with LAS less than 15 arcsec were observed only in the A configuration and at 5 GHz; the longest baselines for these sources were provided by 5-GHz MERLIN observations. For a typical source in the sample we observed for 15 min at D array, 45 min at C array, 1 h at B array and 1.5 h at A array.

We required that bandwidth smearing should affect peak fluxes by less than 5 per cent. A bandwidth of 50 MHz (the largest bandwidth on the VLA) met this requirement

for all observations at C and D arrays. At B array a bandwidth of 50 MHz was used for all the sources with LAS less than 150 arcsec and of 25 MHz for the three sources with LAS greater than 150 arcsec. At A array we observed sources with LAS less than 45 arcsec with 50 MHz bandwidth, sources with sizes between 45 arcsec and 90 arcsec with 25 MHz bandwidth and the remainder with 12.5 MHz bandwidth. To obtain comparable sensitivity for all sources, we increased the observing time for those sources observed with a reduced bandwidth. The three largest sources in the sample (with LAS > 150 arcsec) were observed with three pointing centers, centered on the core and the northern and southern hotspots.

Because some of our data were provided by other observers, and for other reasons beyond our control, actual times on sources varied slightly from the plan in some cases, and four of the sources with LAS > 15 arcsec (3C 47, 3C 215, 3C 249.1 and 3C 334) were observed at 5 GHz rather than 8 GHz. For three sources (3C 299, 3C 334 and 3C 457) the shortest baselines used were insufficient to sample structure on the largest scales adequately.

Details of the VLA observations for each source in the sample are given in Table 2. The typical full resolution (FWHM of the restoring Gaussian) of the resulting images at 8 GHz is 0.25 arcsec, corresponding to a linear resolution of between 1.3 and 2 kpc for the sources in our sample. The typical off-source noise on the maps is $20 \mu\text{Jy beam}^{-1}$.

3C48 or 3C286 were observed as primary flux calibrators at the beginning and end of each observing run and a secondary phase calibrator was observed before and after a scan on each target source. For those observations with a scheduled on-source integration time greater than 30 minutes, two scans of each source were made; where possible the two scans were separated by a couple of hours so as to maximise the uv -coverage. One of the polarization position angle calibrators, 3C286 or 3C138, was also observed once during each run with additional observations of one of the secondary calibrators at a range of parallactic angles to allow polarization calibration.

The reduction of the VLA data was performed as described in H97 and B92 using the NRAO AIPS software and following standard procedures given in the AIPS Cookbook. For those sources observed at multiple pointing centres, data were combined in the image plane using the AIPS task L`TESS`.

2.2 MERLIN data

Details of the MERLIN observations are given in Table 3. The typical full resolution of the resulting images at 5 GHz is 0.05 arcsec, corresponding to a linear resolution of about 0.4 kpc for the sources in our sample.

3C286 was used as both a primary flux and polarization calibrator and, throughout the run, observations of the target source were frequently interleaved with those of a phase calibrator. The analysis of the MERLIN data followed standard procedures. After initial editing of bad samples, the data were imported into AIPS using a ‘pipeline’ process which applies the solutions derived from each of the calibrators to the target. The target data were then split into the standard FITS single source format and self-calibration applied. The poor uv -coverage of the observations and the low

Table 1. The sample of radio sources

Source	IAU Name	z	Optical Ident.	Optical Type	S_{178} (Jy)	α	LAS (arcsec)	Size (kpc)	$P_{178}(10^{25} \text{ W Hz}^{-1} \text{ sr}^{-1})$	RM (rad m ⁻²)
3C 16	0035+130	0.405	G	E	12.2	0.94	76.0	545	97	–
3C 19	0038+328	0.482	G	N	13.2	0.63	6.7	53	140	+4
3C 42	0125+287	0.395	G	N	13.1	0.73	29.0	205	92	–47
3C 46	0132+376	0.4373	G	N	11.1	1.13	160.0	1200	113	–87
3C 47	0133+207	0.425	Q	B	28.8	0.98	73.0	539	260	–23
3C 67	0221+276	0.3102	G	B	10.9	0.58	2.5	15	43	–64
3C 109	0410+110	0.3056	G	B	23.5	0.85	96.0	577	96	–16
3C 172	0659+253	0.5191	G	N	16.5	0.86	100.0	824	228	–
3C 200	0824+294	0.458	G	N?	12.3	0.84	24.0	185	126	+15
4C 14.27	0832+143	0.392	G	N	11.2	1.15	37.0	260	89	–
3C 215	0903+169	0.411	Q	B	12.4	1.06	58.0	419	106	+31
3C 225B	0939+139	0.582	G	N	23.2	0.94	5.0	44	436	–25
3C 228	0947+145	0.5524	G	N	23.8	1.00	46.0	391	405	+5
3C 244.1	1030+585	0.428	G	N	22.1	0.82	52.0	385	192	–4
3C 249.1	1100+772	0.311	Q	B	11.7	0.81	44.0	268	49	–29
3C 268.3	1203+645	0.371	G	B?	11.7	0.50	1.7	11	66	+86
3C 274.1	1232+216	0.422	G	N?	18.0	0.87	160.0	1176	154	–4
3C 275.1	1241+166	0.557	Q	B	19.9	0.96	19.0	162	339	–11
3C 295	1409+524	0.4614	G	N	91.0	0.63	5.1	39	873	–
3C 299	1419+419	0.367	G	N	12.9	0.65	12.0	81	75	–
3C 330	1609+660	0.549	G	N	30.3	0.71	61.0	517	447	+13
3C 334	1618+177	0.555	Q	B	11.9	0.86	55.0	469	192	+41
3C 341	1626+278	0.448	G	N	11.8	0.85	76.0	578	115	+18
3C 351	1704+608	0.371	Q	B	14.9	0.73	62.0	422	91	–
3C 427.1	2104+763	0.572	G	E	29.0	0.97	26.0	225	530	+19
3C 455	2252+129	0.5427	Q	B	14.0	0.71	3.9	33	201	+7
3C 457	2309+184	0.428	G	N	14.3	1.01	200.0	1482	133	–

Unless otherwise specified all data are taken from the update of the information presented in LRL (Laing & Riley, private communication). Column 3: Redshift. Column 4: Optical identification of host; Galaxy (G) or Quasar (Q). Column 5: Optical type as broad-line (B), narrow-line (N) or low-excitation (E) following the definitions of Laing et al. (1994). For those with ambiguous optical spectra a best guess is shown and labelled as such with a question mark. Column 6: 178-MHz flux density of the source. Column 7: Low frequency (178-750 MHz) spectral index. Columns 8 and 9: Largest angular size (taken to be the sum of the angular lengths of each lobe) and the corresponding linear size. Column 10: Luminosity at 178 MHz. Column 11: Integrated rotation measure taken from Simard-Normandin, Kronberg & Button (1981), where available.

surface brightness of the structure in most of the sources in the sample observed by MERLIN made self-calibration difficult. The self-calibration solutions from the pipeline did not produce a significant improvement in our image quality; we therefore performed self-calibration and imaging in a fashion similar to that used for the VLA data. Only a single iteration of self-calibration was used. The multi-frequency synthesis capabilities of MERLIN meant that for two sources (3C 19 and 3C 299) observations were made at three frequencies, 4.546, 4.866 and 5.186 GHz. These three-frequency observations were treated separately during the calibration and imaging processes; the data were combined in the image plane using the AIPS task COMB .

3 SOURCES IN DETAIL

In Table 4 we list our measurements of the total and core flux densities for each source and the core positions; this table also includes references to previous radio observations. The optical classification of the associated objects, their redshifts and the overall radio properties of the sources are listed in Table 1. In the discussion of each source we highlight the main features in the maps presented and, where relevant,

we include a summary of the information available at other wavebands (e.g. optical emission line spectra, UV and X-ray observations).

Typically, maps for each of the sources in the sample are presented at two resolutions to show both the large scale structure of the lobes and the detail in the hotspots and jets. The resolution of the lower-resolution map has been chosen to give approximately 50 beam widths across the source; that of the higher-resolution map is the best that could be obtained with the available data. Unless otherwise stated in the figure caption the maps are at 8 GHz. Summaries of the observational properties of each image are given in Table 5. In the contour plots, the lowest positive contour is at approximately five times the r.m.s. off-source noise; negative contours are shown dashed. The lowest level on the greyscale images is three times the r.m.s. off-source noise.

For each source, polarization maps are also presented: Stokes Q and U maps were made using IMAGR and images of polarized intensity (corrected for Ricean bias; Simmons & Stewart 1985) and angle were produced using the AIPS task COMB. The lengths of the vectors represent the fractional polarization, obtained by dividing the polarized intensity by the total intensity at each point; points are only displayed where both the total intensity and the polarized intensity are

Table 2. Observational information for sources in the sample observed with the VLA.

Source	A configuration		B configuration		C configuration		D configuration	
	Date of observation	t_{int} (min)						
3C 16	1999/08/01	90	1997/04/12	60	2000/04/30	60	1998/01/24	15
3C 19	1996/12/14 ^b	15	Not observed	–	Not observed	–	Not observed	–
3C 42	1996/12/14	60	1997/04/12	50	1997/08/29	45	Not observed	–
3C 46 ^a	1998/05/16	180	1998/10/11	120	1997/08/29	135	1998/01/24	45
3C 47	Not observed	–	1985/05/23 ^e	290	1986/11/06 ^e	130	Not observed	–
3C 67	1994/03/03 ^g	120	Not observed	–	Not observed	–	Not observed	–
3C 109	1996/12/14	120	1993/04/02 ^d	30	1991/01/24 ^d	30	1992/07/26 ^d	30
3C 172	1998/05/16	150	1997/04/12	50	2000/05/19	45	1998/01/28	15
3C 200	1996/12/14	60	1997/04/12	50	1997/08/29	45	Not observed	–
4C 14.27	1996/12/14	60	1997/04/12	50	1997/08/29	45	1998/01/28	15
3C 215	1992/10/29 ^c	30	1993/04/02 ^c	30	1991/01/24 ^c	30	1992/07/26 ^c	30
3C 225B	1996/12/14 ^b	15	Not observed	–	Not observed	–	Not observed	–
3C 228	1996/12/14	90	1997/04/12	50	1997/08/29	45	1998/01/28	15
3C 244.1	1996/12/14	90	1997/04/12	50	1989/09/01 ^f	90	1998/01/28	15
3C 249.1	1992/10/29 ^c	30	1993/04/02 ^c	30	1991/01/24 ^c	30	1992/07/26 ^c	30
3C 274.1 ^a	1998/05/16	180	1998/10/13	150	1997/08/29	135	1998/01/28	45
3C 275.1	1996/12/14	60	1997/04/12	50	1997/08/29	45	1998/01/28	15
3C 295	1988/11/25 ^h	600	Not observed	–	Not observed	–	Not observed	–
3C 299	1996/12/14 ^b	15	Not observed	–	Not observed	–	Not observed	–
3C 330	1996/12/14	90	1997/04/12	50	1989/09/19 ^f	170	1989/24/11 ^f	45
3C 334	1986/05/05 ^e	440	1986/07/19 ^e	230	Not observed	–	Not observed	–
3C 341	1996/12/14	90	1997/04/12	50	1997/08/29	45	1998/01/28	15
3C 351	1992/10/29 ^d	30	1993/04/02 ^d	30	1991/01/24 ^d	30	1998/01/24	15
3C 427.1	1996/12/14	60	1997/04/12	50	1997/08/29	45	Not observed	–
3C 455	1996/12/14 ^b	15	Not observed	–	Not observed	–	Not observed	–
3C 457 ^a	1998/05/16	180	1998/10/11	120	1997/08/29	135	1998/01/24	45

^a Observations made with three pointing centres.^b Observed at 4.89 GHz for use with MERLIN data.^c 4.9-GHz *uv*-data kindly supplied by B. J. Wills.^d 8.3-GHz *uv*-data kindly supplied by B. J. Wills.^e 4.9-GHz *uv*-data kindly supplied by J. P. Leahy.^f 8.5-GHz *uv*-data kindly supplied by J. P. Leahy.^g 8.4-GHz image kindly supplied by D. M. Katz-Stone.^h 8.4-GHz image kindly supplied by R. A. Perley.**Table 3.** Observational information for sources in the sample observed with MERLIN.

Source	Date of observation	Freq (GHz)	t_{int} (hr)
3C 19	1997/02/02	4.546, 4.866, 5.186	3×5
3C 67	1996/12/20	4.994	15
3C 225B	1996/12/12	4.994	14
3C 268.3 ^a	1992/05/06	4.995	12
3C 299	1997/02/01	4.546, 4.866, 5.186	3×5

^a 5.0-GHz image kindly supplied by E. Lüdke.

five times the r.m.s. off-source noise level. The vectors shown are drawn parallel to the direction of the received electric vector. The direction of the magnetic field in the source will be perpendicular to this if Faraday rotation is negligible. At 8 GHz significant Faraday rotation, resulting in a correction to the position angles of $\gtrsim 5^\circ$, will only occur when the rotation measure towards a given point is greater than about 70 rad m^{-2} . For most sources the only data available on rotation measures are the integrated rotation measures as listed in Table 1. These indicate that, in the majority of cases, the average correction over the whole source is at most

a few degrees; however this does not necessarily imply that corrections to individual vectors are not greater than this (e.g. Leahy, Pooley & Riley 1986).

We use the following consistent nomenclature when describing the sources. Linear jet-like components in the radio map which meet the criteria of Bridle & Perley (1984) are classified as jets; those that fail one or more of these criteria are classed as possible jets. A hotspot is defined as any bright (greater than ten times the r.m.s. noise), compact (with largest dimension smaller than 10 per cent of the LAS of the source) feature which is not part of a jet. This defini-

tion allows for the possibility of several hotspots in a single lobe. Following Laing (1989) the most compact component is referred to as the primary hotspot, and any other components as secondary hotspots; however, the choice is, in some cases, somewhat subjective. Our definition of a hotspot is similar to that of H97 and L97 but much less restrictive than that of Bridle et al. (1994).

The main features of each source are labelled on the maps presented. Components and regions of interest in the northern lobe are marked N1, N2, N3 etc. with those in the southern lobe labelled S1, S2, S3 etc. Other features, including possible imaging artefacts, are labelled X1, X2, X3 etc.

When a radio core is not clearly visible on an image, the position of the optical identification is marked by a cross. If no radio core has been found in other maps presented here or in the literature, the arm length of the cross indicates the uncertainty in the location of the optical object. Where a radio core is present but its location could be confused by nearby unresolved features (usually knots in a jet) it is labelled with a C.

3.1 3C 16

The radio emission is highly asymmetric and a number of previous observations only show the southern lobe (e.g. Jenkins, Pooley & Riley 1977; Pearson, Readhead & Perley 1985). More recent observations at 1.5 GHz (Leahy & Perley 1991; Bogers et al. 1994) and low-resolution images at 8 GHz (Harvanek & Hardcastle 1998) have detected the northern lobe just above the noise level.

All structure is resolved out in the full-resolution image; the images shown here are at resolutions of 2.5 arcsec (Fig. 1) and 0.75 arcsec (Fig. 2).

The low-resolution image (Fig. 1) confirms the presence of the faint northern lobe which is roughly twice the length of the southern lobe and narrows strikingly halfway along with only a narrow neck of emission connecting the inner and outer parts of the lobe. The optical identification (marked by a cross) falls between two bright regions in the southern half of the source. This structure led Schoenmakers et al. (2000) to suggest that 3C 16 was an example of a ‘double-double’ radio galaxy, possibly formed by an interruption of the activity in the active galactic nucleus. This suggestion is supported by the higher resolution map (Fig. 2) in which there are two weak compact features (N1 and S1) which could be hotspots associated with the inner double. A very faint core coincident with the associated galaxy is also visible on this map.

The tips of both outer lobes are edge brightened although no clearly identifiable hotspots are present in either of them. Both lobes are strongly polarized (~ 50 per cent) with the direction of the magnetic field parallel to the source edge.

3.2 3C 19

No radio core is detected in the VLA A-configuration image (Fig. 3) and the optical identification (marked with a cross) appears to fall within the southern lobe, away from the gap in emission between the two lobes. The lobe structure is significantly asymmetric with respect to the core –

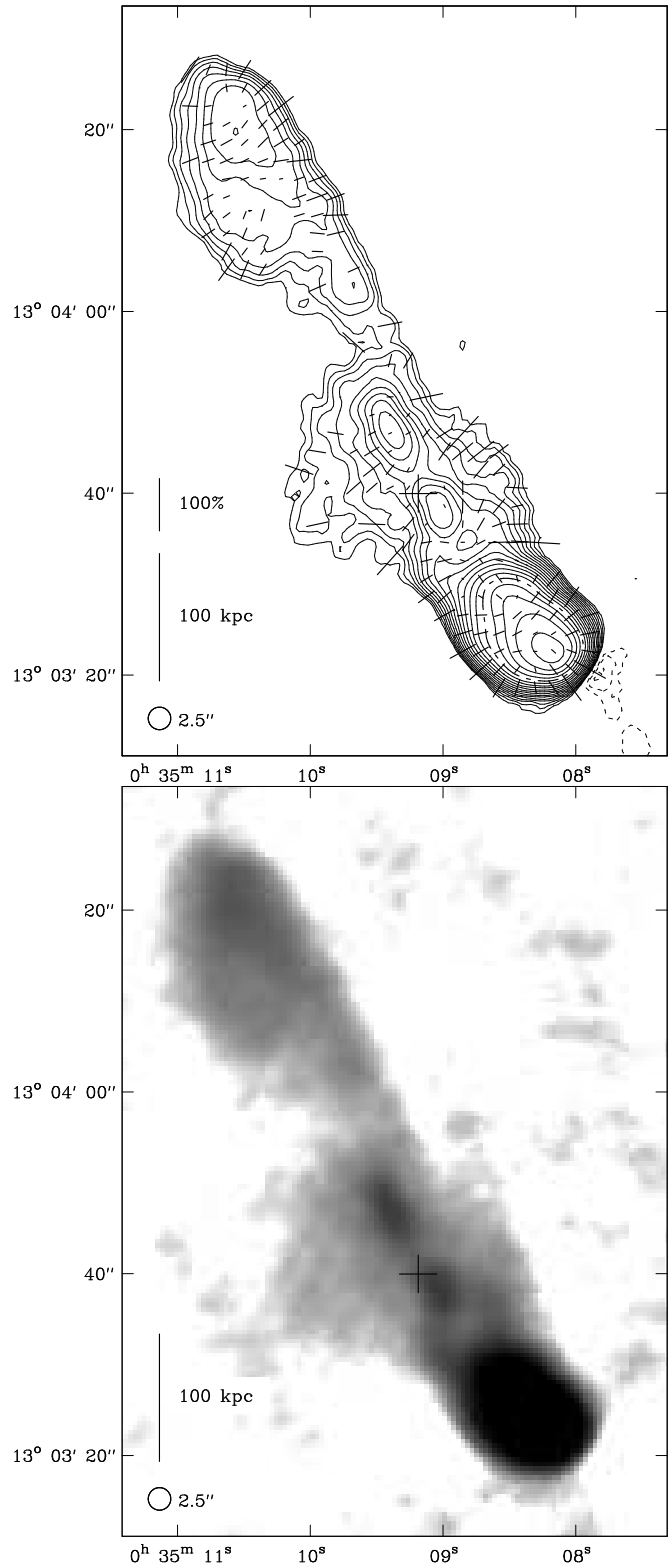


Figure 1. 3C 16 at 2.5-arcsec resolution. Contours at $0.075 \times (-1, 1, \sqrt{2}, 2, \dots)$ mJy beam $^{-1}$. The peak intensity is 31.6 mJy beam $^{-1}$. The cross marks the position of the associated galaxy.

Table 4. Radio data and previous observations for the sample

Source	Freq. (GHz)	Total Flux (mJy)	Core Flux (mJy)	Error (mJy)	Core position		Previous radio map reference
					RA(B1950)	Dec(B1950)	
3C 16	8.46	290	0.26	0.01	00 35 09.126	+13 03 39.90	1, 2, 3, 4, 5
3C 19	4.86	1200	0.47	0.02	00 38 13.742	+32 53 39.18	6, 7
3C 42	8.46	520	3.64	0.02	01 25 42.660	+28 47 30.34	8, 44
3C 46	8.47	200	1.63	0.02	01 32 34.072	+37 38 46.41	9, 10
3C 47	4.89	1200	73.56	0.02	01 33 40.422	+20 42 10.40	10, 11, 12, 13, 14, 15
3C 67	8.44	600	2.00	0.04	02 21 18.054	+27 36 37.64	2, 6, 16, 17, 18, 19, 20
3C 109	8.26	900	240.70	0.03	04 10 54.868	+11 04 40.98	21, 22
3C 172	8.46	510	0.43	0.03	06 59 04.126	+25 18 15.38	23
3C 200	8.46	420	47.96	0.01	08 24 21.377	+29 28 40.59	4, 24
4C 14.27	8.46	160	0.14	0.02	08 32 16.549	+14 22 11.35	3
3C 215	4.89	450	16.37	0.02	09 03 44.126	+16 58 16.00	14
3C 225B	4.86	970	1.11	0.08	09 39 32.235	+13 59 33.58	
3C 228	8.47	670	18.98	0.02	09 47 27.718	+14 34 02.93	12
3C 244.1	8.45	590	1.38	0.02	10 30 19.582	+58 30 04.41	8, 9, 25, 44
3C 249.1	4.89	810	70.70	0.03	11 00 27.444	+77 15 08.41	14, 26, 27, 28
3C 268.3	5.00	1100	1.1		12 03 54.096	+64 30 18.68	16, 18, 19, 29
3C 274.1	8.47	450	2.47	0.01	12 32 56.800	+21 37 05.64	6, 30, 31
3C 275.1	8.46	660	207.40	0.01	12 41 27.557	+16 39 18.03	32, 33, 34
3C 295	8.41	3300	4.64	0.07	14 09 33.375	+52 26 13.59	35, 36, 37
3C 299	4.86	980 ^a	1.64	0.07	14 19 06.206	+41 58 28.82	20, 38, 39
3C 330	8.47	1200	0.58	0.04	16 09 14.084	+66 04 22.57	8, 44
3C 334	4.89	630 ^a	129.51	0.02	16 18 07.288	+17 43 30.32	4, 14, 27, 40, 41
3C 341	8.47	310	0.72	0.03	16 26 02.493	+27 48 14.57	3, 42
3C 351	8.26	740	6.13	0.02	17 04 03.515	+60 48 31.15	3, 14, 43
3C 427.1	8.46	530	0.89	0.02	21 04 45.332	+76 21 08.29	9
3C 455	4.86	840	<1 ^b		22 52 34.526	+12 57 33.50 ^b	4, 18
3C 457	8.46	370 ^a	2.32	0.01	23 09 38.609	+18 29 22.53	3

Column 2 lists the effective frequency of observation for each object. Column 3 gives the total flux at that frequency, measured by integration on suitable maps. Column 4 lists the core flux, taken to be the integrated flux of a Gaussian fitted to the core with the AIPS task JMFIT except where no core was detected, and column 5 gives the error assigned by JMFIT. (The core fluxes of 3C46, 3C67, 3C109 and 3C334 may be variable: see the text.) Columns 6 and 7 give the RA and Dec of the core determined using the AIPS task JMFIT; where no core was detected the position given is that of the associated optical object. References to previous radio maps are given in column 8. References are 1: Jenkins, Pooley & Riley (1977); 2: Pearson, Readhead & Perley (1985); 3: Leahy & Perley (1991); 4: Bogers et al. (1994); 5: Harvanek & Hardcastle (1998); 6: Leahy & Williams (1984); 7: Leahy et al. (1997); 8: Fernini, Burns & Perley (1997); 9: Neff, Roberts & Hutchings (1995); 10: Leahy, Bridle & Strom (2000); 11: Vermeulen et al. (1993); 12: Burns et al. (1984); 13: Fernini et al. (1991); 14: Bridle et al. (1994); 15: Leahy (1996); 16: Lüdke et al. (1998); 17: Sanghera et al. (1995); 18: Akujor & Garrington (1995); 19: Fanti et al. (1985); 20: van Breugel et al. (1992); 21: Antonucci (1985); 22: Giovannini et al. (1994); 23: Jenkins & Scheuer (1976); 24: Garrington, Conway & Leahy (1991); 25: Laing unpublished (see reference 10); 26: Lonsdale & Morison (1983); 27: Dennett-Thorpe (1996); 28: Laing (1988); 29: van Breugel, Miley & Heckman (1984); 30: Strom et al. (1990); 31: Leahy, Pooley & Riley (1986); 32: Akujor et al. (1994); 33: Riley & Pooley (1975); 34: Liu & Pooley (1990); 35: Perley & Taylor (1991); 36: Akujor, Spencer & Wilkinson (1990); 37: Taylor & Perley (1992); 38: Liu & Pooley (1991); 39: Spencer et al. (1991); 40: Leahy, Muxlow & Stephens (1989); 41: Hough et al. (1992); 42: Bridle & Perley (1984); 43: Kronberg, Clarke & van den Bergh (1980); 44: Fernini (2002).

^a Total flux density may be underestimated due to inadequate sampling of the largescale structure.

^b Bogers et al. (1994) have detected a core at 8 GHz at RA 22 52 34.54, Dec +12 57 33.4 with a flux density of 1.4 mJy.

hotspot axis; most of the emission appears on the western side, suggesting strong environmental influences.

MERLIN observations of the two hotspots (Fig. 4) show that they have substantially different structures. The northern hotspot (N2) is edge-brightened with smoothly decreasing brightness along the major axis towards the central component. The southern lobe consists of a very diffuse component (S4) at the centre of a relatively large region bounded by a narrow band over which the brightness changes rapidly. The compact region S3 is located at the edge of the lobe and may represent the primary hotspot with S4 a secondary ‘splatter spot’ (e.g. Williams & Gull 1985). There is a faint trail of emission (S2 to S3) just above the noise level extending from the lobe tip back towards the core.

MERLIN observations of the region near the optical

identification show two main features (Fig. 5). The northern component (C) has lower polarization and is, within the errors, coincident with the optical identification so we identify it as the core. This core appears to be elongated towards the northern hotspot, indicating a possible jet (N1). The second feature near the core (S1) could be a jet knot, but it is extended perpendicular to the axis joining the core and the southern hotspot making this unlikely.

Laing (1988) and Garrington et al. (1988) found that in many extended high-luminosity sources the radio lobe on the jet side shows less depolarization than that on the counterjet side. This effect favours the simple relativistic beaming model in which the lobe on the jet side is moving towards us and is therefore seen through less of the surrounding medium than the counterjet side. In 3C 19, however, the data may be

Table 5. Properties of the images of LRL FR II radio sources with $0.3 < z < 0.6$.

Source	Fig.	Region	FWHM		σ (μJy)	Source	Fig.	Region	FWHM		σ (μJy)
			(arcsec)	(kpc)					(arcsec)	(kpc)	
3C 16	1	Whole	2.500	17.9	15	3C 244.1	35	Whole	0.750	5.6	20
	2	S Lobe	0.750	5.4	10		36	Hotspots	0.400	3.0	13
3C 19	2	Whole	0.750	5.4	10	3C 249.1	36	Whole	0.400	3.0	13
	3	Whole	0.400	3.2	53		37	Whole	1.200	7.3	53
	4	Hotspots	0.055	0.4	114		38	Jet	0.350	2.1	23
3C 42	5	Core	0.055	0.4	114	39	W Hotspot	0.350	2.1	23	
	6	Whole	0.400	2.8	13	3C 268.3	40	Whole	0.061	0.4	63
	7	Hotspots	0.250	1.8	11	3C 274.1	41	Whole	1.000	7.4	12
3C 46	7	Whole	0.250	1.8	11	42	N Hotspot	1.000	7.4	12	
	8	Whole	2.500 ^a	18.8	14	42	N Hotspot	0.250	1.9	14	
	9	N Hotspot	0.900	6.8	12	43	S Hotspot	1.000	7.4	12	
	9	N Hotspot	0.290 ^b	2.2	7	3C 275.1	44	Whole	0.225	1.9	8
3C 47	10	S Hotspot	0.900	6.8	12	45	Whole	0.225	1.9	8	
	11	Whole	1.300	9.6	22	3C 295	46	Whole	0.175	1.3	100
3C 67	12	Lobes	1.300	9.6	22	47	Whole	0.250	1.9	50	
	13	Whole	0.200	1.2	38	47	Lobes	0.250	1.9	50	
3C 109	14	N Hotspot	0.050	0.3	240	3C 299	48	Whole	0.410	2.8	66
	15	S Hotspot	0.050	0.3	240	49	N Hotspot	0.050	0.3	119	
	16	Whole	2.500	15.0	60	49	S Hotspot	0.050	0.3	119	
3C 172	17	Whole	1.100	6.6	35	3C 330	50	Whole	2.500	21.2	80
	18	N Hotspot	1.100	6.6	35	51	Hotspots	0.300	2.5	22	
	18	N Hotspot	0.275	1.7	20	51	Whole	0.300	2.5	22	
	19	S Hotspot	1.100	6.6	35	3C 334	52	Whole	1.150	9.8	34
	19	S Hotspot	0.275	1.7	20	53	N Lobe	0.350	3.0	14	
3C 200	20	Whole	2.500	20.6	40	54	S Lobe	0.350	3.0	14	
	21	N Lobe	0.900	7.4	15	3C 341	55	Whole	1.500	11.4	24
	21	N Hotspot	0.225	1.9	18	56	Hotspots	0.225	1.7	17	
	22	S Lobe	0.900	7.4	15	56	Jet	0.225	1.7	17	
3C 215	22	S Hotspot	0.225	1.9	18	56	Whole	0.225	1.7	17	
	23	Whole	0.375	2.9	24	3C 351	57	Whole	3.000	20.4	40
	24	Jet/N lobe	0.250	1.9	10	58	Hotspots	0.300	2.0	12	
4C 14.27	24	Whole	0.250	1.9	10	58	Jet	0.300	2.0	12	
	25	Whole	1.000	7.0	18	58	Whole	0.300	2.0	12	
3C 225B	26	Whole	0.250	1.8	11	3C 427.1	59	Whole	0.450	3.9	19
	26	Hotspots	0.250	1.8	11	60	Whole	0.250	2.2	14	
	27	Whole	0.900	6.5	19	61	N Hotspot	0.450	3.9	19	
3C 228	28	Jet	0.370	2.7	17	61	N Hotspot	0.250	2.2	14	
	29	Whole	0.400	3.5	134	62	S Hotspot	0.450	3.9	19	
3C 228	30	N Hotspot	0.050	0.4	257	62	S Hotspot	0.250	2.2	14	
	31	S Hotspot	0.050	0.4	257	3C 455	63	Whole	0.400	3.4	70
	32	Whole	1.200	10.2	38	3C 457	64	Whole	1.000	7.4	12
	33	Hotspots	0.225	1.9	12	65	N Hotspot	1.000	7.4	12	
3C 244.1	33	Whole	0.225	1.9	12	66	S Hotspot	1.000	7.4	12	
	34	Jet	0.225	1.9	12	66	S Hotspot	0.250	1.9	12	

Columns 4 and 5: Angular and corresponding linear size of the FWHM of the restoring beam used; unless otherwise stated the restoring beam is circular. Column 6: R.m.s. off-source noise in $\mu\text{Jy beam}^{-1}$; in several cases there are artefacts around bright hotspots at several times this level.

^a The beam is 2.5×2.0 arcsec² in p.a. -77° .

^b The beam is 0.29×0.25 arcsec² in p.a. -55° .

inconsistent with this trend. The northern lobe is significantly more strongly polarized than the southern lobe but, on the other hand, the possible detection of a long kiloparsec-scale jet (S2 to S3) in the southern lobe and a shorter jet (N1) in the northern lobe may imply that the southern lobe is the approaching one.

3.3 3C 42

Our images of 3C 42 (Figs 6 and 7) show a smooth uniform-brightness bridge in the northern lobe and double structure (N1, N2) at the tip of the northern lobe. There is a smooth decrease in brightness throughout the southern lobe away from a single hotspot towards the core. The average percentage polarization of the northern lobe (~ 30 per cent) is slightly greater than that of the southern (~ 20 per cent) although both show some variation along their extent. The northern hotspot region narrows very significantly as it runs

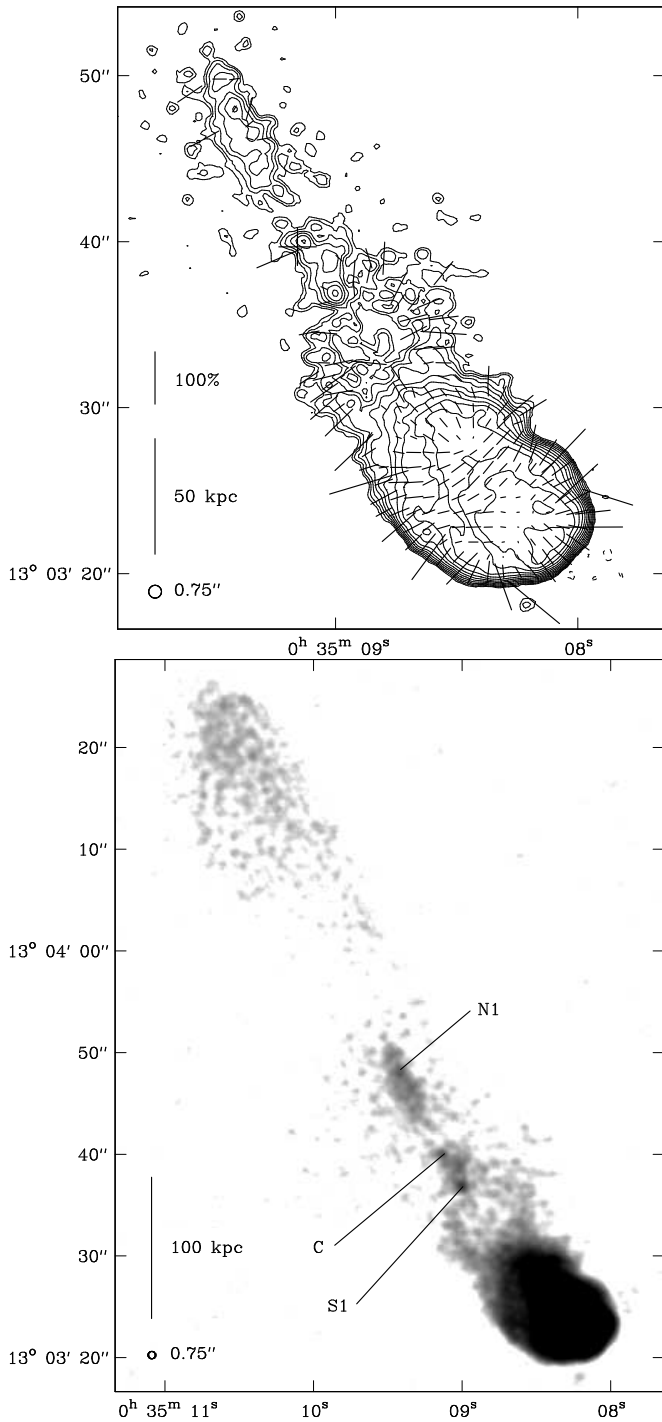


Figure 2. 3C 16 at 0.75-arcsec resolution. Above: The southern end, contours at $0.050 \times (-1, 1, \sqrt{2}, 2, \dots)$ mJy beam $^{-1}$. The peak intensity is 3.85 mJy beam $^{-1}$. Below: The whole source.

into the northern lobe; the higher-resolution image (Fig. 7) shows that this ‘neck’ of emission is very strongly polarized (~ 70 per cent). In the northern hotspot region, there is a ridge of emission (N3) from one of the peaks (N2) pointing towards the core. The high curvature in this ridge prevents it from being classified as a jet and it is possibly more likely to represent backflow. Because N1 is marginally brighter and more compact than N2, we classify N1 as the primary hot-

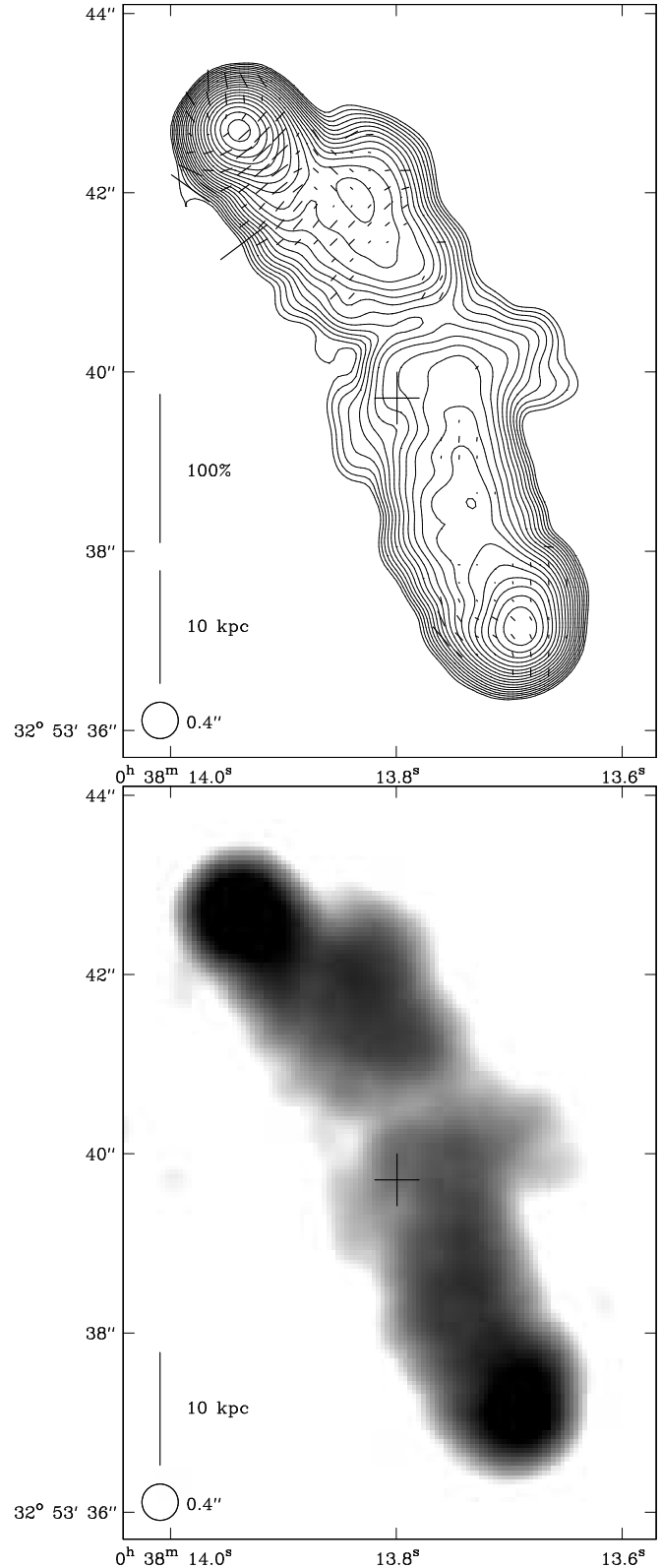


Figure 3. 3C 19 at 5 GHz and 0.4-arcsec resolution. Contours at $0.25 \times (-1, 1, 1.5, 2, 2.25, \dots)$ mJy beam $^{-1}$. The peak intensity is 306 mJy beam $^{-1}$.

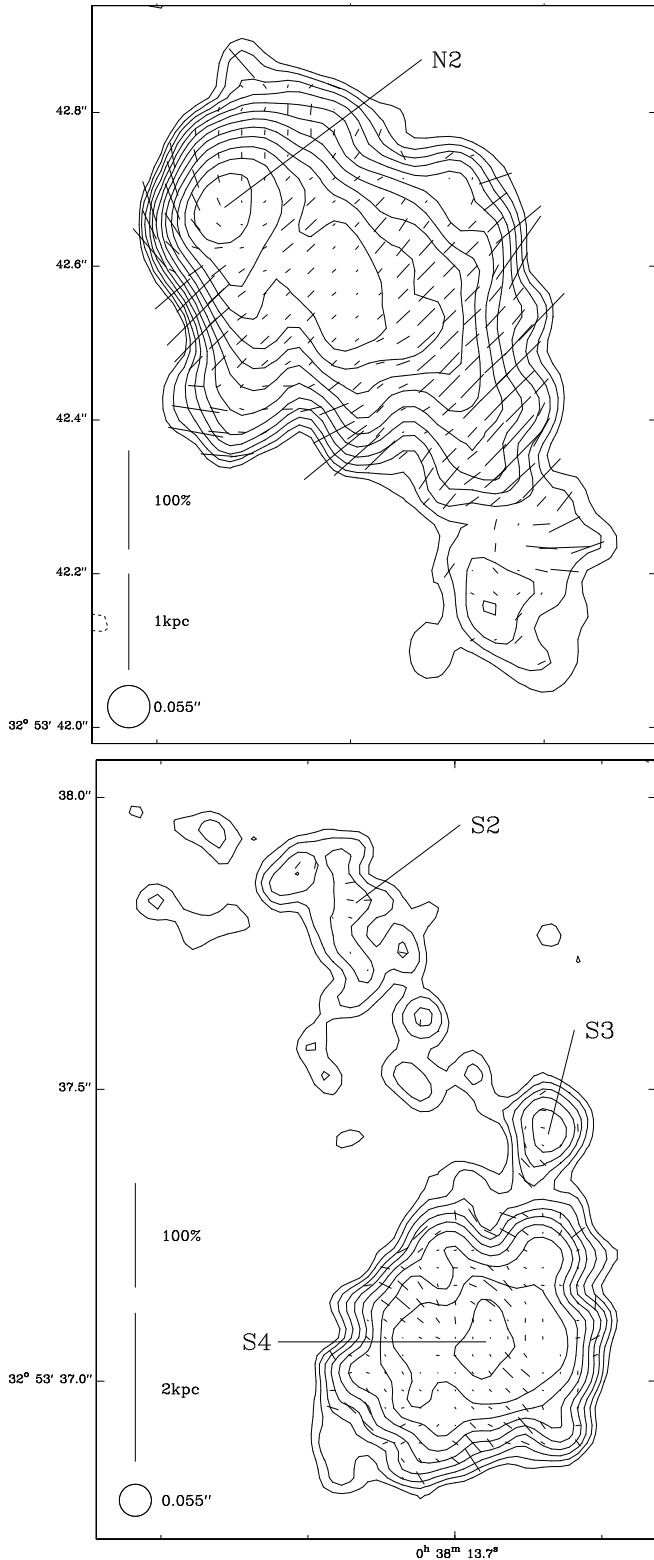


Figure 4. Hotspots of 3C 19 at 5 GHz and 0.055-arcsec resolution. Above: Northern hotspot, contours at $0.5 \times (-1, 1, \sqrt{2}, 2, \dots)$ mJy beam $^{-1}$. The peak intensity is 31.2 mJy beam $^{-1}$. Below: Southern hotspot, contours at $0.354 \times (-1, 1, \sqrt{2}, 2, \dots)$ mJy beam $^{-1}$. The peak intensity is 6.79 mJy beam $^{-1}$.

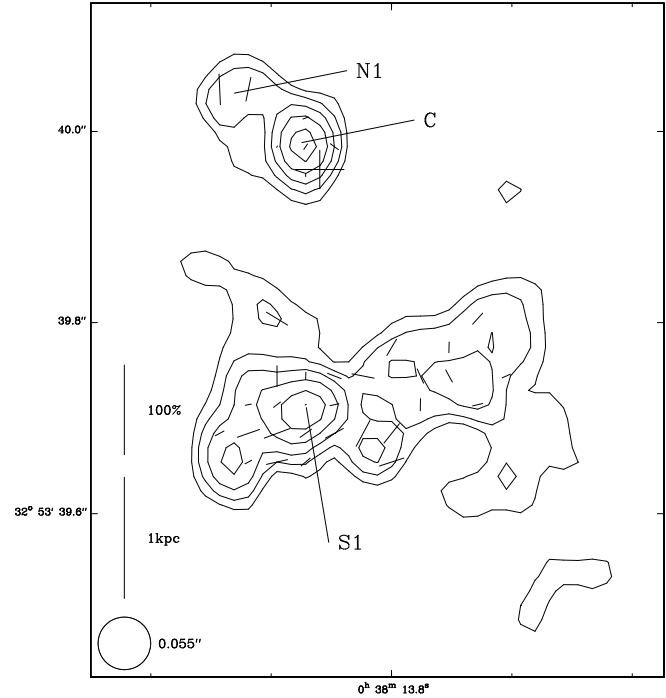


Figure 5. Core region of 3C 19 at 5 GHz and 0.055-arcsec resolution. Contours at $0.177 \times (-1, 1, \sqrt{2}, 2, \dots)$ mJy beam $^{-1}$. The peak intensity is 0.90 mJy beam $^{-1}$.

spot. Fernini, Burns & Perley (1997), on the other hand, classify N2 as the primary from their 5-GHz image with a resolution of 0.4 arcsec. These features are also discussed by Fernini (2002) who used our A- and B-array data to produce images of 3C 42 at similar resolutions. (We have included C-array data in making our images and the noise levels on our maps are about a factor of two lower than his.) He comments that the southern hotspot does not fulfill the criteria for a hotspot defined by Bridle et al. (1994).

3.4 3C 46

3C 46 is one of the largest sources in the sample. It has a large integrated rotation measure of -87 rad m $^{-2}$ so that polarization vectors at 8 GHz may be misaligned with the true magnetic field direction by rotations of order 5° .

The image at 2.5-arcsec resolution shows lobe structure extending much of the way back towards the core (Fig. 8); the 1.5-GHz low resolution image in Leahy, Bridle & Strom (2000) shows a complete bridge. There is a low-brightness feature, N3, extending to the northeast ahead of the northern hotspot region whereas the southern hotspot is at the edge of the lobe. As well as having the outward extension to the northeast, the tip of the northern lobe is much narrower than the tip of the southern lobe (Figs 9 and 10). However, at 0.9-arcsec resolution, both the northern and southern hotspots show double structure (N1, N2 and S1, S2); the outer components, N2 and S2, are, respectively, brighter and more compact than N1 and S1 and are identified as the primary hotspots. The component N2 is still quite compact in the

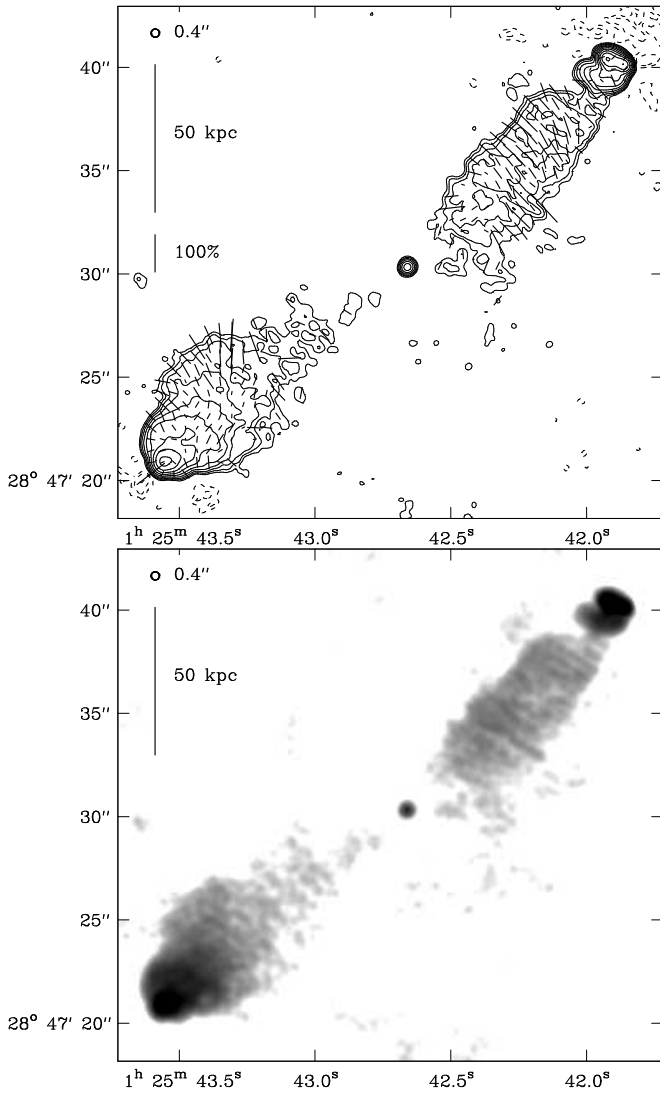


Figure 6. 3C 42 at 0.4-arcsec resolution. Contours at $0.065 \times (-2, -1, 1, 2, 4, \dots)$ mJy beam^{-1} . The peak intensity is $35.2 \text{ mJy beam}^{-1}$.

highest resolution (0.29 arcsec) image but N2, S1 and S2 are essentially resolved out at this resolution.

A 1.4 mJy core is detected. From observations with the VLA in A configuration alone, Neff, Roberts & Hutchings (1995) quote flux densities for the core of 11 mJy and 3.6 mJy at 1.5 and 5 GHz, indicating that the core is steep spectrum; taken at face value these imply an unusually steep spectrum between 5 and 8 GHz with a spectral index of 1.8. However, Neff et al. comment that their images show complex non-aligned structures, which are probably imaging artefacts, near the core so that there are significant errors in the flux densities they quote for the core; it is also possible that the core is variable though we see no evidence for this in our data which were collected over a period of fourteen months.

3.5 3C 47

3C 47 is associated with a quasar at a redshift of 0.425.

The 4.9-GHz image presented here was made using the

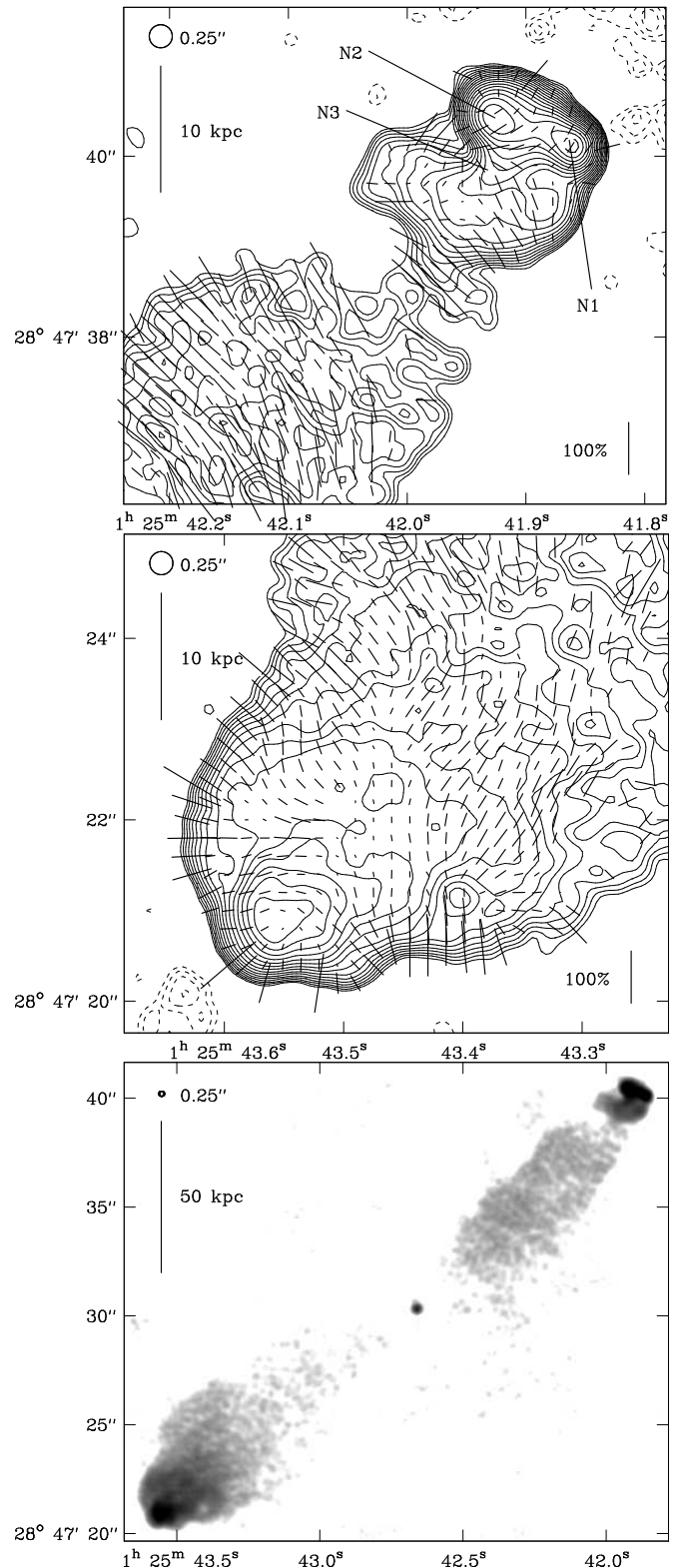


Figure 7. 3C 42 at 0.25-arcsec resolution. Contours at $0.055 \times (-2, -\sqrt{2}, -1, 1, \sqrt{2}, 2, \dots)$ mJy beam^{-1} . Top: Northern hotspot. The peak intensity is $23.8 \text{ mJy beam}^{-1}$. Middle: Southern hotspot. The peak intensity is $9.57 \text{ mJy beam}^{-1}$. Bottom: The whole source.

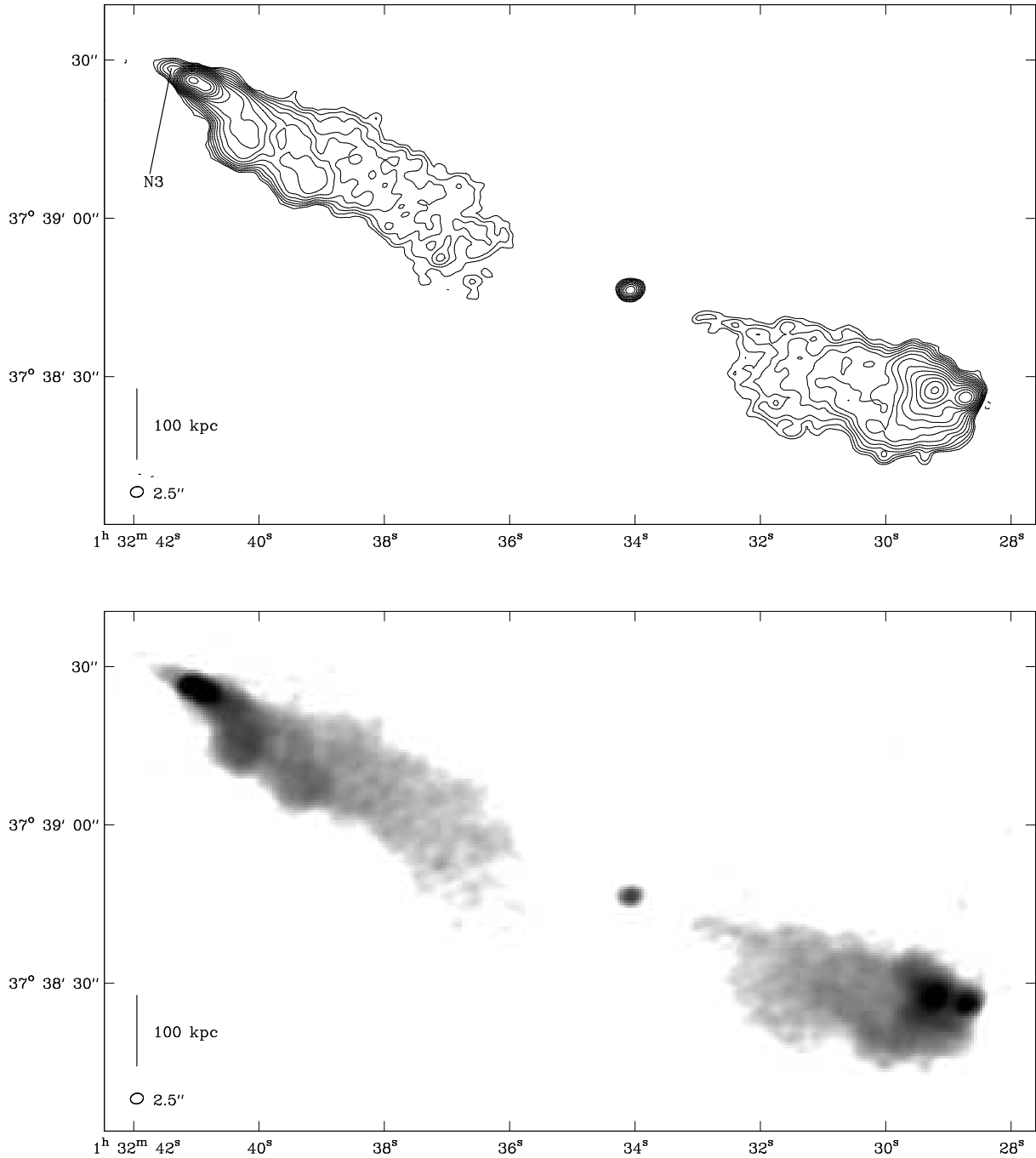


Figure 8. 3C 46 at 2.5-arcsec resolution. Contours at $0.070 \times (-1, 1, \sqrt{2}, 2, \dots)$ mJy beam $^{-1}$. The peak intensity is 14.9 mJy beam $^{-1}$.

B- and C-array uv -data acquired by Fernini et al. (1991) for their study of the depolarization asymmetry in 3C 47. It was included in our analysis for the sake of completeness. Since there are no A-array observations the full-resolution restoring beam has a FWHM of 1.3 arcsec, rather larger than that for the rest of the sample.

Vermeulen et al. (1993) have detected super-luminal motion ($\sim 7.4c$, assuming $H_0 = 50 \text{ km s}^{-1} \text{ Mpc}^{-1}$) close to the core constraining the angle of orientation to within $\sim 20^\circ$ of the line of sight. This is in contrast with the lobe structure (Fig. 11) which is more reminiscent of a radio galaxy at an angle greater than 45° . The outer edges of both lobes are

very sharp, but within the lobes the brightness appears to fall smoothly away from the hotspots, dropping below the noise level well before reaching the central object. This suggests that a bridge would be observed in higher sensitivity images.

The strong jet (S1 to S2) can be followed almost continuously to the hotspot at S3 (Fig. 12). There is also evidence for an outflow (S4) from the hotspot and a secondary, but very diffuse, ‘warm’ spot at S5.

Fernini et al. (1991) found that the northern lobe was very much more strongly depolarized than the jetted south-

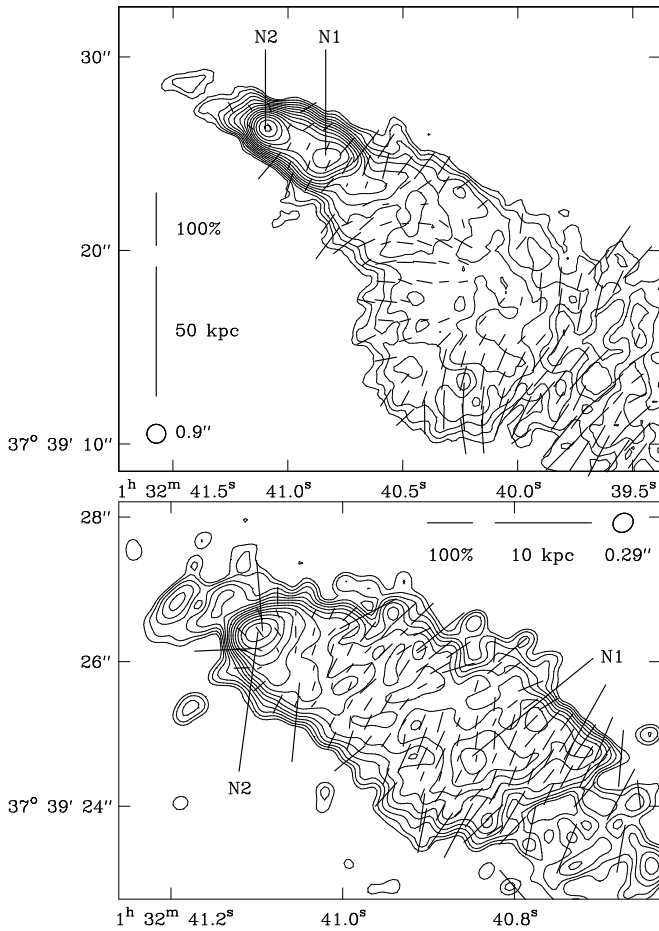


Figure 9. Northern tip of 3C 46. Above: At 0.9-arcsec resolution, contours at $0.060 \times (-1, 1, \sqrt{2}, 2, \dots)$ mJy beam $^{-1}$. The peak intensity is 8.1 mJy beam $^{-1}$. Below: At 0.29-arcsec resolution, contours at $0.035 \times (-1, 1, \sqrt{2}, 2, \dots)$ mJy beam $^{-1}$. The peak intensity is 2.9 mJy beam $^{-1}$.

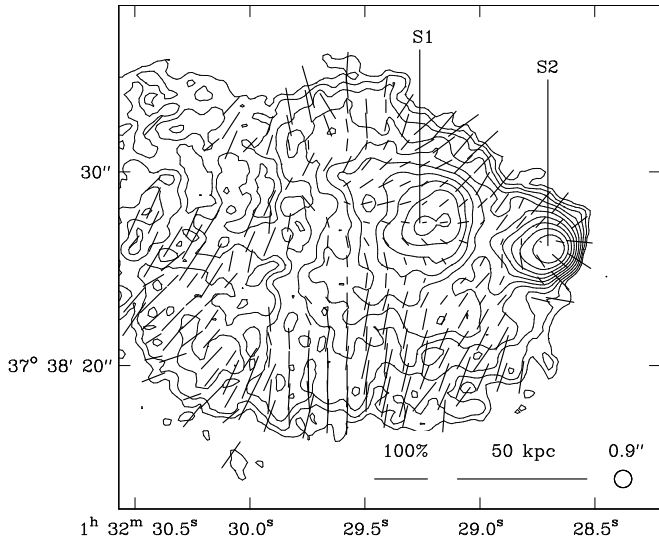


Figure 10. Southern tip of 3C 46 at 0.9-arcsec resolution. Contours at $0.060 \times (-1, 1, \sqrt{2}, 2, \dots)$ mJy beam $^{-1}$. The peak intensity is 1.9 mJy beam $^{-1}$.

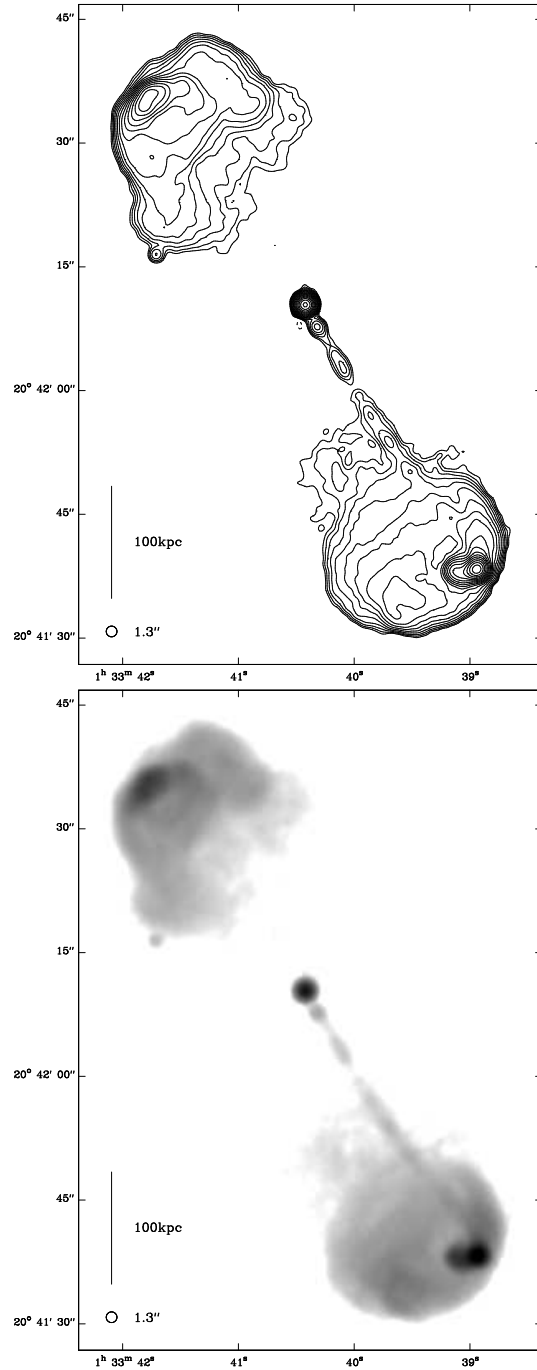


Figure 11. 3C 47 at 5 GHz and 1.3-arcsec resolution. Contours at $0.15 \times (-1, 1, 1.5, 2, 2.25, \dots)$ mJy beam $^{-1}$. The peak intensity is 198 mJy beam $^{-1}$.

ern lobe, in accordance with the Laing–Garrington effect (Laing 1988, Garrington et al. 1988) described in Section 3.2.

The feature X1 (Fig. 12) is unpolarized and has a flat spectrum; it is therefore almost certainly an unrelated background source (Leahy, Bridle & Strom 2000).

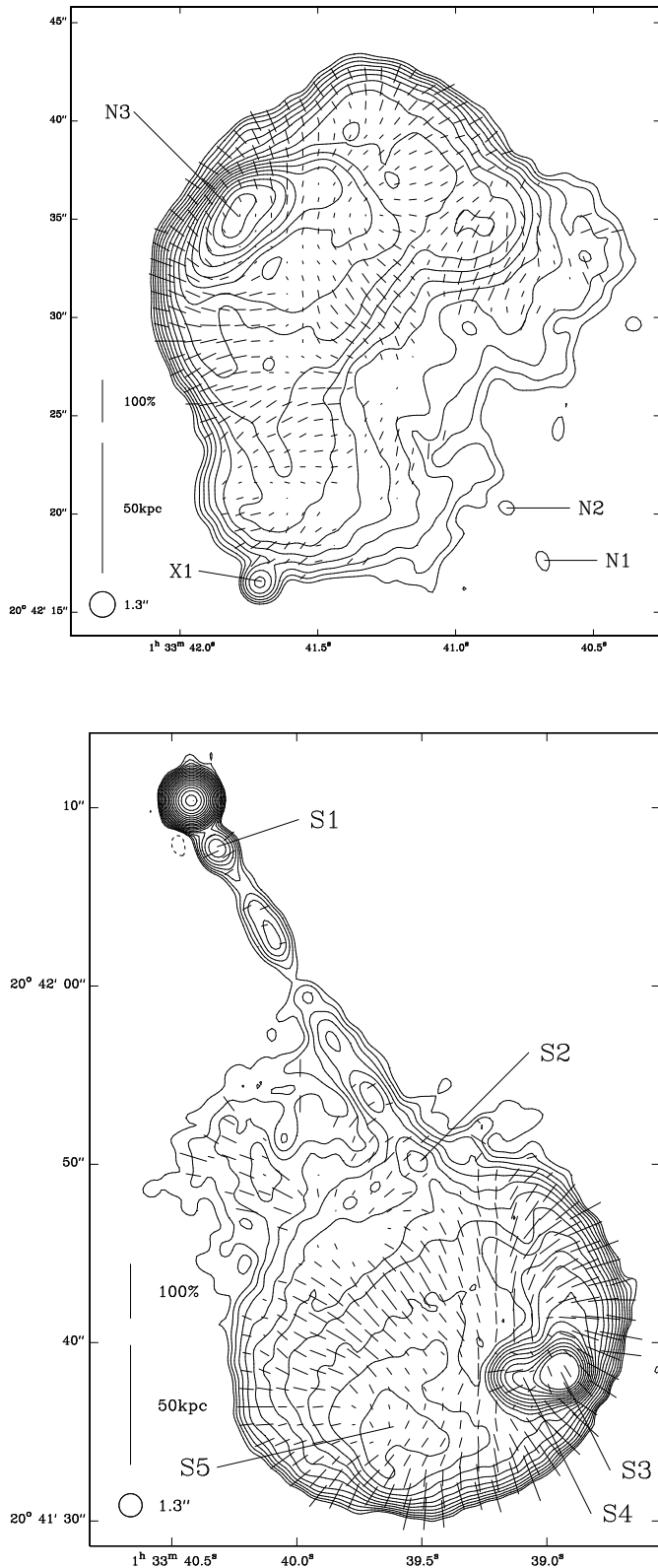


Figure 12. Lobes of 3C 47 at 5 GHz and 1.3-arcsec resolution. Above: Northern lobe, contours at $0.125 \times (-1, 1, \sqrt{2}, 2, \dots)$ mJy beam $^{-1}$. The peak intensity is 25.9 mJy beam $^{-1}$. Below: Southern lobe, contours at $0.125 \times (-1, 1, \sqrt{2}, 2, \dots)$ mJy beam $^{-1}$. The peak intensity is 198 mJy beam $^{-1}$.

3.6 3C 67

The radio structure of 3C67 is very asymmetric in both total intensity and polarization and has been extensively studied by many authors (see Table 4). Due to an error on our part A-configuration 5-GHz observations of 3C 67 were not made; the 8-GHz image presented here (Fig. 13) is that of Katz-Stone (private communication) for which no matching polarization data were available.

There is a large uncertainty in the position of the optical identification (LRL) which has led some authors (e.g. Fanti et al. 1985) to identify the core location with the southern lobe. However Fig. 13 clearly shows a 2-mJy core whose position is marginally beyond the 1σ error limits given by LRL. At the same location a 3-mJy core is revealed by the 5 GHz MERLIN observations of Sanghera et al. (1995). However, no such feature is present above the noise level in the MERLIN data presented here at a similar sensitivity and frequency (Fig. 14); this allows us to place an upper limit on its flux density ~ 1 mJy, suggesting that it is variable.

The lobes are distorted around the central component at N6 and S3 in a manner reminiscent of the lobe structure in larger sources bent around a central galaxy (Leahy & Williams 1984). In this source, however, the distortion is occurring within 5 kpc of the core so that the bending is presumably happening well inside the host galaxy.

The northern lobe is more extended and more strongly polarized than the southern one (Fig. 14). The hotspot (N4) appears to be significantly recessed from the end of the northern lobe which ends in a diffuse, but edge-brightened, structure (N5).

The southwest edge of the northern lobe has a region polarized at the 20 per cent level extended over a length of ~ 1 kpc (N3). van Breugel et al. (1992) and Lüdke et al. (1998) find a similar pattern at other frequencies, indicating little depolarization or Faraday rotation between 5 and 15 GHz.

There is possible evidence for a jet in the northern lobe provided by two features just above the noise level – a slightly elongated structure (N1) and a possible knot (N2) on the edge of the polarized region.

The southern lobe is compact and weakly polarized (Fig. 15). The feature (S2) to the south west of the hotspot (S1) also appears in the image presented by Lüdke et al. (1998). On a scale of 30 mas, an EVN map (Fanti et al. 1985) shows this lobe to be broken into two distinct components with the hotspot slightly recessed from the edge of the lobe.

3.7 3C 109

3C 109 is associated with a broad-line radio galaxy with a strong, variable core (Antonucci 1985; Giovannini et al. 1994).

The low-resolution image in Fig. 16 shows a weak jet (S1) extending from the core to the southeast lobe. The inner half of the southern lobe is of uniform brightness whereas the outer half of the southern lobe and the whole of the northern lobe show a smooth decrease in brightness from the hotspots back towards the centre. Both lobes show similar degrees of polarization (~ 20 per cent), although there is a notable lack of polarized emission from the middle of the northern lobe.

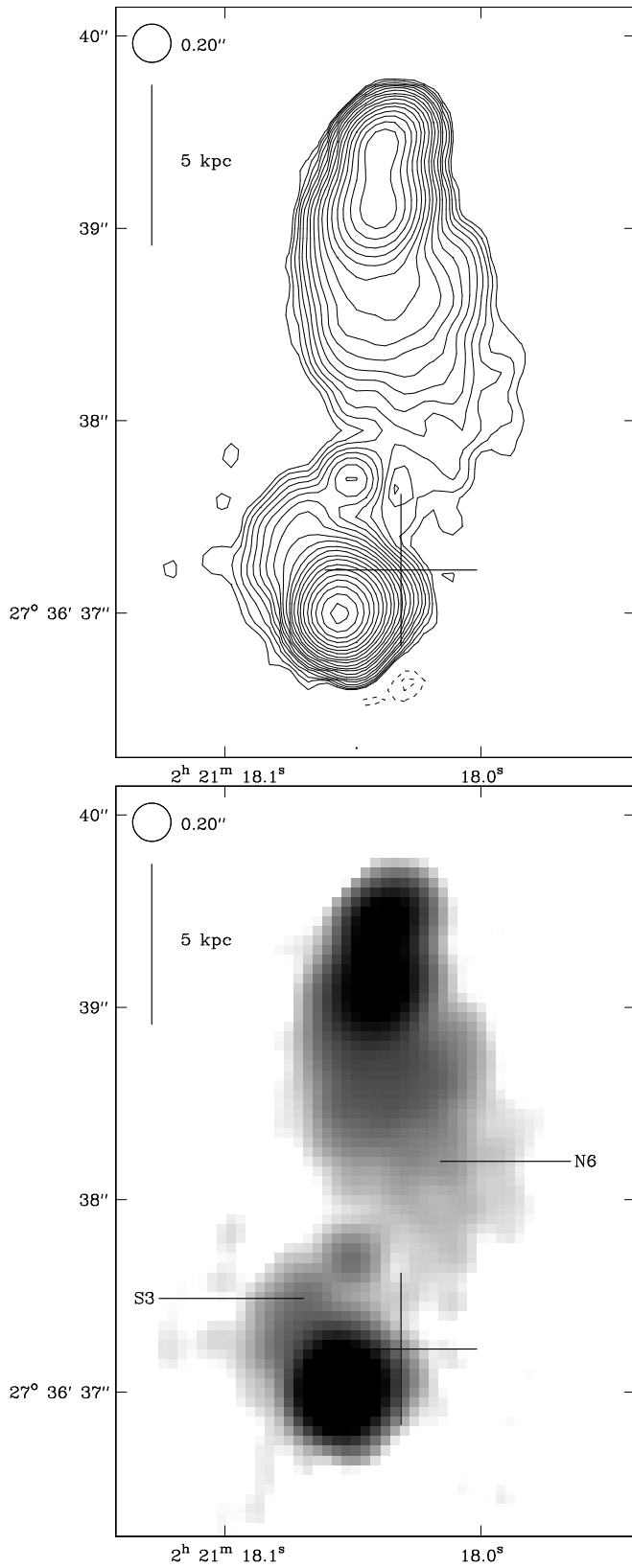


Figure 13. 3C 67 at 8 GHz and 0.2-arcsec resolution. Contours at $0.20 \times (-\sqrt{2}, -1, 1, \sqrt{2}, 2, \dots)$ mJy beam $^{-1}$. The peak intensity is 235 mJy beam $^{-1}$. (Image provided by D. Katz-Stone.)

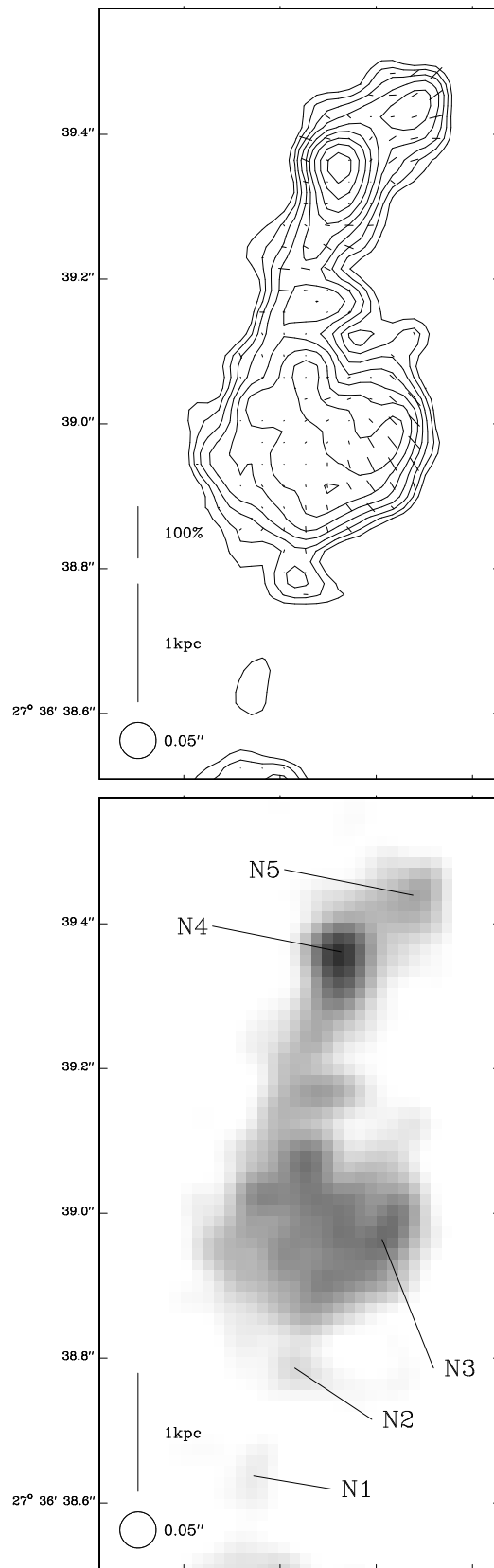


Figure 14. Northern hotspot of 3C 67 at 5 GHz and 0.05-arcsec resolution. Contours at $1 \times (-1, 1, \sqrt{2}, 2, \dots)$ mJy beam $^{-1}$. The peak intensity is 19.6 mJy beam $^{-1}$.

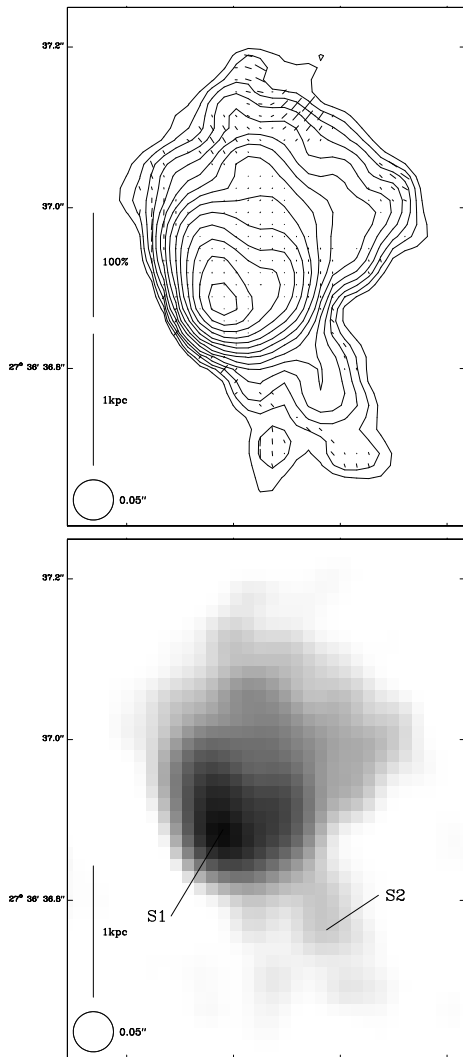


Figure 15. Southern hotspot of 3C 67 at 5 GHz and 0.05-arcsec resolution. Contours at $1 \times (-1, 1, \sqrt{2}, 2, \dots)$ mJy beam $^{-1}$. The peak intensity is 108 mJy beam $^{-1}$.

An image of the whole source at a higher resolution of 1.1 arcsec and of the hotspot regions at resolutions of 1.1 and 0.275 arcsec are shown in Figs 17, 18 and 19. The image of the northern hotspot region at 1.1 arcsec (Fig. 18) shows a hotspot (N1) at the tip of a larger region of relatively uniform emission. In the 0.275-arcsec image of this region N1 is resolved, with a compact region set back slightly from the end of the lobe. The 1.1-arcsec image of the southern lobe (Fig. 19) shows that there is an extended region of enhanced brightness (S2 to S3) leading to the hotspot S4 (see also Fig 17); the polarization angle lies parallel to this path which is tentatively identified as that of the jet. The hotspot S4 is slightly resolved in the 0.275-arcsec image. The region S5 is diffuse and off the main axis of the jet (although it is on the main axis of the source) and is therefore classified as a secondary hotspot.

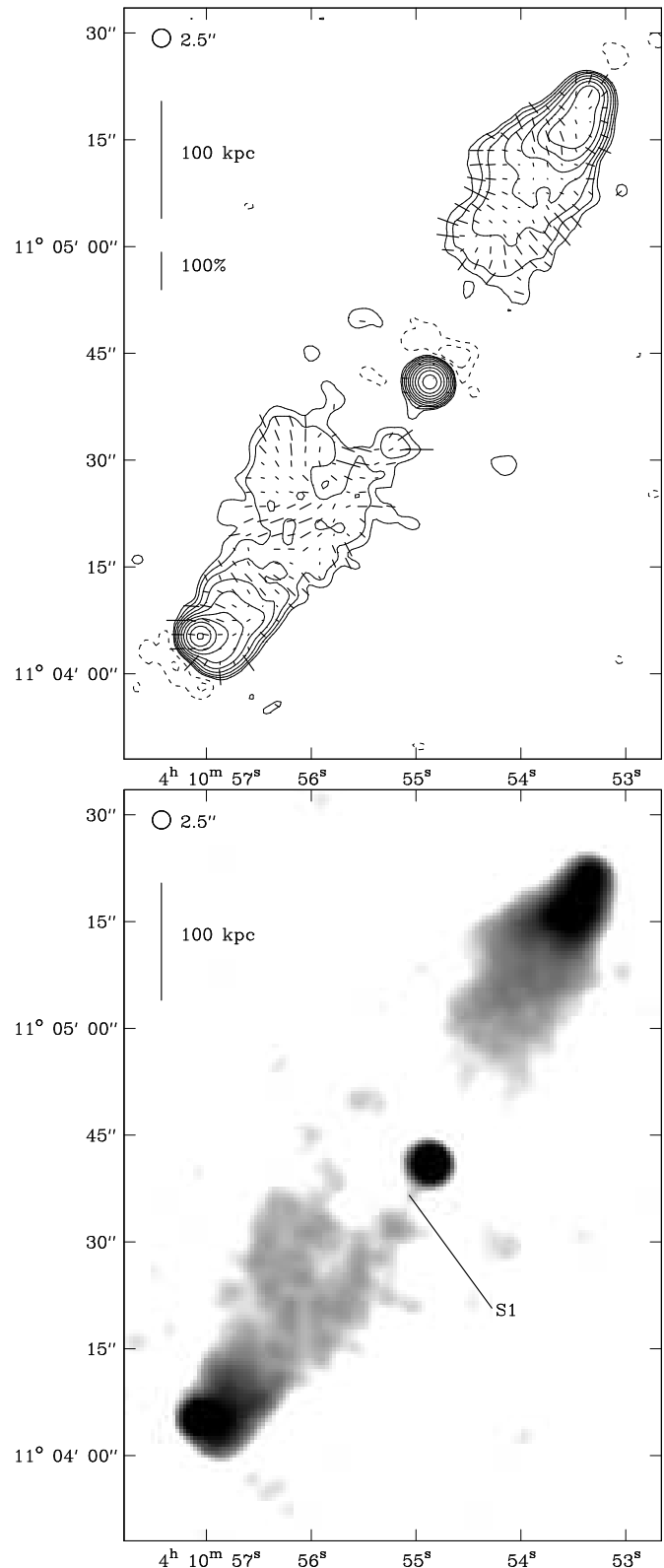


Figure 16. 3C 109 at 2.5-arcsec resolution. Contours at $0.3 \times (-2, -1, 1, 2, 4, \dots)$ mJy beam $^{-1}$. The peak intensity is 241 mJy beam $^{-1}$.

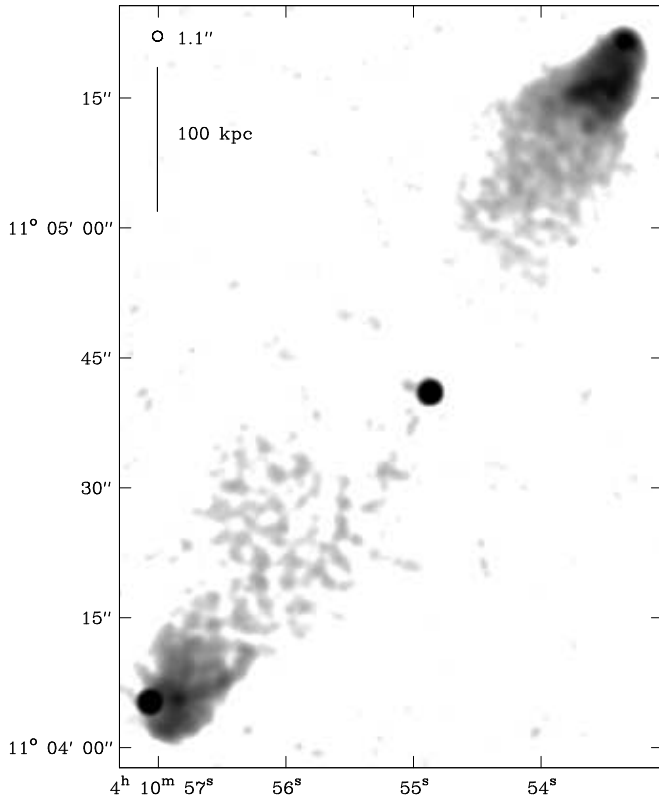


Figure 17. 3C 109 at 1.1-arcsec resolution.

3.8 3C 172

3C 172 exhibits a number of unusual properties, yet no high-quality radio images appear in the literature.

The low-resolution image (Fig. 20) shows that the southern edge of the northern lobe is slightly edge brightened. Both lobes are highly polarized (North ~ 50 per cent; South ~ 40 per cent) with the magnetic field direction parallel to the lobe edges except on the edges nearest to the core; here the magnetic field direction is parallel to the source axis, possibly indicating that the lobes continue below the noise level back towards the core. However, the relatively sharp change in brightness at the inner edge of both lobes may suggest that a low brightness bridge does not exist and that the lobes are detached from the core (e.g. Jenkins & Scheuer 1976). There is a weak core coincident with the associated galaxy.

The higher-resolution image of the northern lobe (Fig. 21) shows that the eastern edge is remarkably straight and fades smoothly into the noise whereas the western edge is edge brightened with a pronounced curve. The hotspot narrows considerably as it runs into the lobe; it is clearly resolved in the 0.225-arcsec image with no obvious compact features.

The 0.9-arcsec image of the southern lobe (Fig. 22) shows a double hotspot. However in the 0.225-arcsec image there is substantial structure in this hotspot region. The eastern component of the double consists of two knots of emission (S1, S2) leading to a bright hotspot (S3) which is slightly elongated perpendicular to the source axis and which we identify as the primary hotspot. The western com-

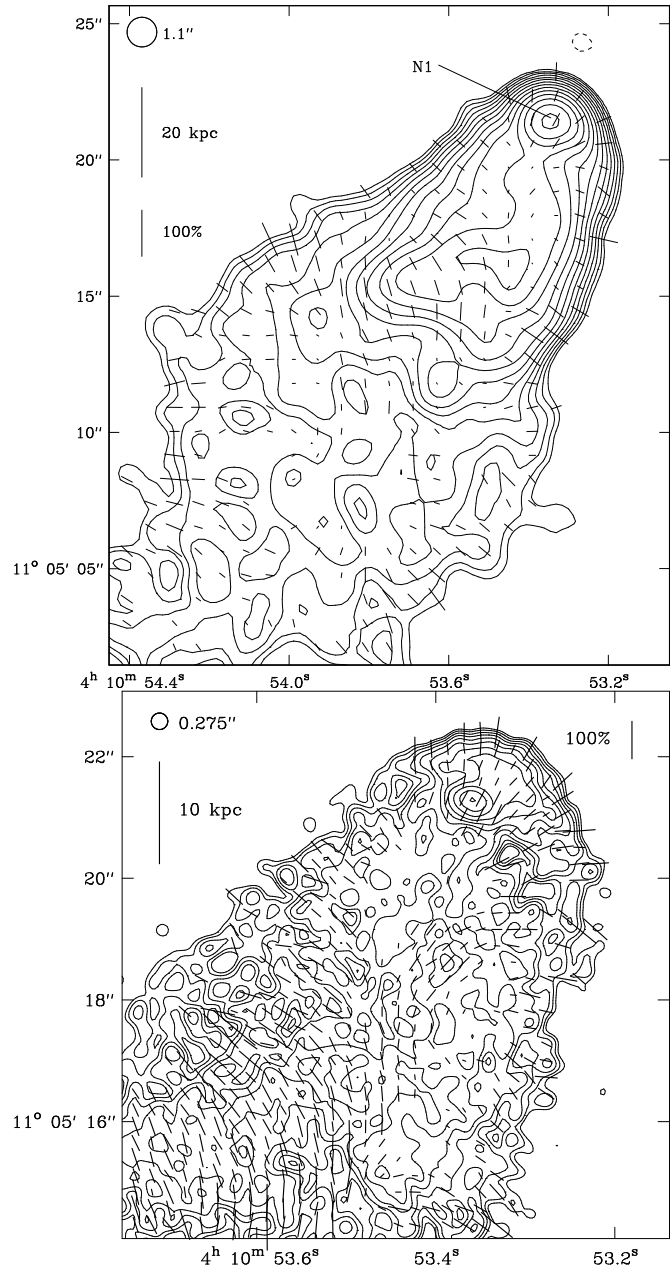


Figure 18. Northern hotspot of 3C 109. Above: 1.1-arcsec resolution. Contours at $0.175 \times (-1, 1, \sqrt{2}, 2, \dots)$ mJy beam $^{-1}$. The peak intensity is 17.3 mJy beam $^{-1}$. Below: 0.275-arcsec resolution. Contours at $0.1 \times (-1, 1, \sqrt{2}, 2, \dots)$ mJy beam $^{-1}$. The peak intensity is 3.25 mJy beam $^{-1}$.

ponent of the double is edge brightened but shows no obvious compact features.

3.9 3C 200

The most striking feature of 3C 200 is a pronounced one-sided jet. However, the associated optical object is a narrow-line radio galaxy implying that the axis is probably at a large angle to the line of sight; such a jet is therefore unex-

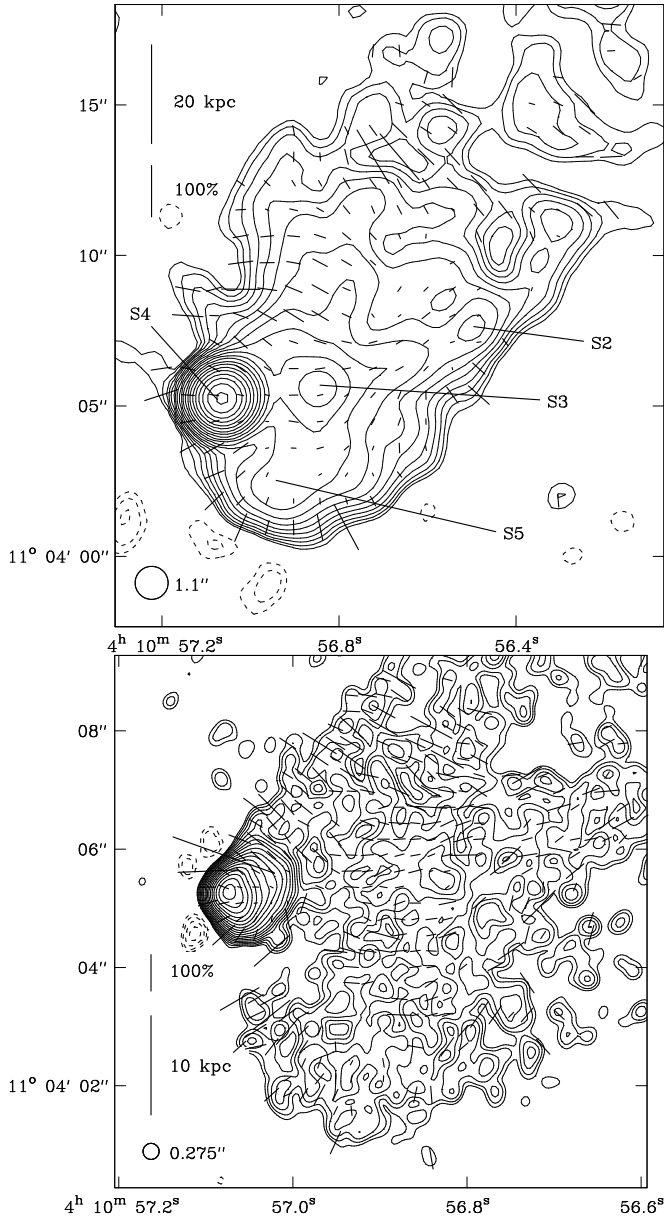


Figure 19. Southern hotspot of 3C 109. Above: 1.1-arcsec resolution. contours at $0.175 \times (-2, -\sqrt{2}, -1, \sqrt{2}, 2, \dots)$ mJy beam $^{-1}$. The peak intensity is 136 mJy beam $^{-1}$. Below: 0.275-arcsec resolution. Contours at $0.1 \times (-2, -\sqrt{2}, -1, 1, \sqrt{2}, 2, \dots)$ mJy beam $^{-1}$. The peak intensity is 42.8 mJy beam $^{-1}$.

pected. Interestingly, the distorted lobe morphology is also more characteristic of the quasars in the sample.

Low-frequency images (Garrington, Conway & Leahy 1991; Bogers et al. 1994) show extensive lobes only hinted at in the maps presented here (Fig. 23). The northern lobe extends to the east, and there is a large area of smooth emission surrounding the jet between the tip of the southern lobe and the core.

The southern lobe (Figs 23 and 24) contains a strong jet which bends sharply three-quarters of the way along its length and terminates in a diffuse structure (S1). There is a significant dip in the emission at X3 around which an

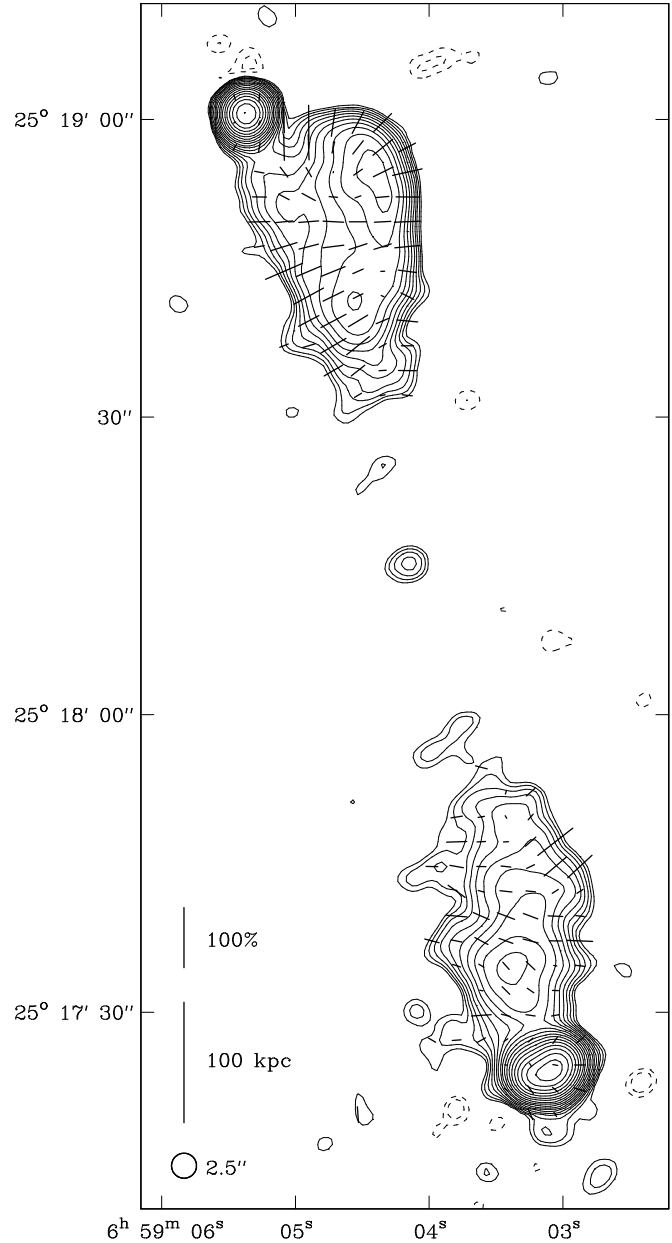


Figure 20. 3C 172 at 2.5-arcsec resolution. Contours at $0.2 \times (-\sqrt{2}, -1, 1, \sqrt{2}, 2, \dots)$ mJy beam $^{-1}$. The peak intensity is 88.8 mJy beam $^{-1}$.

arc links S1 to a second slightly lower peak (S2). The jet is polarized (~ 30 per cent) with the magnetic field parallel to its length until the point where it starts to bend. After this point the polarization drops to ~ 10 per cent and the magnetic field direction becomes perpendicular to the jet. There is an additional weak feature (X2) at the point where the southern jet bends; it is strongly polarized (~ 60 per cent) perpendicular to the jet direction. Its relationship to the rest of the lobe is unclear.

There is a possible faint counterjet (N1) in the northern lobe (Figs 23 and 24) pointing towards a pronounced hotspot (N2/N3). The remainder of the lobe is of relatively uniform brightness, although there is an arc-like structure around a dip in the emission X1 rather similar to that in the southern

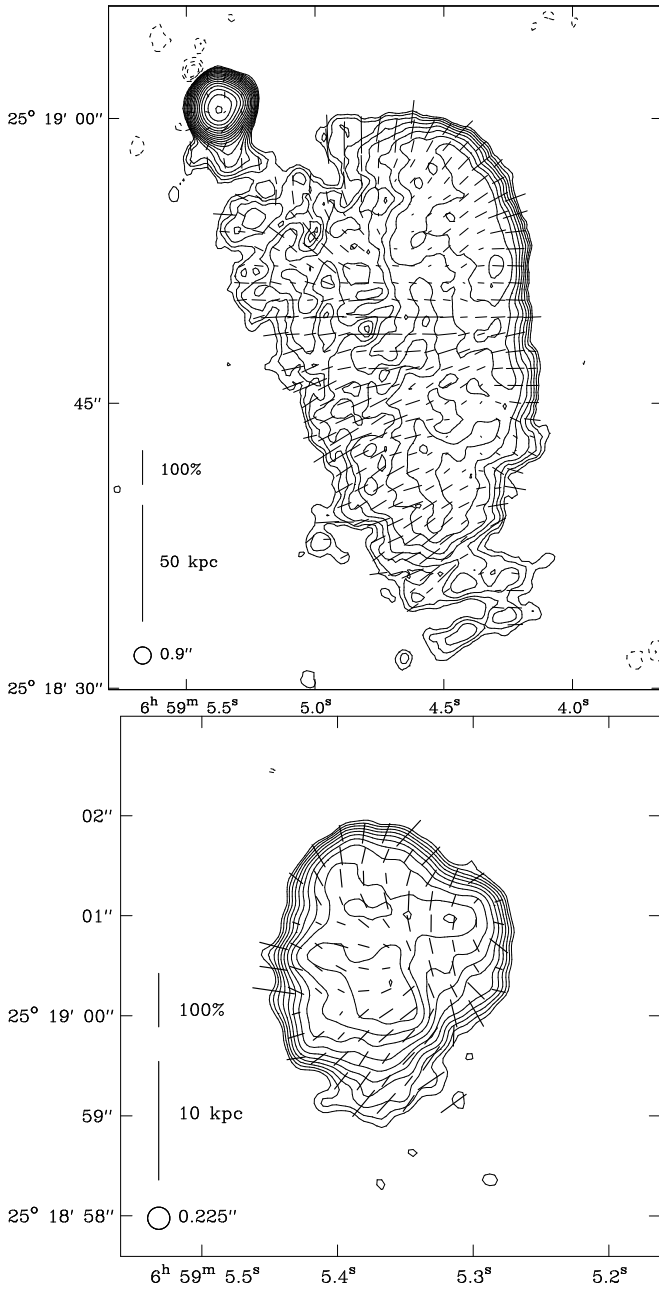


Figure 21. Northern lobe and hotspot of 3C172. Above: Northern lobe at 0.9-arcsec resolution. Contours at $0.075 \times (-\sqrt{2}, -1, 1, \sqrt{2}, 2, \dots)$ mJy beam $^{-1}$. The peak intensity is 28.1 mJy beam $^{-1}$. Below: Northern hotspot at 0.225-arcsec resolution. Contours at $0.09 \times (-1, 1, \sqrt{2}, 2, \dots)$ mJy beam $^{-1}$. The peak intensity is 2.90 mJy beam $^{-1}$.

lobe, which links N2/3 to an edge brightened region at the northern tip (N4). The higher resolution image (Fig. 24) shows two components, N2 and N3, in the hotspot; N3 is slightly more compact so we label it as the primary.

In the 8-GHz images presented here both lobes are strongly polarized (~ 50 per cent) with the magnetic field parallel to the lobe boundary at the edges. At lower frequencies (e.g. 1.5 GHz; Garrington, Conway & Leahy 1991) the northern (unjetted) lobe is more strongly polarized than the

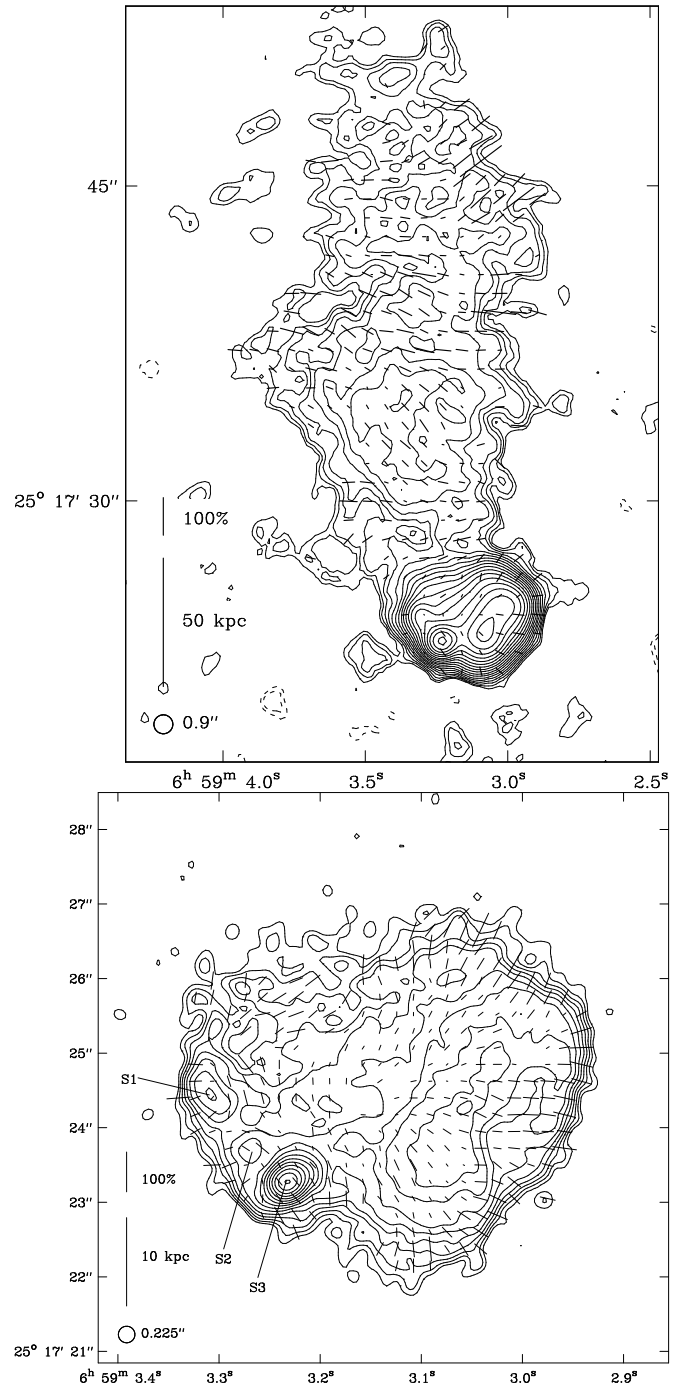


Figure 22. Southern lobe and hotspot of 3C 172. Above: Southern lobe at 0.9-arcsec resolution. Contours at $0.075 \times (-\sqrt{2}, -1, 1, \sqrt{2}, 2, \dots)$ mJy beam $^{-1}$. The peak intensity is 29.9 mJy beam $^{-1}$. Below: Southern hotspot at 0.225-arcsec resolution. Contours at $0.09 \times (-1, 1, \sqrt{2}, 2, \dots)$ mJy beam $^{-1}$. The peak intensity is 11.9 mJy beam $^{-1}$.

southern (jetted) one. This is inconsistent with what would be expected from the Laing–Garrington correlation.

3.10 4C 14.27

At a resolution of 1 arcsec the northern lobe of 4C 14.27 is very narrow (Fig. 25) and strongly polarized (~ 40 per cent);

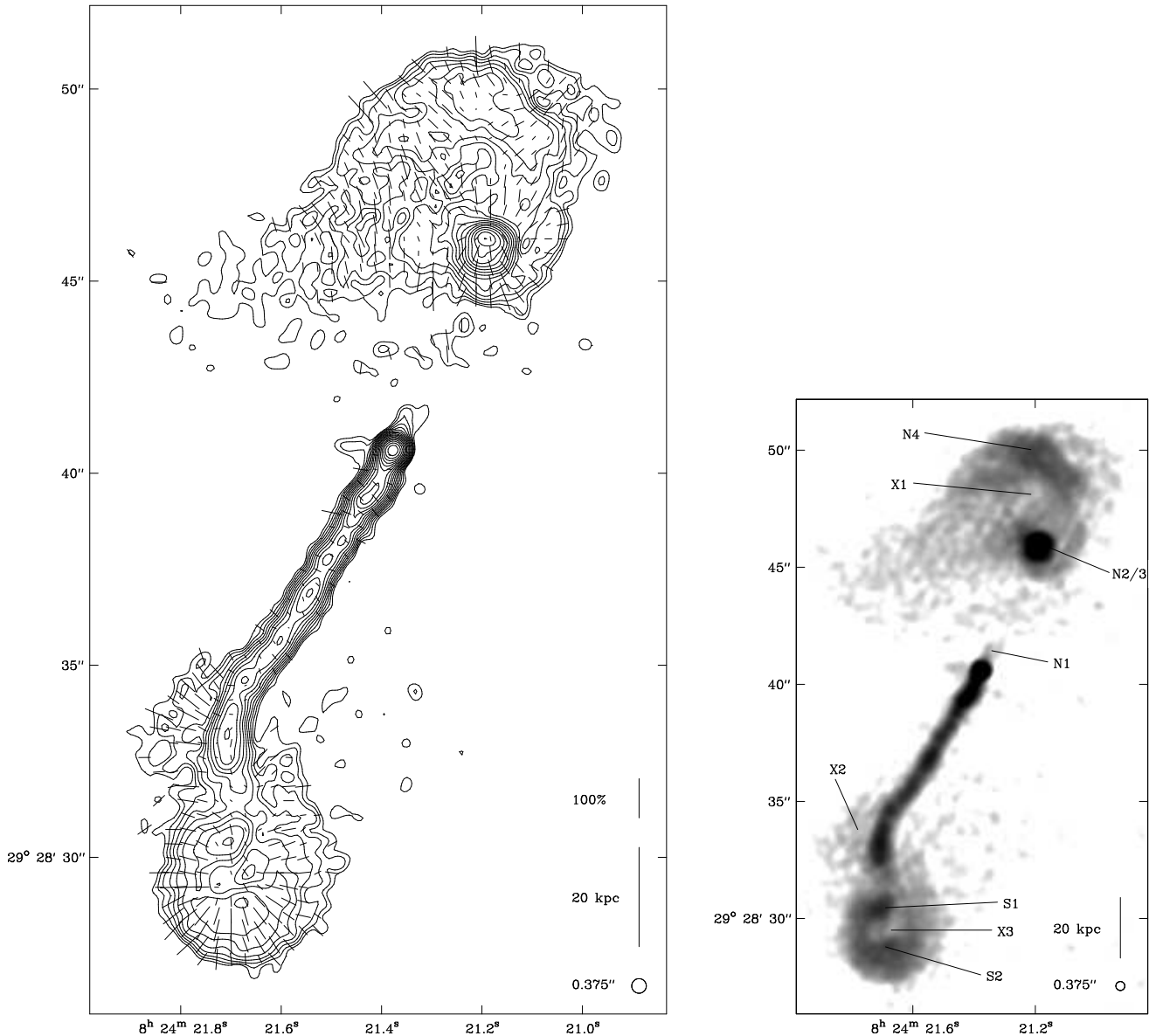


Figure 23. 3C 200 at 0.375-arcsec resolution. Contours at $0.120 \times (-1, 1, \sqrt{2}, 2, \dots)$ mJy beam $^{-1}$. The peak intensity is 41.7 mJy beam $^{-1}$.

except in the hotspot region, N1, the direction of the magnetic field is parallel to the source axis along the entire lobe. The southern lobe is significantly shorter and wider than the northern lobe and has a curving ridgeline; the 1.5-GHz image of Leahy & Perley (1991) shows that it has an even more extensive wing (stretching to the north) than shown here. Except in its northern wing the southern lobe is less polarized (~ 20 per cent) than the northern lobe.

In the 0.25-arcsec image (Fig. 26) the lobe emission is well resolved. Both the northern and southern hotspot regions are diffuse; the arc-like regions N1 and S1 are identified as possible hotspots.

A radio core, C, is detected just above the noise level at a position coincident with the location of the optical identification.

3.11 3C 215

3C 215 is associated with a quasar. The lobes and the jet are very distorted (Fig. 27) and Bridle et al. (1994) describe the structure as “evidently ambiguous”, lacking many of the characteristics of powerful sources. The unusual plume structure in the southern lobe is more reminiscent of FR I activity than an FR II lobe.

The southern jet is extremely twisted and knotty. There is a steady decrease in brightness in the lobe to the south of this jet, through S7, S8 and S9, and although the material appears to be at least partially confined at the lobe edges (in particular there is significant edge brightening at S9), it would be hard to claim convincingly that there is a hotspot in this region. The higher-resolution image (Fig. 28) shows the jet region in more detail. Bridle et al. (1994) suggest that S4 is possibly the hotspot candidate, but, like component S1 in the jet, this region is curved and may be a jet knot where

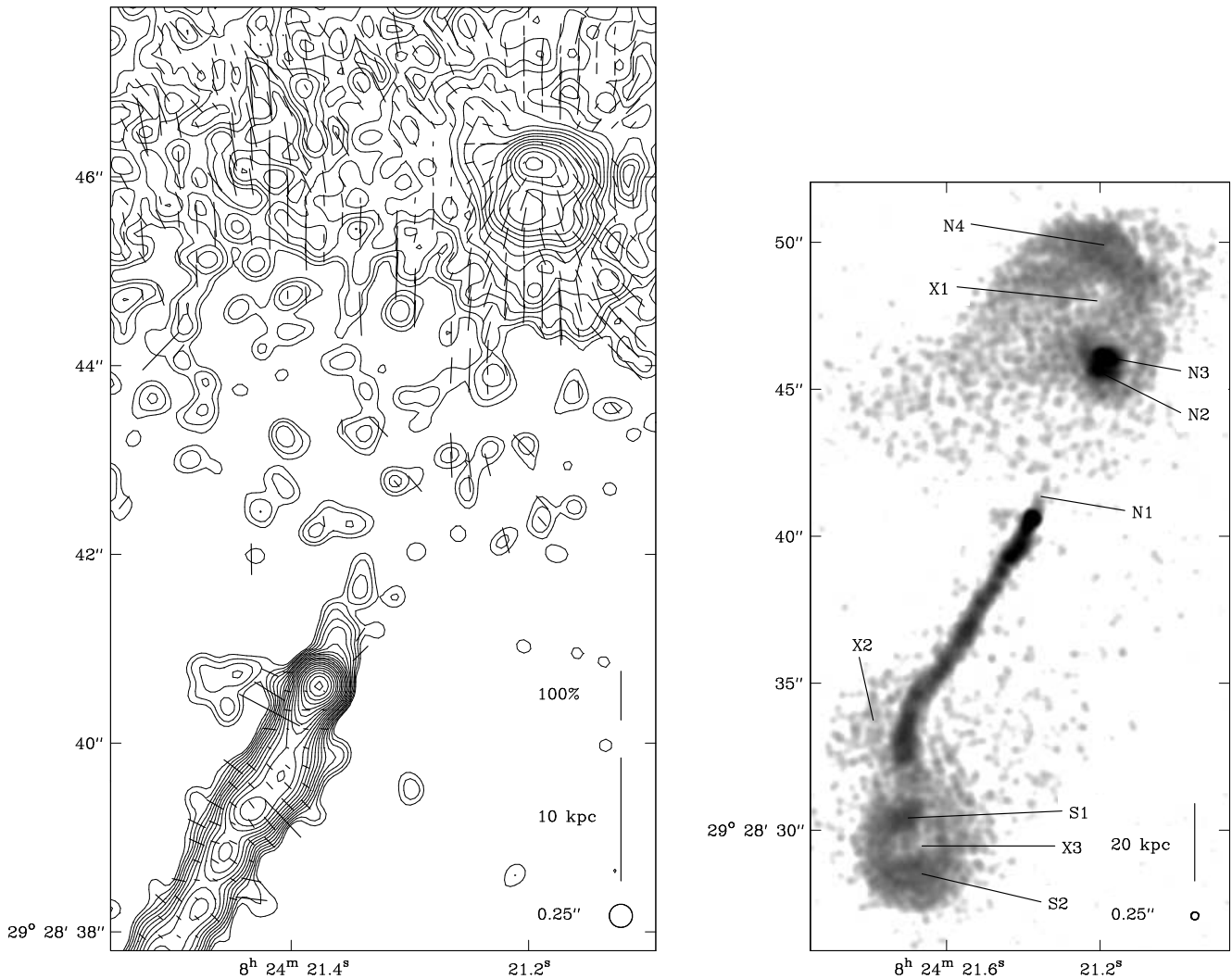


Figure 24. 3C 200 at 0.25-arcsec resolution. Contours at $0.050 \times (-1, 1, \sqrt{2}, 2, \dots)$ mJy beam $^{-1}$. Left: The northern hotspot, core and part of the jet. The peak intensity is 39.7 mJy beam $^{-1}$. Right: Whole source.

the beam is deflected towards S5. The strongly polarized (~ 50 per cent) region S6 may represent the flow of material from S5 towards S7. Its alignment with the central part of the jet (S1 to S4) is probably significant and may indicate the interaction of jet material that has not been bent near S4 with either the external medium or backflow from S5.

The northern lobe is more similar to that of a typical FR II source. A very faint ridge of emission (N1 to N2) marks the position of a possible counter-jet, the longest in the sample (see Bridle et al. 1994). Although the northern lobe is edge brightened (N2) there is no evidence for a compact hotspot; the brightest point is diffuse and significantly recessed from the edge of the lobe.

Strong X-ray emission (Hardcastle & Worrall 1999, Hardcastle, private communication) and galaxy counts (Ellingson, Yee & Green 1991) indicate that the source is in a rich cluster environment, perhaps explaining the distorted structure.

Except in the region S7, the distribution of polarized intensity is complex and there is no simple relation between the angle of the magnetic field and features in the total emis-

sion. In S7 the polarization vectors are highly ordered and the magnetic field direction is parallel to the lobe axis. Since the source lies in a rich cluster it is possible that the complex polarization structure is a result of strong differential Faraday rotation in the cluster medium; on the other hand the integrated rotation measure of 31 rad m^{-2} is not unusually large (see Table 1) and does not necessarily provide support for this suggestion.

3.12 3C 225B

The VLA 5-GHz map (Fig. 29) shows a radio core coincident with the position of the optical nucleus. There is a marked asymmetry in polarization with the southern lobe being considerably more polarized (~ 20 per cent) than the northern one ($\lesssim 5$ per cent). This may be due to asymmetric depolarization, giving an indication of orientation and implying that the southern lobe is closer to us than the northern one.

MERLIN images of the source show similarities between the hotspot regions of the northern (Fig. 30) and southern lobes (Fig. 31). Both regions contain a fairly compact peak

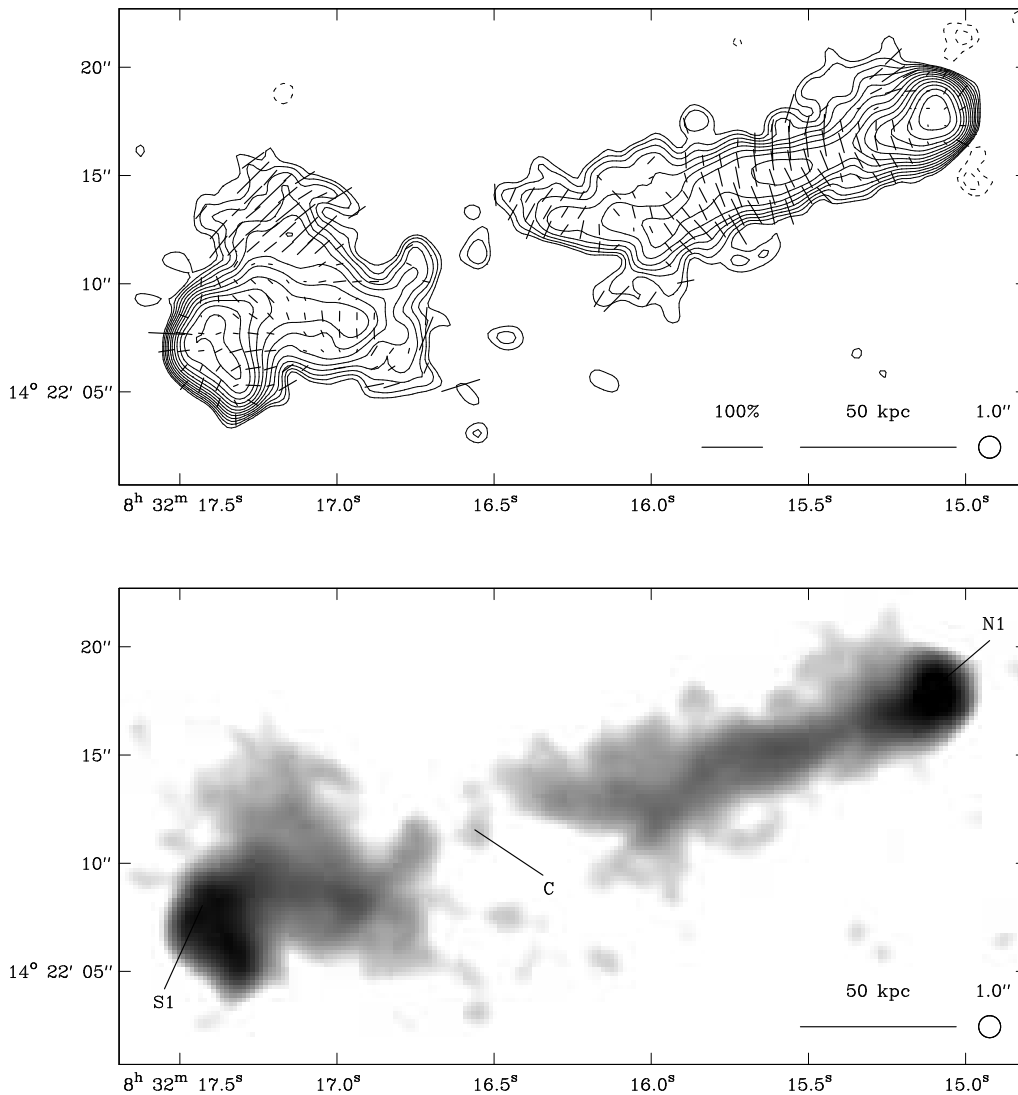


Figure 25. 4C 14.27 at 1.0-arcsec resolution. Contours at $0.090 \times (-\sqrt{2}, -1, 1, \sqrt{2}, 2, \dots)$ mJy beam $^{-1}$. The peak intensity is 7.45 mJy beam $^{-1}$.

(N4;S2) embedded in a larger region of relatively uniform brightness. In the southern lobe a ridge of emission (S1), and in the northern lobe a train of knots (N1 to N3), point back from the peaks towards the core. Additionally the northern lobe contains a second, diffuse, peak at the tip of the region (N5) which is more reminiscent of a hotspot. The presence of jet-like features of roughly equal brightness in both lobes is unusual. It is difficult to judge the reliability of these, however, due to the presence of artefacts at about the same level (e.g. X1) in the images.

3.13 3C 228

Both the northern and southern lobes exhibit large regions of uniform brightness punctuated by abrupt changes in brightness (Fig. 32). In the northern lobe, to the south of the hotspot, there is a region of relatively uniform brightness (N1) and then, to the south of this, a ‘smooth’ region of lower surface brightness just above the noise level. A similar pattern exists in the southern lobe with the regions of uniform

surface brightness S3, (to the north of the hotspot) and S2 (to the north of S3). The images of Burns et al. (1984), at lower resolution and a frequency of 5 GHz, show that both lobes exhibit low brightness bridges that extend back to the core.

The southern jet (Fig. 34) is elongated along the source axis, although unresolved perpendicular to it. The magnetic field is parallel to the source axis along the entire extent of the jet. The jet was detected in previous observations as a slightly elongated peak in the southern lobe (e.g. Burns et al. 1984) but due to the lower resolution of these observations it did not meet the criteria for a jet given by Bridle & Perley (1984).

The northern hotspot (N2; Fig. 33) is distorted and appears to be slightly recessed from the tip of the lobe. There are small elongations to the south east (N3) and south west (N4). Just to the south of the hotspot is a deep dip in the emission (X1).

The southern hotspot (S5) is also distorted with an elongation towards the east. There is a bright, unresolved,

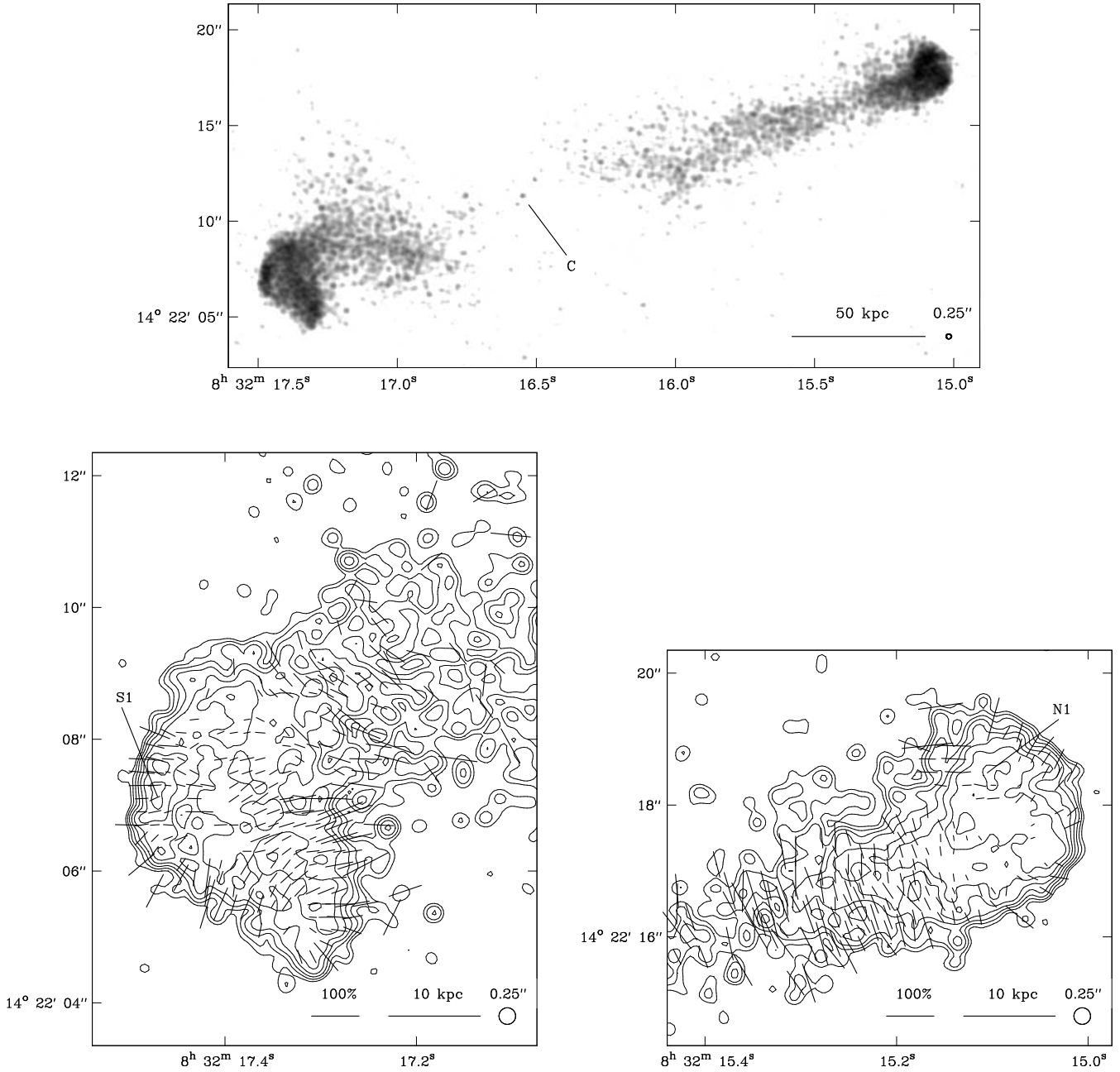


Figure 26. 4C 14.27 at 0.25-arcsec resolution. Contours at $0.055 \times (-1, 1, \sqrt{2}, 2, \dots)$ mJy beam $^{-1}$. Top: Whole source. Bottom left: Southern hotspot. The peak intensity is 0.513 mJy beam $^{-1}$. Bottom right: Northern hotspot. The peak intensity is 0.737 mJy beam $^{-1}$.

peak (S4) which lies just to the north of the hotspot along the core-hotspot axis and may be a hotspot or a jet knot. A faint curving ridge of emission leads back from S4 to the northeast and may also be part of the jet, though it is not aligned with S1 or the core-hotspot axis.

3.14 3C 244.1

Away from the hotspots both the northern and southern lobes are of relatively uniform brightness (Fig. 35) and low-frequency images (Leahy, Bridle & Strom 2000) show a

bridge extending back to the core. At 8 GHz, both lobes are strongly polarized (~ 50 per cent).

The northern hotspot region (Fig. 36) is resolved into two components, N1 and N2. It is unclear which of the two is the primary hotspot. The brighter, more compact, component N1 fulfills most definitions of a primary hotspot and the more diffuse N2 that of a secondary.

In the southern lobe (Fig. 36) the components S2 and S3 fulfill our hotspot criteria, although, as with the northern hotspots, it is not clear which is the primary and which the secondary - we classify S3 as the primary since it is slightly more compact than S2. The nature of the compact feature,

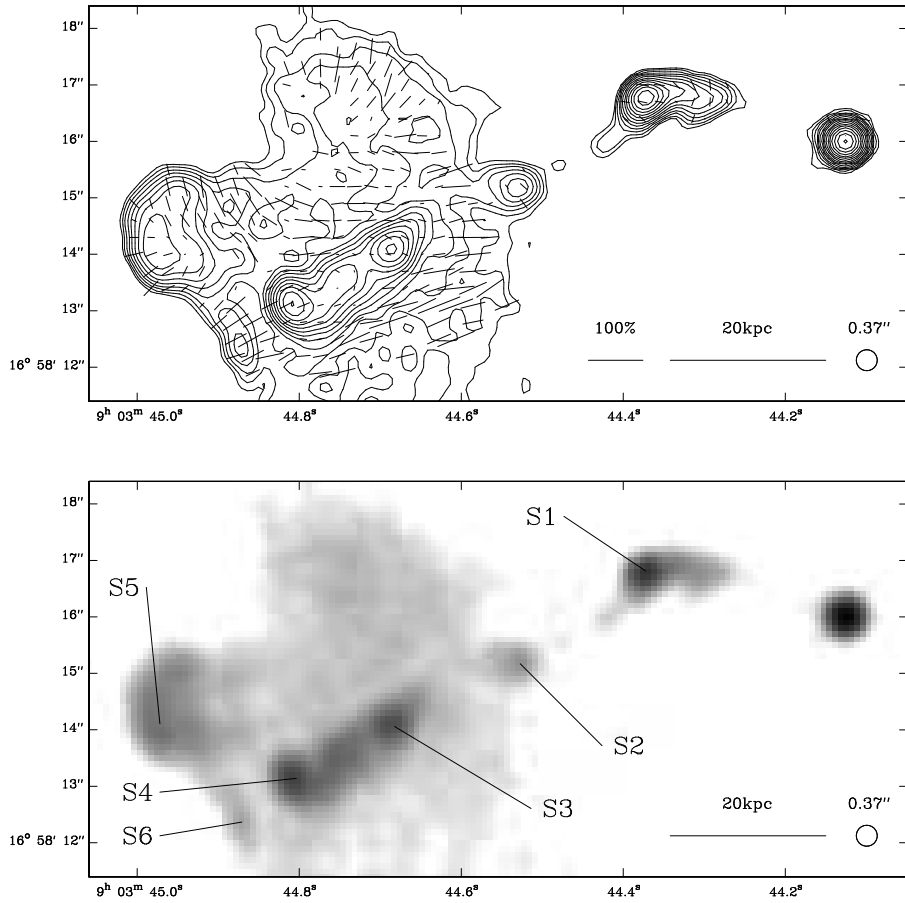


Figure 28. 3C 215 at 5 GHz and 0.37-arcsec resolution. Contours at $0.089 \times (-1, 1, \sqrt{2}, 2, \dots)$ mJy beam $^{-1}$. The peak intensity is 16.4 mJy beam $^{-1}$.

S1, in the lobe is unclear; its high polarization and close alignment with the source axis indicate that it is unlikely to be a background source. It is possible that it represents a jet knot, but there is no other evidence of a jet in this lobe. Fernini, Burns & Perley (1997) and Fernini (2002) also note the presence of the compact feature S1; they comment that neither S2 nor S3 are bright enough to satisfy their criteria as hotspots and they therefore identify S1 as the termination point of the beam. (Fernini (2002) used our A- and B-array data to produce images of 3C 244.1 at similar resolutions; however we have included C- and D-array data in making our images and the noise levels on our maps are about a factor of two lower than his.) Other observations (e.g. Neff, Roberts & Hutchings 1995) show a gap in emission, possibly due to a lack of sensitivity or under-sampling, between S1 and the diffuse region containing S2 and S3, again suggesting that S1 is a feature internal to the lobe rather than the terminating hotspot.

3.15 3C 249.1

3C 249.1 is associated with a quasar. The radio structures of the two lobes are very different from each other; the eastern lobe is more reminiscent of an FR I lobe and the western one comparatively normal for an FR II (Fig. 37).

There is little variation in the surface brightness over the eastern lobe apart from a slight increase along an edge-brightened ridge to the south east (N5). The spectral index is remarkably constant ($\alpha \sim 0.9$) over the entire lobe area (Dennett-Thorpe 1996) rather than steepening away from the tip as expected in FR II sources. Over the whole of the western half of the eastern lobe, both the degree of polarization and the magnetic field direction are approximately constant.

A jet can be followed from the core to a bright, compact, region (N4) at the base of the eastern lobe, often identified as the hotspot (e.g. Bridle et al. 1994). Fig.38 shows several knots (N1, N2 and N3), elongated along the source axis. A region (X1) protrudes perpendicular to this direction from the half way point, a feature noted at different epochs, frequencies and resolutions (e.g. Lonsdale & Morison 1983; Bridle et al. 1994).

The western lobe is relatively featureless. Although some observations (e.g. Bridle et al. 1994) show a plausible counter-jet path (S1), the evidence in the images presented here is inconclusive. There is, however, a definite, although diffuse, hotspot (S2; Fig. 39), significantly recessed from the edges of the lobe.

A wide variety of suggestions have been made to explain the peculiar morphology including a dense cluster

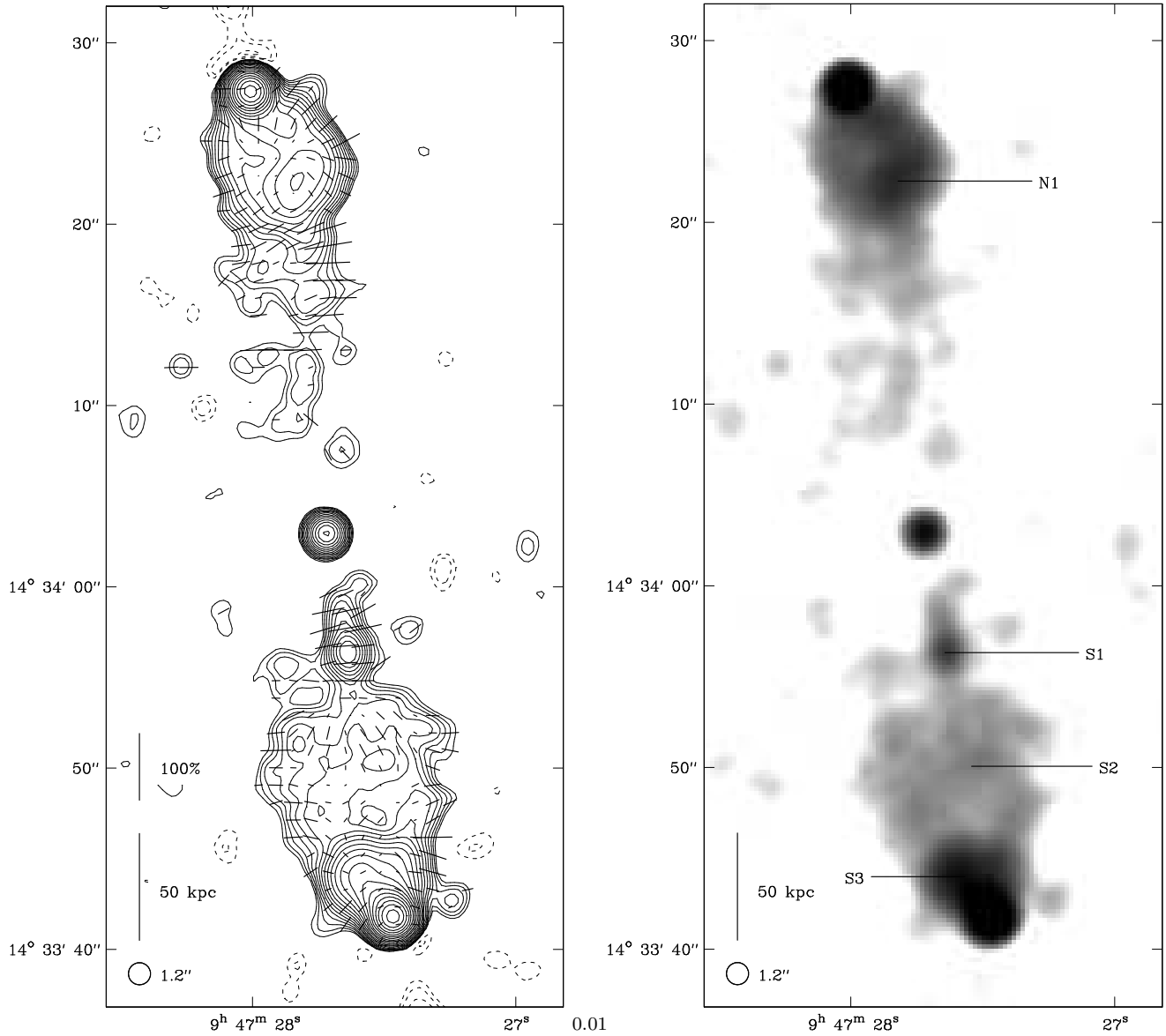


Figure 32. 3C 228 at 1.2-arcsec resolution. Contours at $0.190 \times (-2, -\sqrt{2}, -1, 1, \sqrt{2}, 2, \dots)$ mJy beam $^{-1}$. The peak intensity is 168 mJy beam $^{-1}$.

environment (Hintzen 1984), cooling flows (Crawford, Fabian & Johnstone 1988) or interacting systems (Stockton & MacKenty 1983). The asymmetry in structure has also been used as evidence to promote ‘flip-flop’ models of alternating beams from the central engine (Lonsdale & Morison 1983).

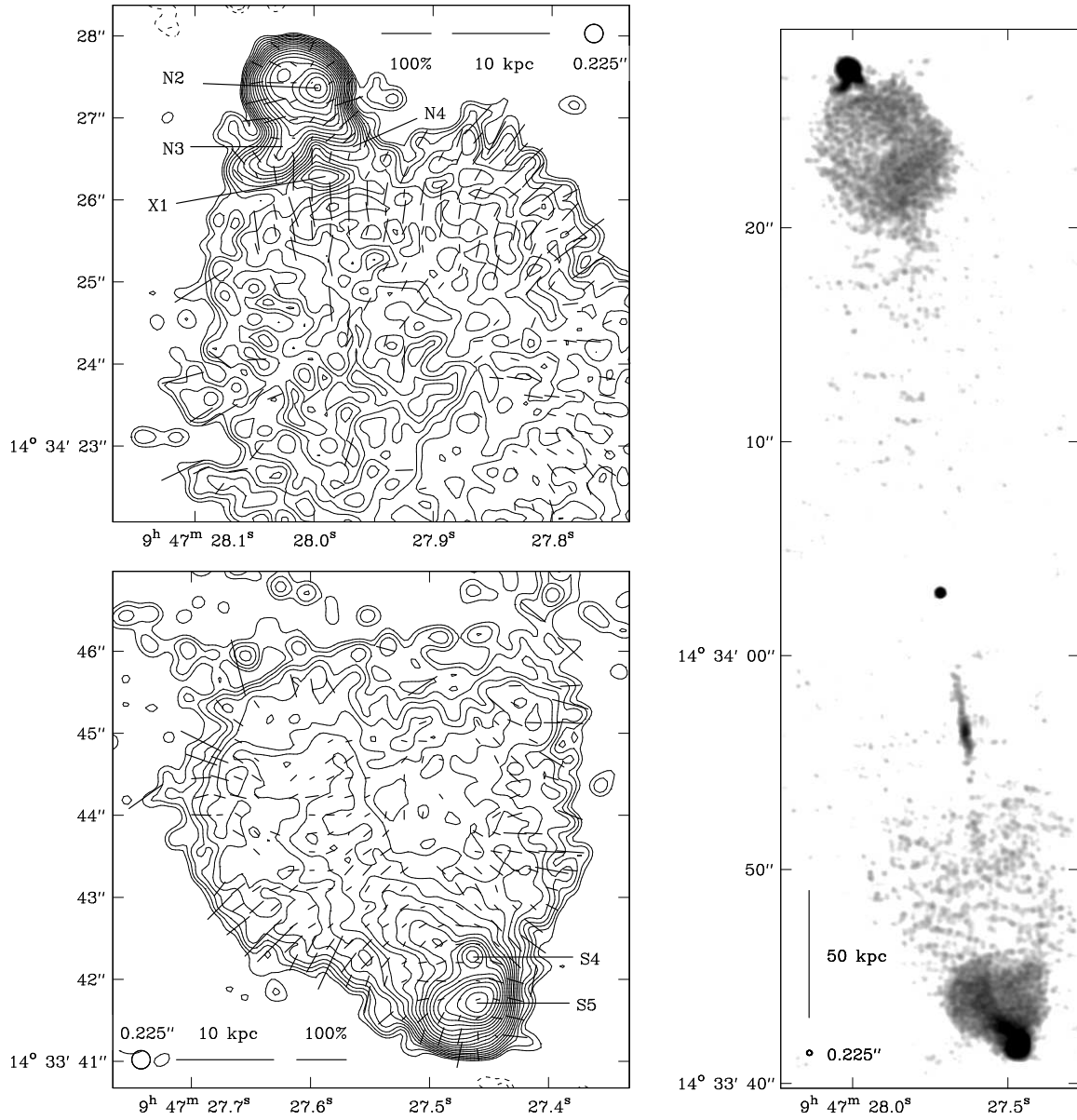


Figure 33. 3C 228 at 0.225-arcsec resolution. Contours at $0.060 \times (-\sqrt{2}, -1, 1, \sqrt{2}, 2, \dots)$ mJy beam $^{-1}$. Top left: Northern hotspot and lobe. The peak intensity is 32.2 mJy beam $^{-1}$. Bottom left: Southern hotspot and lobe. The peak intensity is 40.6 mJy beam $^{-1}$. Right: Whole source.

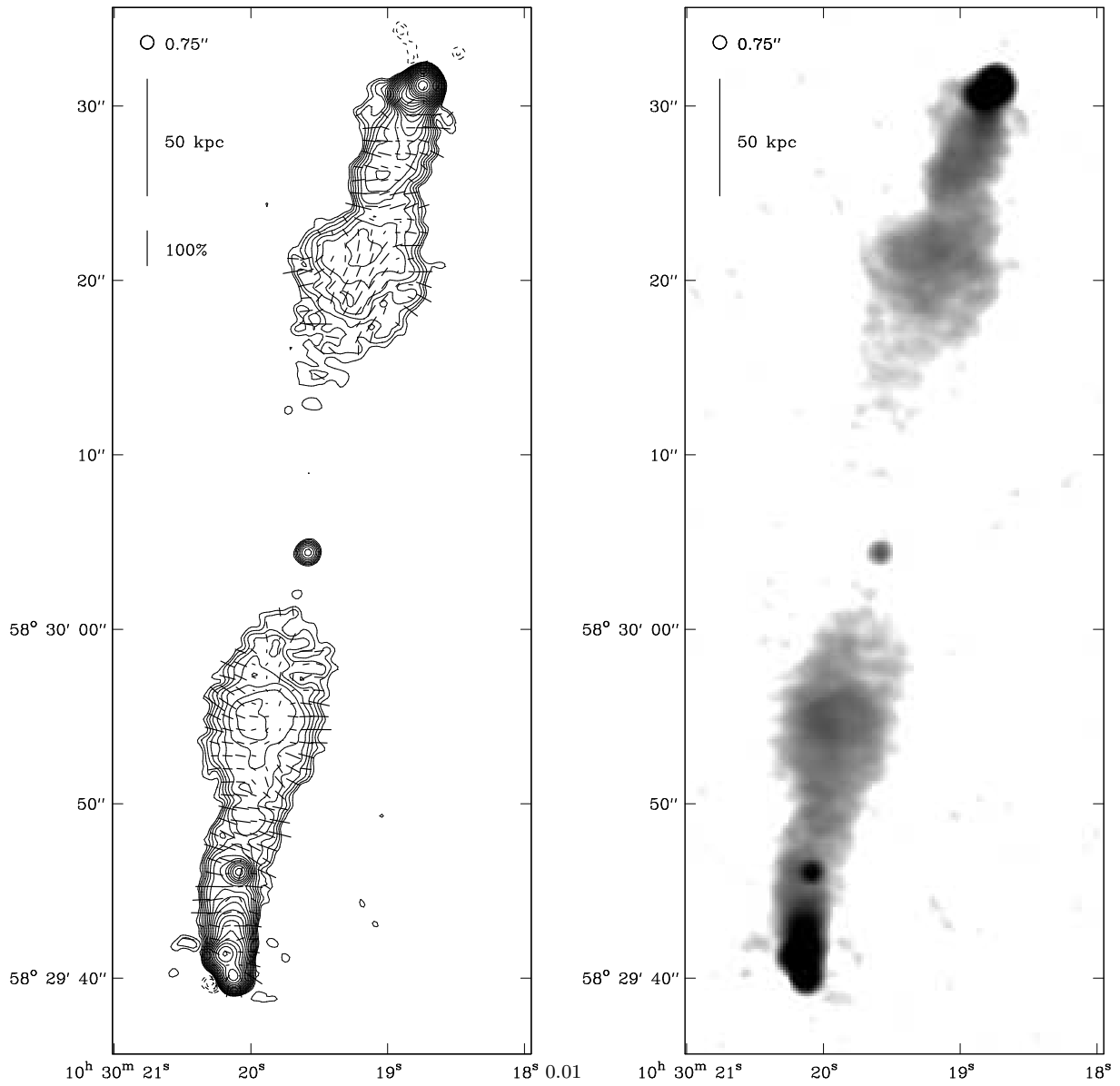


Figure 35. 3C 244.1 at 0.75-arcsec resolution. Contours at $0.100 \times (-2, -\sqrt{2}, -1, 1, \sqrt{2}, 2, \dots)$ mJy beam^{-1} . The peak intensity is $190 \text{ mJy beam}^{-1}$.

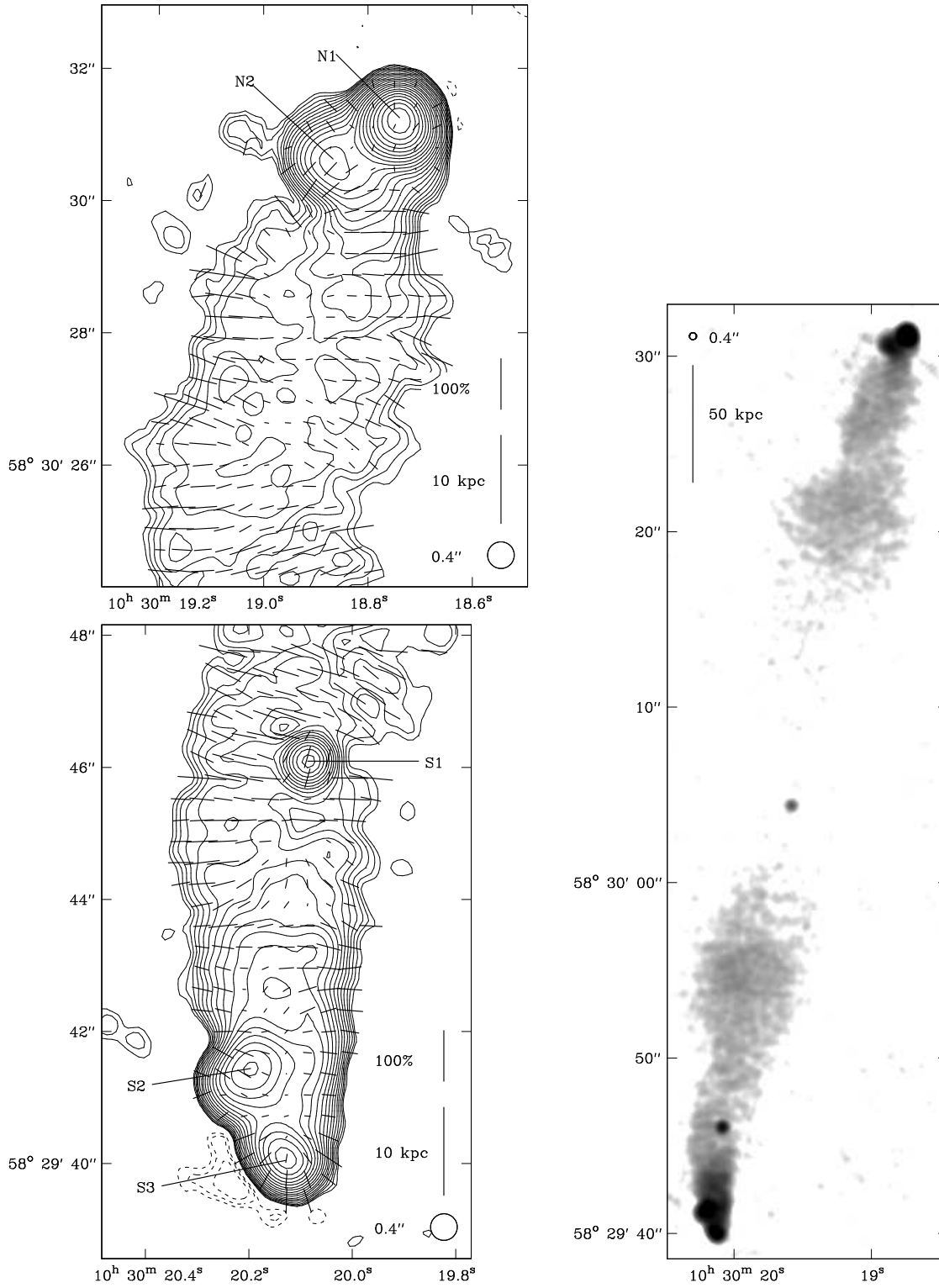


Figure 36. 3C 244.1 at 0.4-arcsec resolution. Contours at $0.065 \times (-2, -\sqrt{2}, -1, 1, \sqrt{2}, 2, \dots)$ mJy beam $^{-1}$. Top left: Northern hotspot and lobe. The peak intensity is 130 mJy beam $^{-1}$. Bottom left: Southern hotspot and lobe. The peak intensity is 20 mJy beam $^{-1}$. Right: Whole source.

3.16 3C 268.3

3C 268.3 is the smallest source in the sample, with an angular size of 1.5 arcsec, corresponding to a linear size of 11 kpc. The 5-GHz image presented here (Fig. 40) is that of Lüdke et al. (1998) and shows a possible radio core, asymmetrically placed towards the northern component.

High-resolution observations (MERLIN + EVN data at 1.6 GHz; Fanti et al. 1985) resolve the northern lobe into a bright, unpolarized, central component with two anti-parallel protrusions. They suggest that this central component is the core, with the two extensions being the jet and counterjet; however, given the core detection of Lüdke et al. (1998), this seems unlikely.

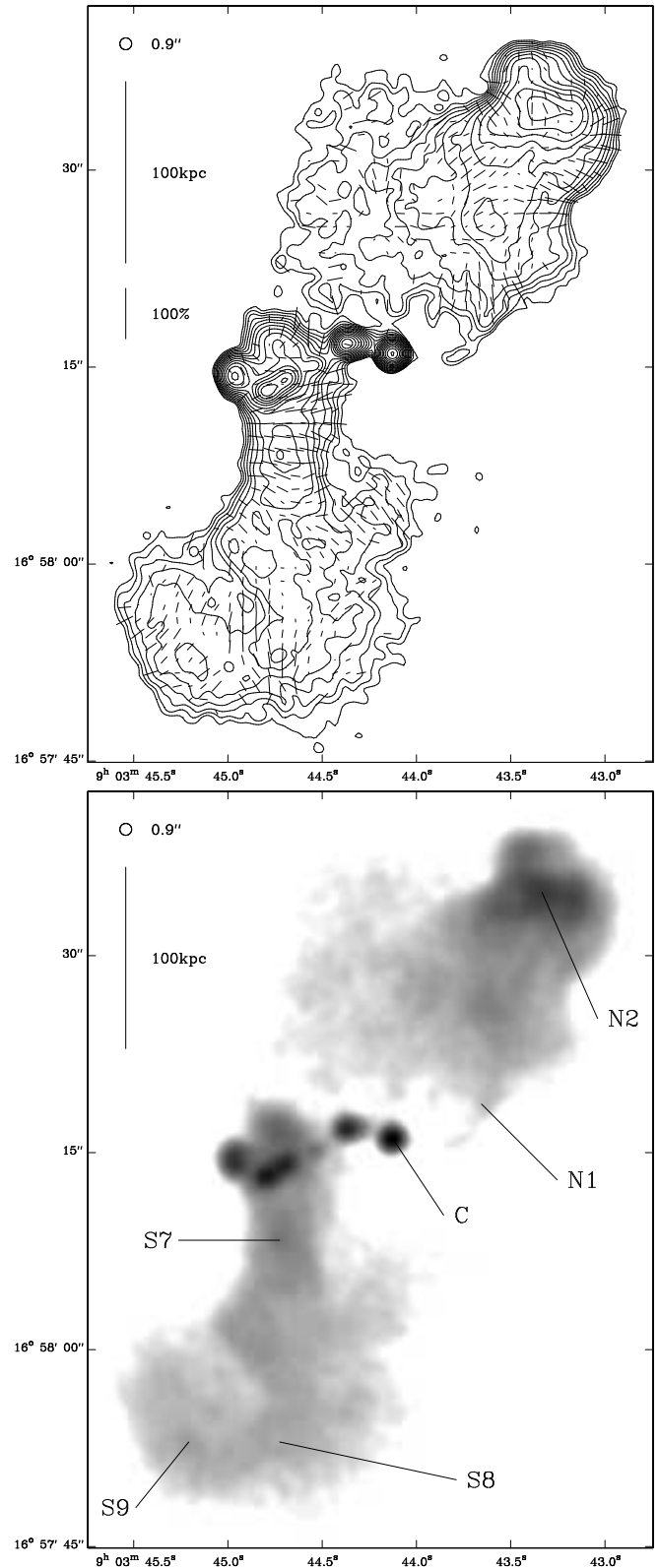


Figure 27. 3C 215 at 5 GHz and 0.9-arcsec resolution. Contours at $0.089 \times (-1, 1, \sqrt{2}, 2, \dots)$ mJy beam $^{-1}$. The peak intensity is 16.5 mJy beam $^{-1}$.

There is an asymmetry in polarization between the two lobes (e.g. Lüdke et al. 1998) with the fainter, more diffuse,

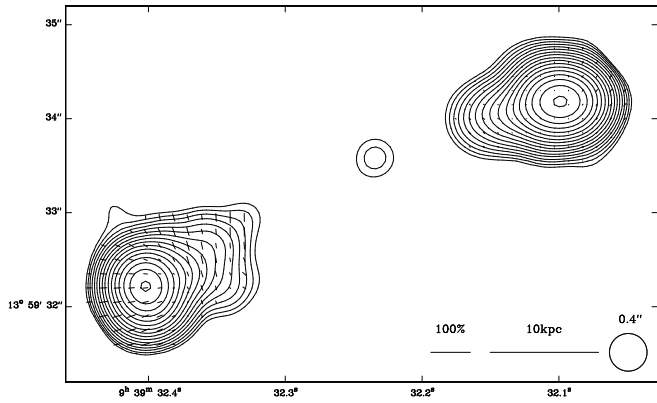


Figure 29. 3C 225B at 5 GHz and 0.4-arcsec resolution. Contours at $0.6 \times (-1, 1, 1.5, 2, 2.5, \dots)$ mJy beam $^{-1}$. The peak intensity is 409 mJy beam $^{-1}$.

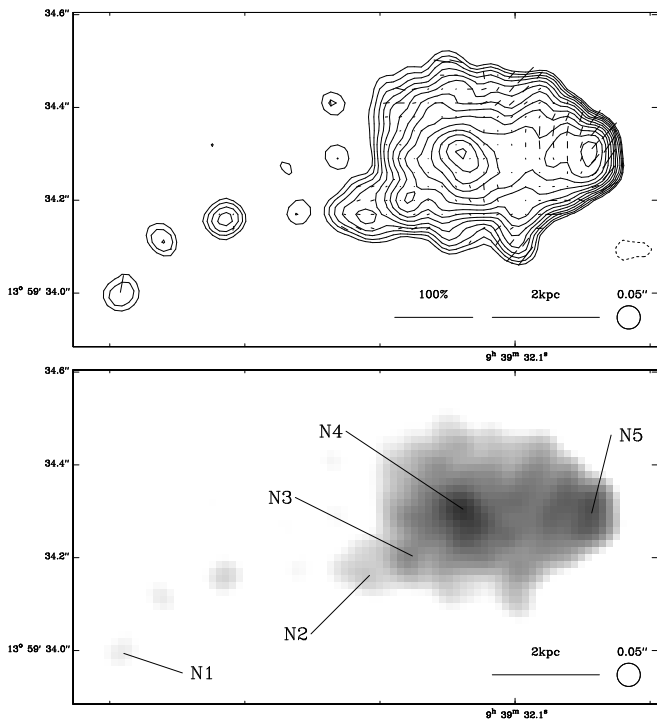


Figure 30. Northern hotspot of 3C 225B at 5 GHz and 0.05-arcsec resolution. Contours at $0.5 \times (-1, 1, \sqrt{2}, 2, \dots)$ mJy beam $^{-1}$. The peak intensity is 48.0 mJy beam $^{-1}$.

southern lobe being more polarized. This, and the possible asymmetry in lobe length, may be a reflection of large variations in the density of the surrounding galactic medium.

3.17 3C 274.1

3C 274.1 is one of the largest sources in the sample and was mapped using three pointing centres. The image at 1.0-arcsec resolution (Fig. 41) shows low-brightness emission extending back towards the core. In lower-frequency, lower-resolution images (e.g. 1.6 GHz; Leahy & Williams 1984) a complete bridge is present, which is deflected near the centre to form an X-shape.

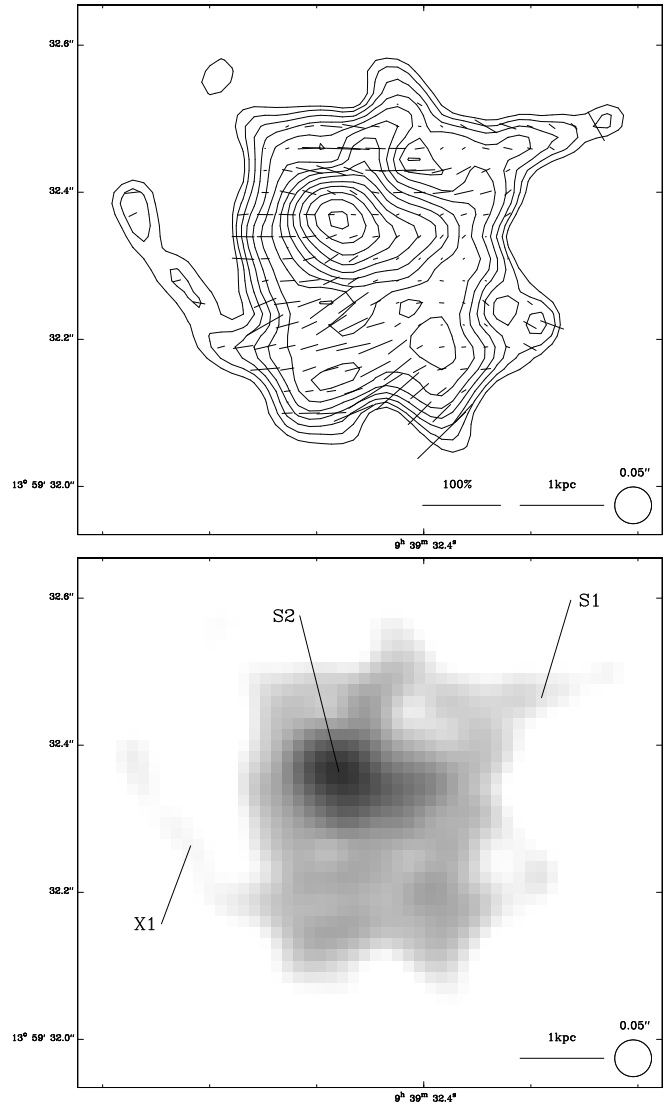


Figure 31. Southern hotspot of 3C 225B at 5 GHz and 0.05-arcsec resolution. Contours at $0.5 \times (-1, 1, \sqrt{2}, 2, \dots)$ mJy beam $^{-1}$. The peak intensity is 47.5 mJy beam $^{-1}$.

The end of the northern lobe (Fig. 42) consists of hotspots, N1 and N2, embedded in a region whose brightness drops abruptly to the north and south of the hotspots and ahead of them to the east; there is further low-brightness emission, N3, to the east of the sharp eastern edge. The northern lobe is uniformly polarized at the 40 per cent level with the magnetic field parallel to the source axis. In the hotspot region the magnetic field runs parallel to the edge. The image at 0.25-arcsec resolution (Fig. 42, below) shows that there is a striking band of unpolarized emission to the north of N1.

The relaxed southern hotspot (Fig. 43) shows two diffuse features (S1 and S2) which are morphologically quite similar; however, due to its location, S2 is identified as the primary hotspot. Both are resolved out at 0.25-arcsec resolution. As with the northern lobe the southern lobe is highly polarized (~ 40 per cent) with the magnetic field parallel to the source axis except around the edge of the hotspot re-

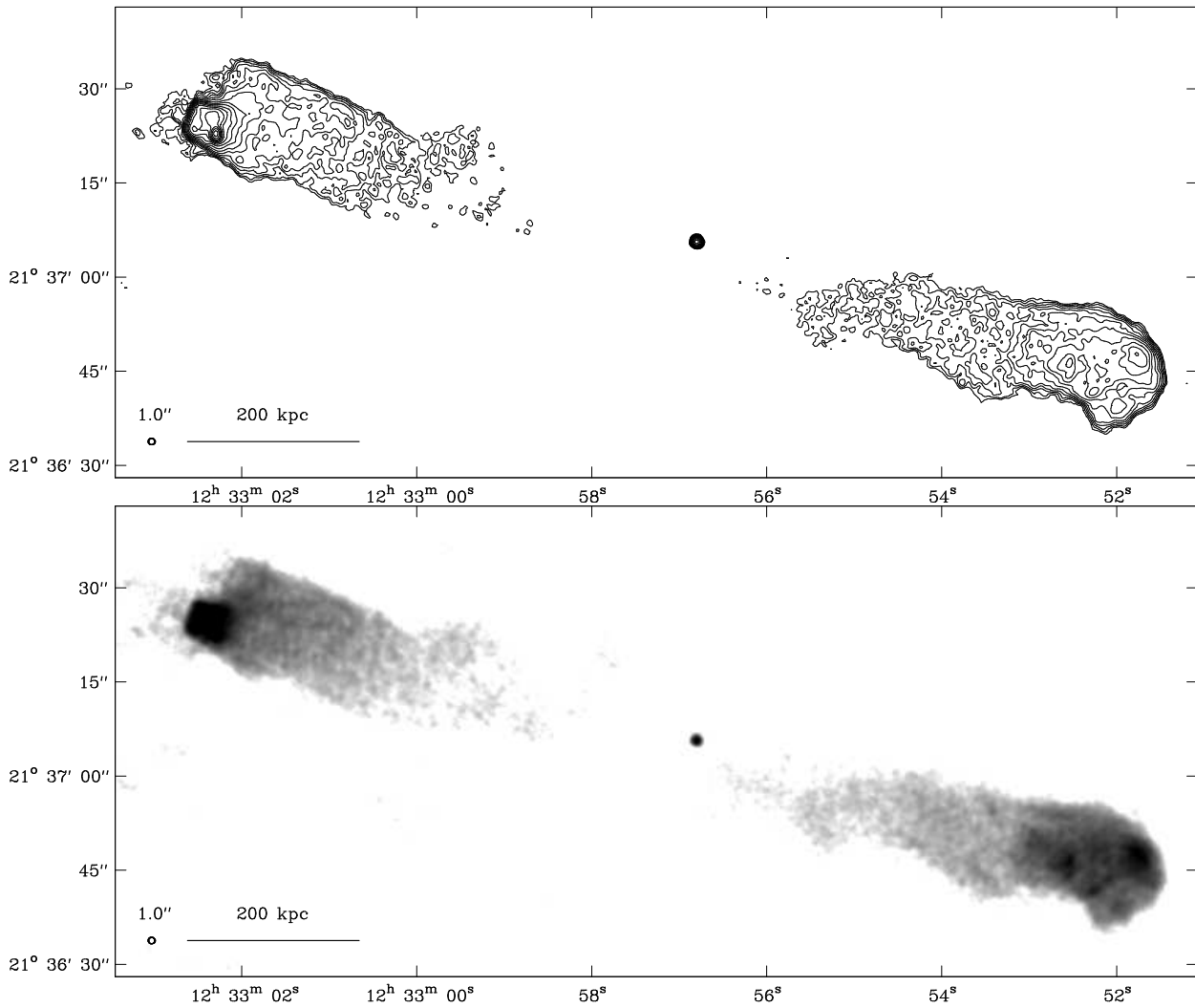


Figure 41. 3C 274.1 at 1.0-arcsec resolution. Contours at $0.060 \times (-1, 1, \sqrt{2}, 2, \dots)$ mJy beam $^{-1}$. The peak intensity is 13.4 mJy beam $^{-1}$.

gion where it runs parallel to the edge; the region close to the hotspot is also relatively weakly polarized.

3.18 3C 275.1

3C 275.1 is associated with a quasar. Only the small-scale, high-brightness structure is visible in the image shown here (Figs 44 and 45). However, lower-resolution maps at 1.4 and 5 GHz (Liu & Pooley 1990) indicate that this structure is embedded in a steep-spectrum low-brightness envelope about 25 arcsec in length and 10 arcsec wide.

The most striking feature of this source is the large angle between the axes joining the core to the northern and southern components. A straight, knotty, jet (N1 to N2) runs from the core to the northern component (Fig. 44). The inner 5 kpc of the jet is aligned approximately north-south (roughly along the axis joining the core and the southern hotspot); in the next ~ 5 kpc the jet curves significantly and then continues in roughly a straight line to the bright northern component. This component contains a pronounced S-shaped bend (N2,N3); there is then a second, less

pronounced, peak in emission (N4) to the northwest of the main peak.

The southern component contains a relaxed hotspot (S2), extended perpendicular to the core-hotspot axis. The core appears slightly extended to the south and there is an adjacent knot of emission to the south of this (both labelled S1 in Fig. 44) which present possible evidence for a counterjet; however the large negative imaging artefacts in this region mean that this suggestion must be treated with caution.

Several authors have argued that the source lies in a dense cluster which could account for its distorted shape (Stocke, Burns & Christiansen 1985, Ellingson, Yee & Green 1991, Hardcastle & Worrall 1999, Crawford & Fabian 2003). Hintzen, Boeshaar & Scott (1981) suggested that the S-shaped bend in the bright northern component could be due to the interaction between the quasar and a companion galaxy. However, Liu & Pooley (1990) note that this ‘interacting’ galaxy is probably in the foreground, although there is a galaxy near the southern component which may be interacting with the southern lobe.

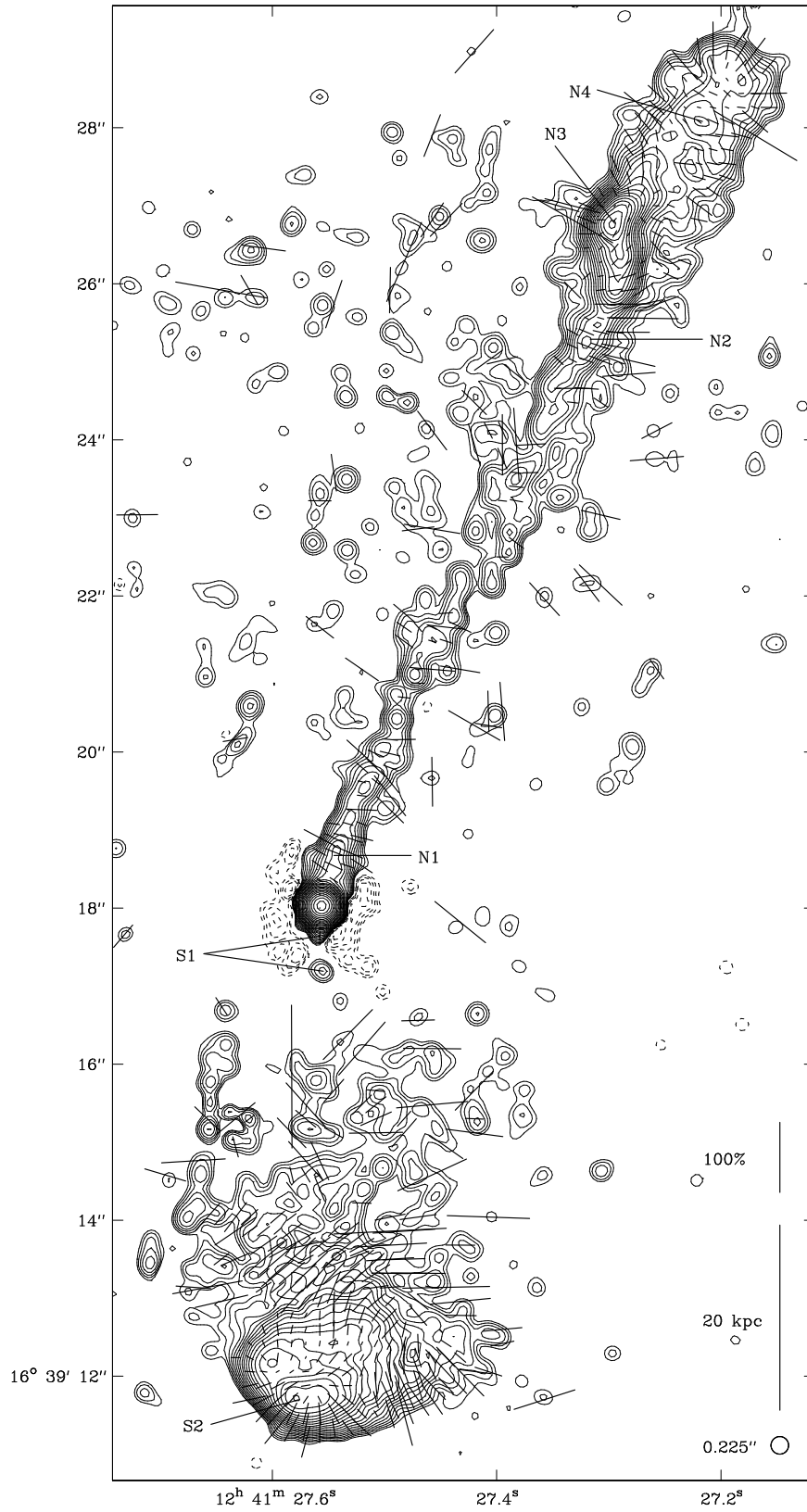


Figure 44. 3C 275.1 at 0.225-arcsec resolution. Contours at $0.040 \times (\dots, -2, -\sqrt{2}, -1, 1, \sqrt{2}, 2, \dots)$ mJy beam $^{-1}$. The peak intensity is 194 mJy beam $^{-1}$.

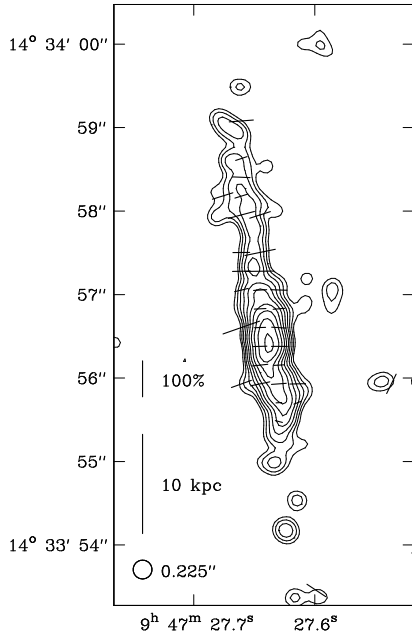


Figure 34. Southern jet of 3C 228 at 0.225-arcsec resolution. Contours at $0.060 \times (-1, 1, \sqrt{2}, 2, \dots)$ mJy beam $^{-1}$. The peak intensity is 1.46 mJy beam $^{-1}$.

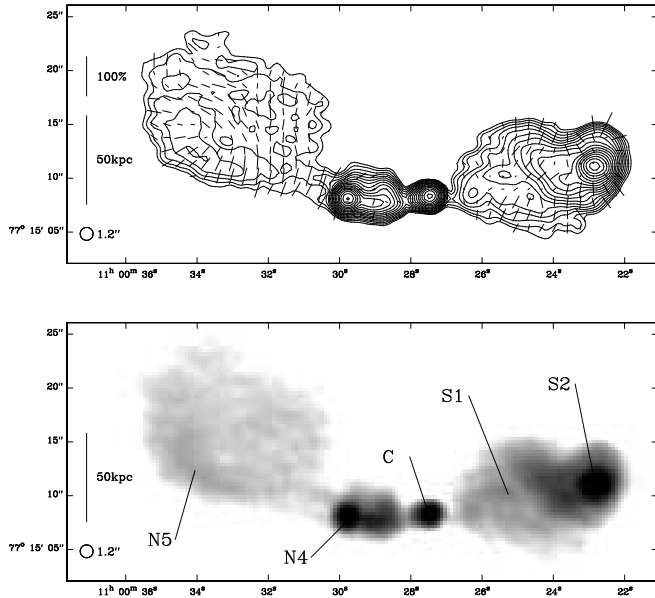


Figure 37. 3C 249.1 at 5 GHz and 1.2-arcsec resolution. Contours at $0.354 \times (-1, 1, \sqrt{2}, 2, \dots)$ mJy beam $^{-1}$. The peak intensity is 107 mJy beam $^{-1}$.

3.19 3C 295

3C 295 lies within the X-ray core of a dense cluster causing strong Faraday rotation (Perley & Taylor 1991). No extended structure, such as a radio halo, is seen even at very low frequencies (151 MHz; Akujor, Spencer & Wilkinson 1990).

The 8.4-GHz map of 3C 295, at a resolution of 0.25 arcsec (Fig. 47), was provided by Perley (private communica-

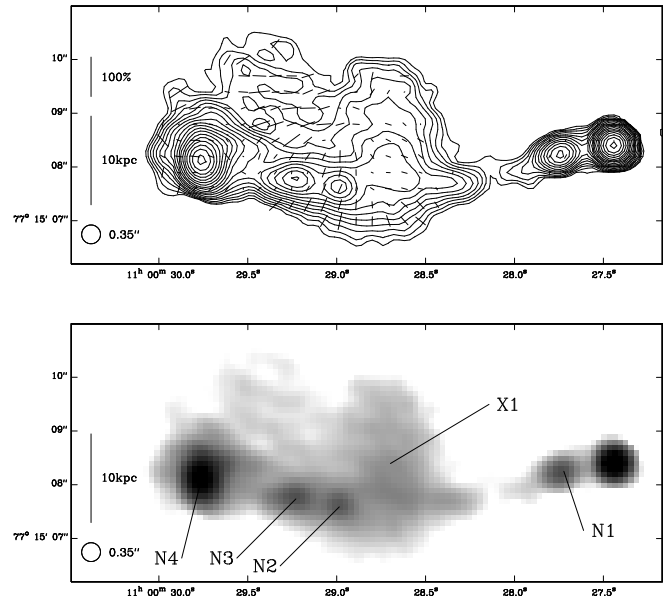


Figure 38. Jet region of 3C 249.1 at 5 GHz and 0.35-arcsec resolution. Contours at $0.177 \times (-1, 1, \sqrt{2}, 2, \dots)$ mJy beam $^{-1}$. The peak intensity is 70.4 mJy beam $^{-1}$.

tion). We include an image made with the same data at a resolution of 0.175 arcsec (Fig. 46).

Set slightly back from the compact northern hotspot (N2) is a small perpendicular outcrop (N3). VLBA studies show a lower brightness region of emission elongated along the axis joining the two components (Taylor & Perley 1992). Chandra observations also show X-ray emission coincident with both hotspots and extended emission to the south west of the northern lobe (Harris et al. 2000). A faint ridge of emission (N1) leads from the core towards the northern hotspot; however, the higher resolution observations of Perley & Taylor (1991) show that this does not represent a jet.

The southern lobe contains a compact hotspot, S1, slightly elongated along the source axis, leading to a perpendicular ridge of emission, S2. High resolution imaging of the southern hotspot (e.g. Taylor & Perley, 1992) shows that it is resolved into a diffuse S-shape. The arc of emission across the lobe could represent the position of a bow-shock indicating its confinement by a dense external gas. Additionally the southern lobe is sharply bounded along all edges with a large gap between itself and the core suggestive of a confining medium. Brunetti et al. (2001a) report that a weak jet has been detected with MERLIN in the southern lobe.

3.20 3C 299

Due to the large asymmetry in brightness between the two lobes of 3C 299, the western lobe was not detected at first (e.g. Laing 1981). In addition the position of the proposed identification was close to the bright eastern component. As a result, much of the earlier literature assumes that 3C 299 is a CSS source consisting of only the eastern region. However, when Liu & Pooley (1991) and van Breugel et al. (1992) detected a central radio core the source was re-classified as an FR II source.

The core (C) is clearly detected on the VLA A-

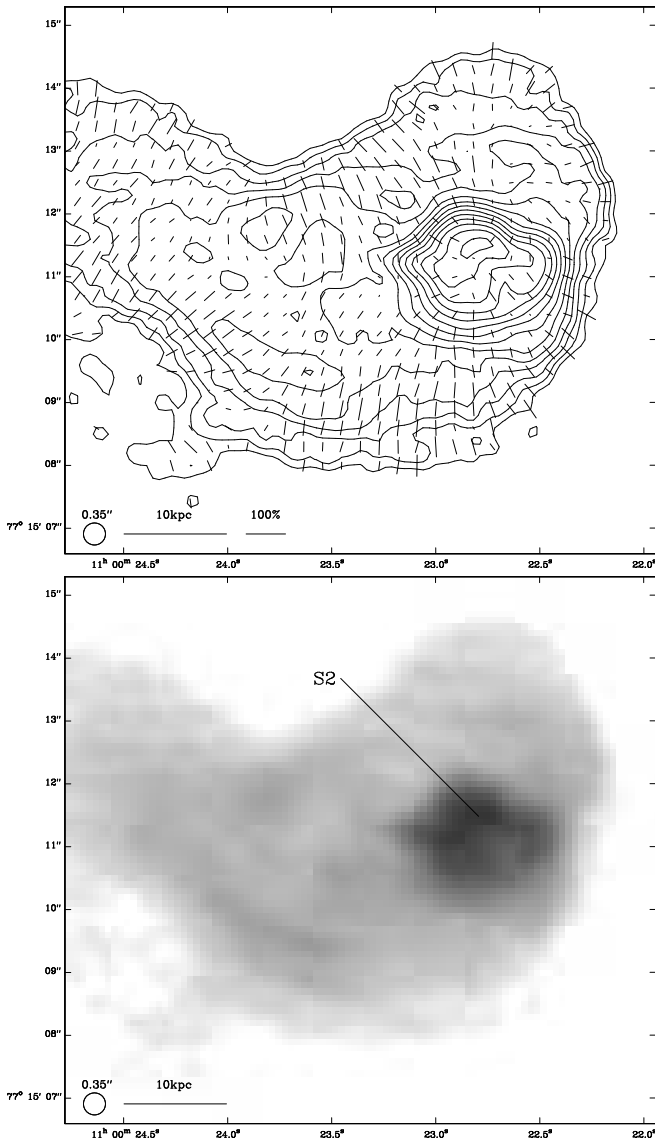


Figure 39. Western lobe of 3C 249.1 at 5 GHz and 0.35-arcsec resolution. Contours at $0.177 \times (-1, 1, \sqrt{2}, 2, \dots)$ mJy beam $^{-1}$. The peak intensity is 17.3 mJy beam $^{-1}$.

configuration image presented here (Fig. 48). No bridge emission is detected in the lower-resolution images, even at 1.4 GHz (Liu & Pooley 1991).

Our MERLIN observations of the northern hotspot region (Fig. 49 above) show three nearly co-linear components (N1, N2 and N3) on an elliptical background. N3 is identified as the primary hotspot and the components N1 and N2 could either be other hotspot regions or jet knots; the feature X1 is also a possible secondary hotspot. Other high-resolution images of this region, at a range of frequencies from 1.7 GHz (Spencer et al. 1991) to 15 GHz (van Breugel et al. 1992), show very similar structure, indicating a uniform spectrum. Both the VLA and MERLIN images show that the northern hotspot region is very weakly polarized.

The component S1 in the southern lobe is slightly elongated along the source axis and coincides with a feature on the lower-resolution maps of Liu & Pooley (1991). Much of the flux from the southern lobe is resolved in the MER-

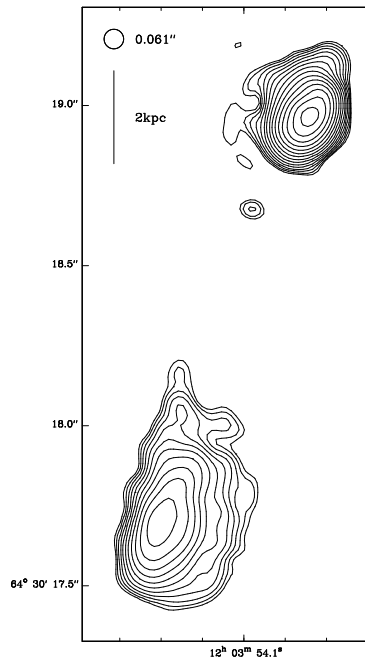


Figure 40. 3C 268.3 at 5 GHz and 0.061-arcsec resolution. Contours at $0.5 \times (-1, 1, 1.5, 2, 2.5, \dots)$ mJy beam $^{-1}$. The peak intensity is mJy beam $^{-1}$. (Image provided by E. Lüdke.)

LIN image (Fig. 49 below) of the region; however, there is a bright, elliptical hotspot which is strongly polarized (~ 50 per cent).

Optical images, in emission lines (McCarthy, Spinrad & van Breugel 1995) and *HST* R-band (de Koff et al. 1996), show a high-density cloud coincident with the position of the northern lobe which may account for the overall asymmetry of the source and for the very low polarization in the northern lobe.

3.21 3C 330

The low-resolution structure of 3C 330 is that of a canonical FR II radio source with compact hotspots at the ends of lobes which fade smoothly back towards the central source (Fig. 50). A weak core is coincident with the position of the optical identification.

High-resolution images (Fig. 51) confirm the existence of the core and show that both hotspot regions are complex. The tip of the northern lobe is elongated and contains a compact hotspot (N3) with a bright tail; Fernini, Burns & Perley (1997) and Fernini (2002) note this feature does not qualify as a hotspot according to the criteria defined by Bridle et al. (1994). (Fernini (2002) used our A- and B-array data to produce images of 3C 330 at similar resolutions; however we have included C- and D-array data in making our images and the noise levels on our maps are about a factor of two lower than his.) The southern lobe shows three distinct regions (S1, S2 and S3) which could all be hotspot candidates; from their 5-GHz images Fernini, Burns & Perley (1997) again note that none of these features qualified as hotspots. However, S3 is brighter and more compact than the other two so that on this basis we have identified it as the primary hotspot; using the 8.4-GHz data at a similar resolution Fernini

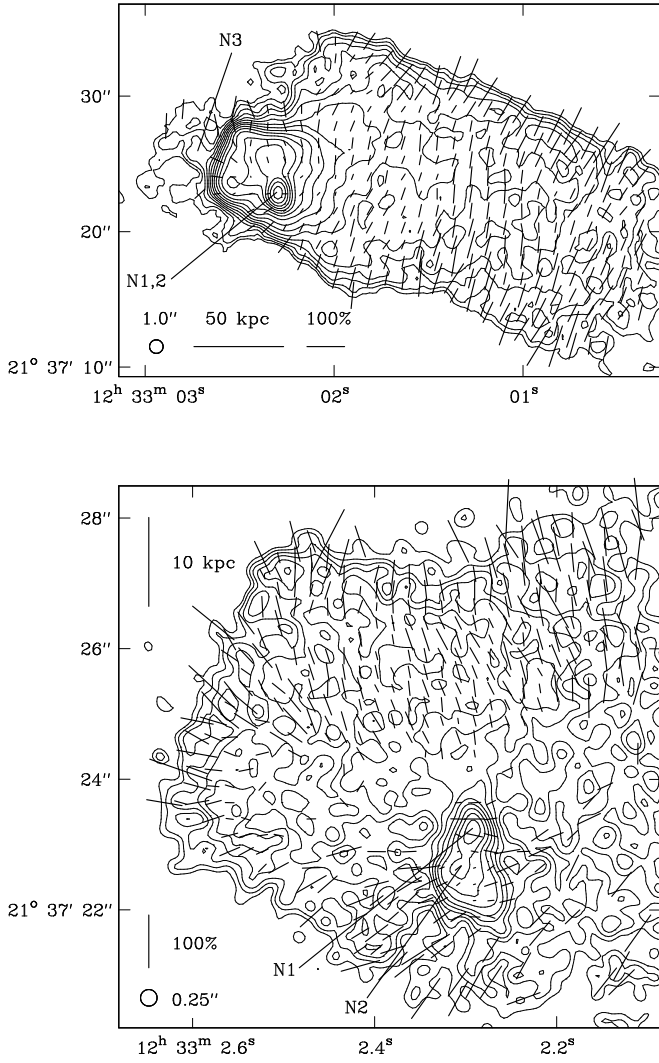


Figure 42. Northern tip of 3C 274.1. Above: At 1.0-arcsec resolution, contours at $0.060 \times (-1, 1, \sqrt{2}, 2, \dots)$ mJy beam⁻¹. The peak intensity is 13.4 mJy beam⁻¹. Below: At 0.25-arcsec resolution, contours at $0.070 \times (-1, 1, \sqrt{2}, 2, \dots)$ mJy beam⁻¹. The peak intensity is 2.8 mJy beam⁻¹.

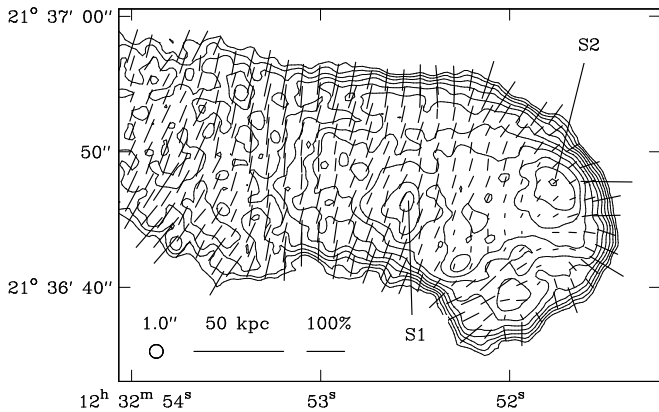


Figure 43. Southern tip of 3C 274.1 at 1.0-arcsec resolution. Contours at $0.060 \times (-1, 1, \sqrt{2}, 2, \dots)$ mJy beam⁻¹. The peak intensity is 1.98 mJy beam⁻¹.

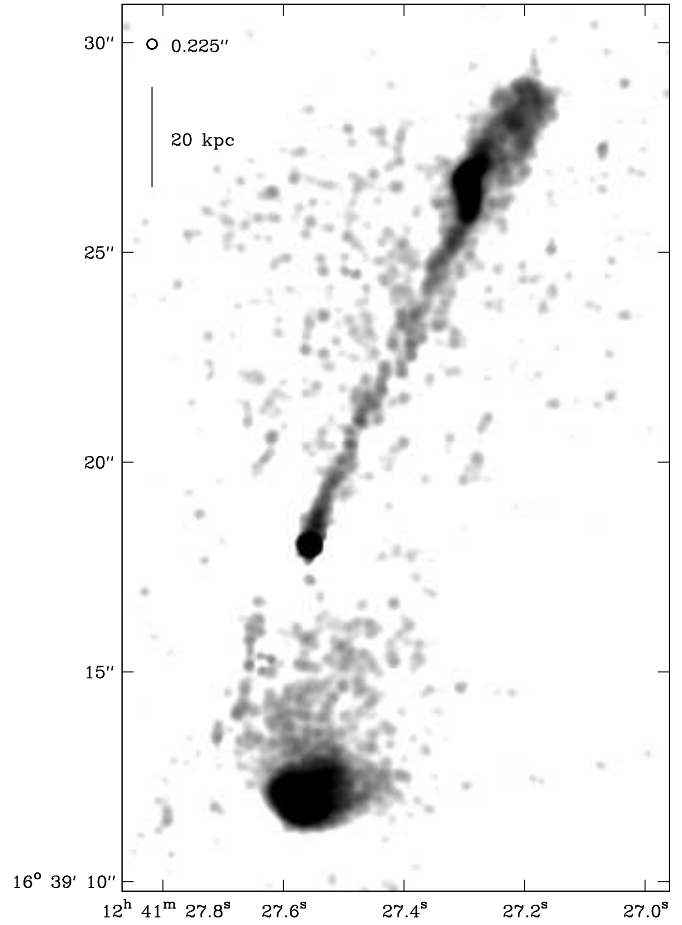


Figure 45. 3C 275.1 at 0.225-arcsec resolution.

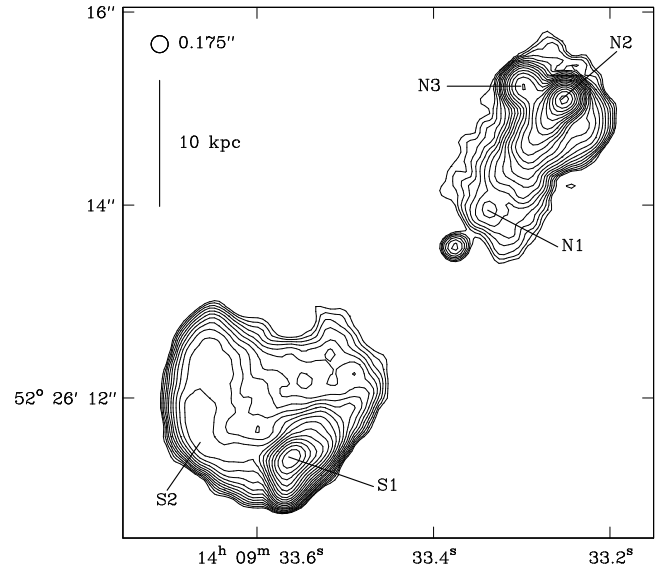


Figure 46. 3C 295 at 0.175-arcsec resolution. Contours at $0.5 \times (-1, 1, \sqrt{2}, 2, \dots)$ mJy beam⁻¹. The peak intensity is 584 mJy beam⁻¹.

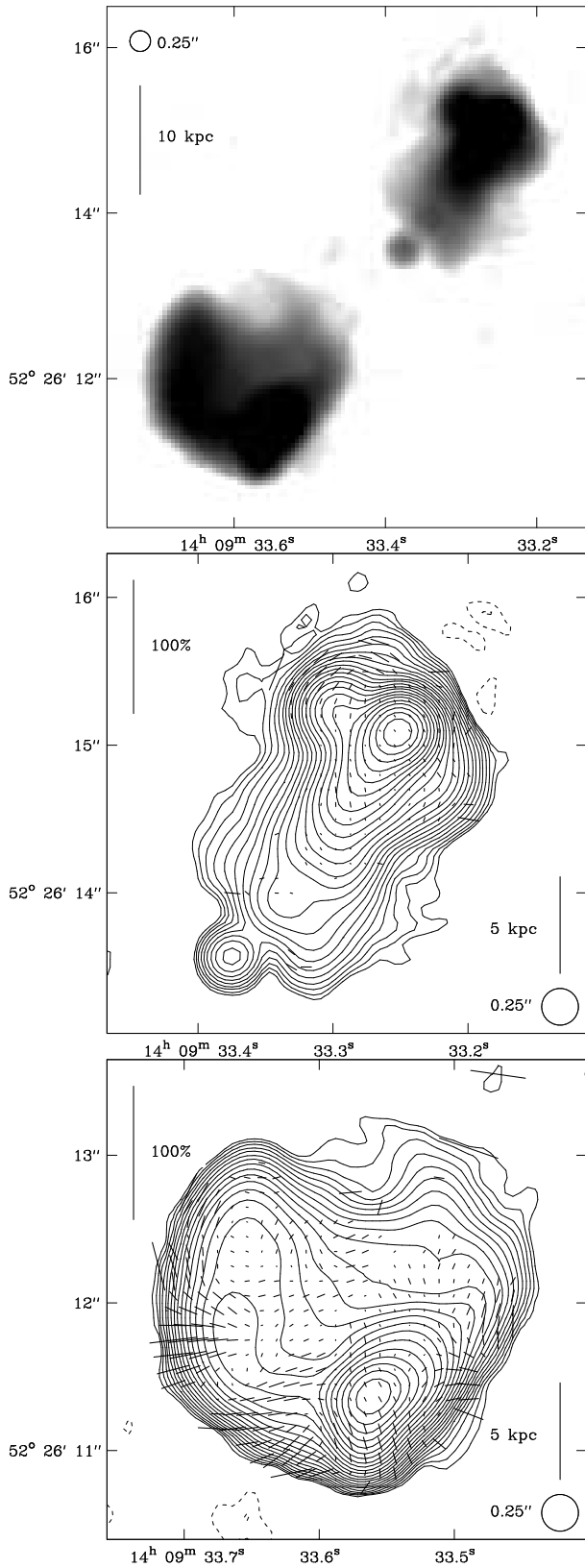


Figure 47. 3C 295 at 0.25-arcsec resolution. Contours at $0.25 \times (-\sqrt{2}, -1, 1, \sqrt{2}, 2, \dots)$ mJy beam $^{-1}$. (Image provided by R. Perley.) Top: Whole source. Middle: Northern lobe. The peak intensity is 684 mJy beam $^{-1}$. Bottom: Southern lobe. The peak intensity is 488 mJy beam $^{-1}$.

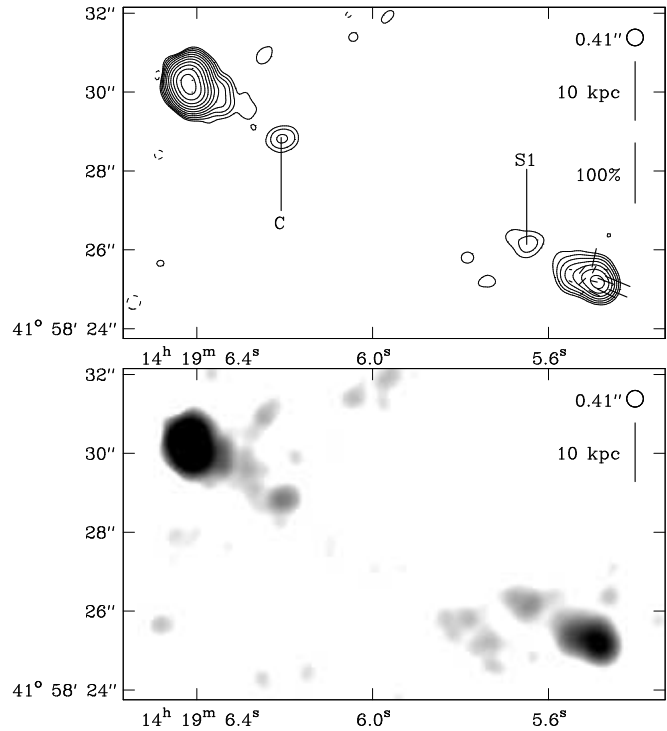


Figure 48. 3C 299 at 5 GHz and 0.41-arcsec resolution. Contours at $0.33 \times (-1, 1, 2, 4, \dots)$ mJy beam $^{-1}$. The peak intensity is 519 mJy beam $^{-1}$.

(2002) comments that this component does qualify as a hotspot according to the criteria set out by Bridle et al. (1994). S1 and S2 may both be secondary hotspots; alternatively, one or other of them may be a jet knot. The hotspot regions in both lobes share an S-shaped symmetry. Set back from the primary hotspots (N3, S3), the emission structure shows evidence for sharp bends at N2/S2 and N1/S1.

There is a high degree of order in the polarization angles in lobes. At low resolution the percentage polarizations of both lobes are roughly the same at ~ 25 per cent; however, the high resolution images of the hotspots show a greater polarization asymmetry (northern ~ 60 per cent, southern ~ 40 per cent).

Hardcastle et al. (2002) have detected X-rays from 3C 330 with Chandra. There are compact X-ray components coincident with the hotspots N3 and S3, which they attribute to synchrotron self-Compton emission. There is also extended emission from the lobes, which they propose is due to inverse Compton scattering of the microwave background radiation, and an even more extended X-ray component, which provides evidence that 3C330 is in a group or cluster.

3.22 3C 334

3C 334 is associated with a quasar. It has a bright one-sided jet (Fig. 52) which has been observed extensively (see Table 4).

The northern lobe has a plume to the south but is otherwise sharply bounded. There is a notable gap between the lobe emission and the core. Higher resolution images (Fig. 53) show a trail of emission (N1, N2 to N3), which could be classed as a counter-jet, leading to a diffuse hot-

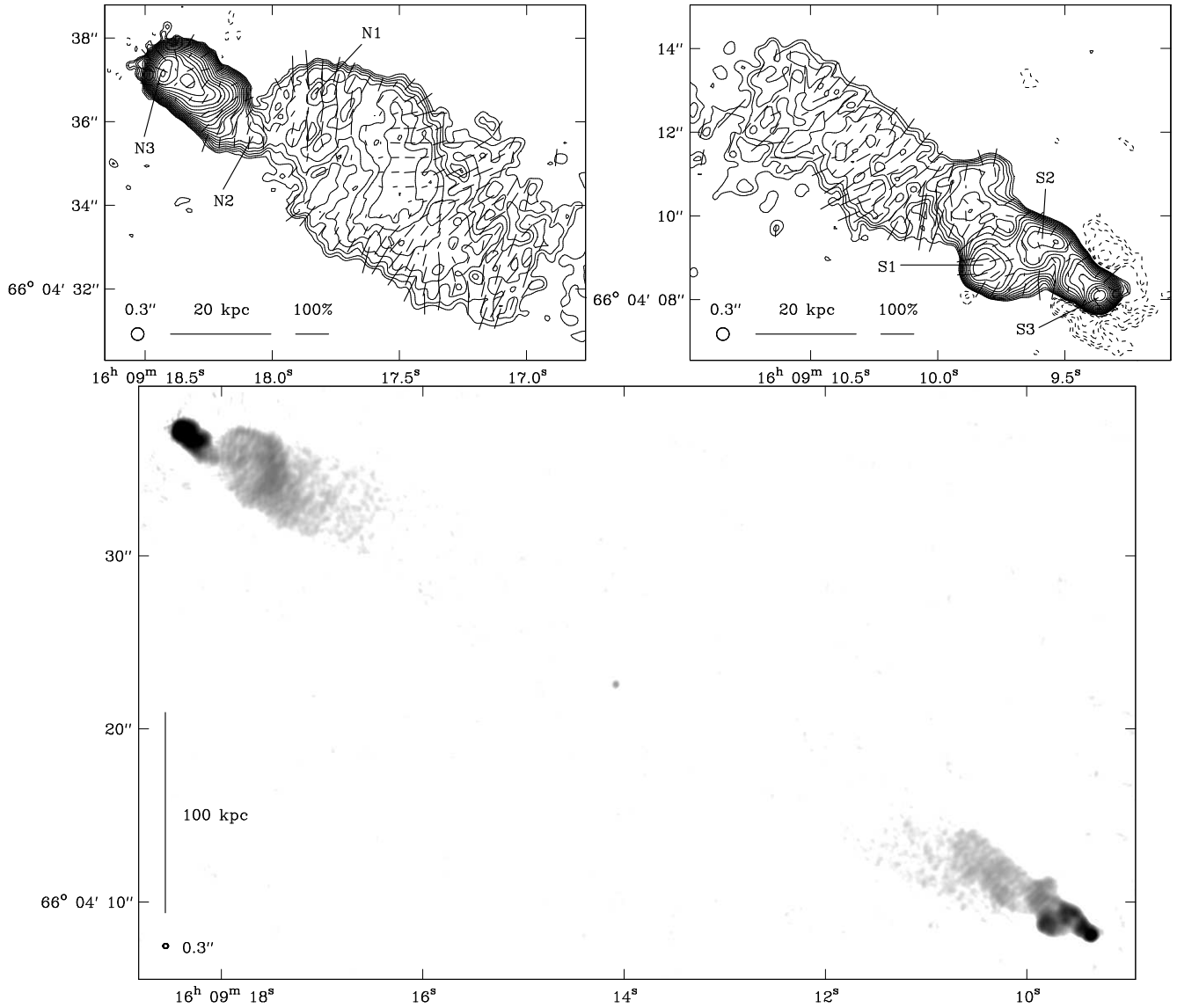


Figure 51. 3C 330 at 0.3-arcsec resolution. Contours at $0.110 \times (\dots, -2, \sqrt{2}, -1, 1, \sqrt{2}, 2, \dots)$ mJy beam $^{-1}$. Above left: Northern hotspot. The peak intensity is 119 mJy beam $^{-1}$. Above right: Southern hotspot. The peak intensity is 55.5 mJy beam $^{-1}$. Below: Whole source.

spot at N4. A further feature (N5) leads from the hotspot towards the plume.

The southern jet is straight for approximately three quarters of its length before bending smoothly to the east. In the image shown here (Fig. 54) the jet shows weak evidence for oscillation in the plane of the sky for the first 10 kpc as suggested by Bridle et al. (1994). The jet appears to end at a hotspot at S3, although a clear trail of emission (S4, S5) leads on from this position curving back again towards a compact region (S6) at the edge of the lobe. This point is edge-brightened and arcs round to yet another bright region at S7. Lower-frequency observations (e.g. Dennett-Thorpe 1996) show the southern lobe extends further back along the northern edge than shown here, but does not reach back to the core.

A weak, but highly polarized, curved structure (X1) runs almost parallel to the main jet close to the region where

it bends (S2). This feature appears in the map of Bridle et al. (1994) and is therefore unlikely to be an imaging artefact.

The core is variable both at radio wavelengths and in the optical. Super-luminal motion has been detected (Hough et al. 1992) although the speeds inferred do not provide strong constraints on the angle to the line of sight.

3.23 3C 341

The low-resolution image of 3C 341 (Fig. 55) shows that both lobes are strongly polarized (~ 50 per cent) with the magnetic field parallel to the lobe axis along almost the whole source. The magnetic field is, however, perpendicular to the lobe axis in a narrow region in the southern lobe close to the core, possibly indicating the presence of a jet. At lower frequencies (e.g. 1.5 GHz, Leahy & Perley 1991) faint

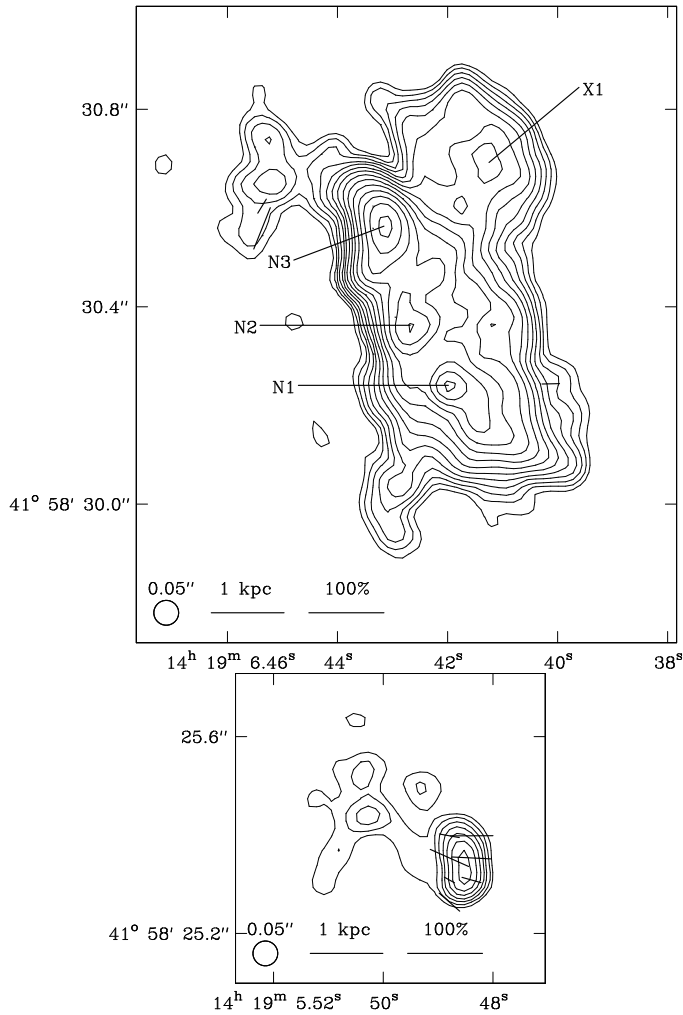


Figure 49. The hotspots of 3C 299 at 5 GHz and 0.05-arcsec resolution. Contours at $0.50 \times (-1, 1, \sqrt{2}, 2, \dots)$ mJy beam $^{-1}$. Above: Northern hotspot. The peak intensity is 49.7 mJy beam $^{-1}$. Below: Southern hotspot. The peak intensity is 4.68 mJy beam $^{-1}$.

wings can be seen close to the core suggesting backflow onto the central galaxy.

At 1.5-arcsec resolution, the northern lobe consists of a hotspot (N1), slightly recessed from the tip, sitting on a large region of uniform brightness; a fainter bridge of emission leads smoothly back to the core. At 0.225-arcsec resolution (Fig. 56) the structure in the northern lobe, including N1, is resolved out. The 5-GHz image of Bridle & Perley (1984) shows unresolved knots in the northern lobe suggestive of jet-like structure; however, such features are not visible in our 8-GHz images or the images presented by Leahy & Perley (1991).

At 1.5-arcsec resolution the southern lobe is also of approximately uniform brightness along its entire length with a slight rise before the diffuse hotspot (S1) at the tip. There is a bright knot of emission (S2) approximately a quarter of the way along the southern lobe. The higher-resolution image (Fig. 56) reveals that this feature is part of a jet-like trail of emission leading towards the southern hotspot

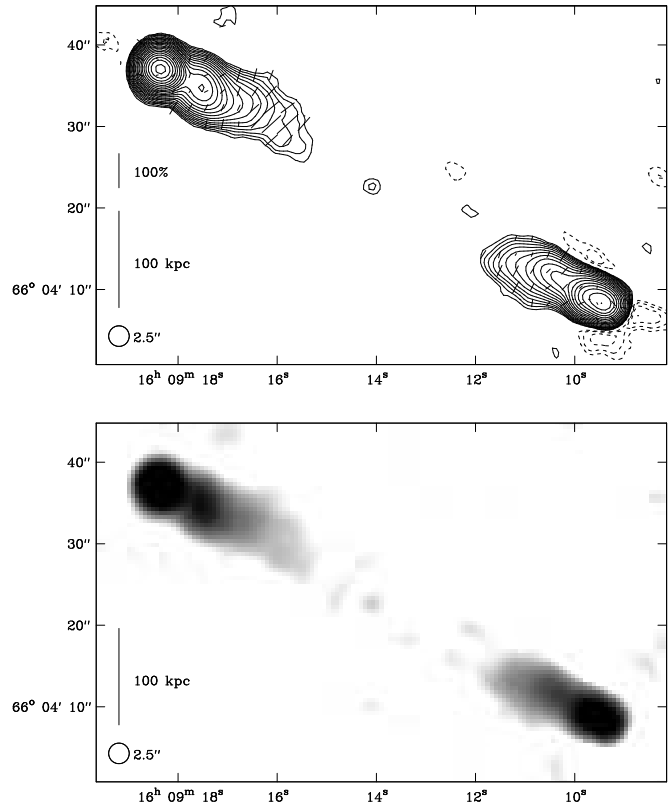


Figure 50. 3C 330 at 2.5-arcsec resolution. Contours at $0.400 \times (-2, -\sqrt{2}, -1, 1, \sqrt{2}, 2, \dots)$ mJy beam $^{-1}$. The peak intensity is 658 mJy beam $^{-1}$.

region; between the core and S2 there appear to be two strands to the jet. The hotspot S1 is resolved out.

3.24 3C 351

3C 351 is associated with a quasar. The northern lobe (N7) is faint, extended and substantially mis-aligned with the (presumed) beam axis (Fig. 57); unusually for an FR II source it has a uniform spectral index ($\alpha \sim 1.0$) across the lobe. At lower frequencies faint structure can be seen to the southeast of the core suggestive of a counterpart to this northern lobe. Kronberg, Clarke & van den Bergh (1980) presented VLA maps at 5 and 15 GHz which showed the diffuse and distorted lobes and they suggested interactions with a dense cluster IGM to explain the unusual structure; however, further investigations (e.g. Hutchings et al. 1996, Hardcastle et al. 2002) have failed to find any evidence for such a cluster.

A bright jet (N2; Fig. 58) is detected close to the nucleus. Following Bridle et al. (1994) the feature N1 is interpreted as a jet knot and the compact source to the southwest of N1 as the core. Bridle et al. (1994) note the possibility of a counter-jet detection to the southwest of the core and they also comment on another compact feature in the southern lobe half-way to the hotspot which they suggest could be part of a counter-jet – there is no evidence for these features in our images.

There is one very weak hotspot in the southern lobe which shows very little compact structure in the higher resolution image (Fig. 58).

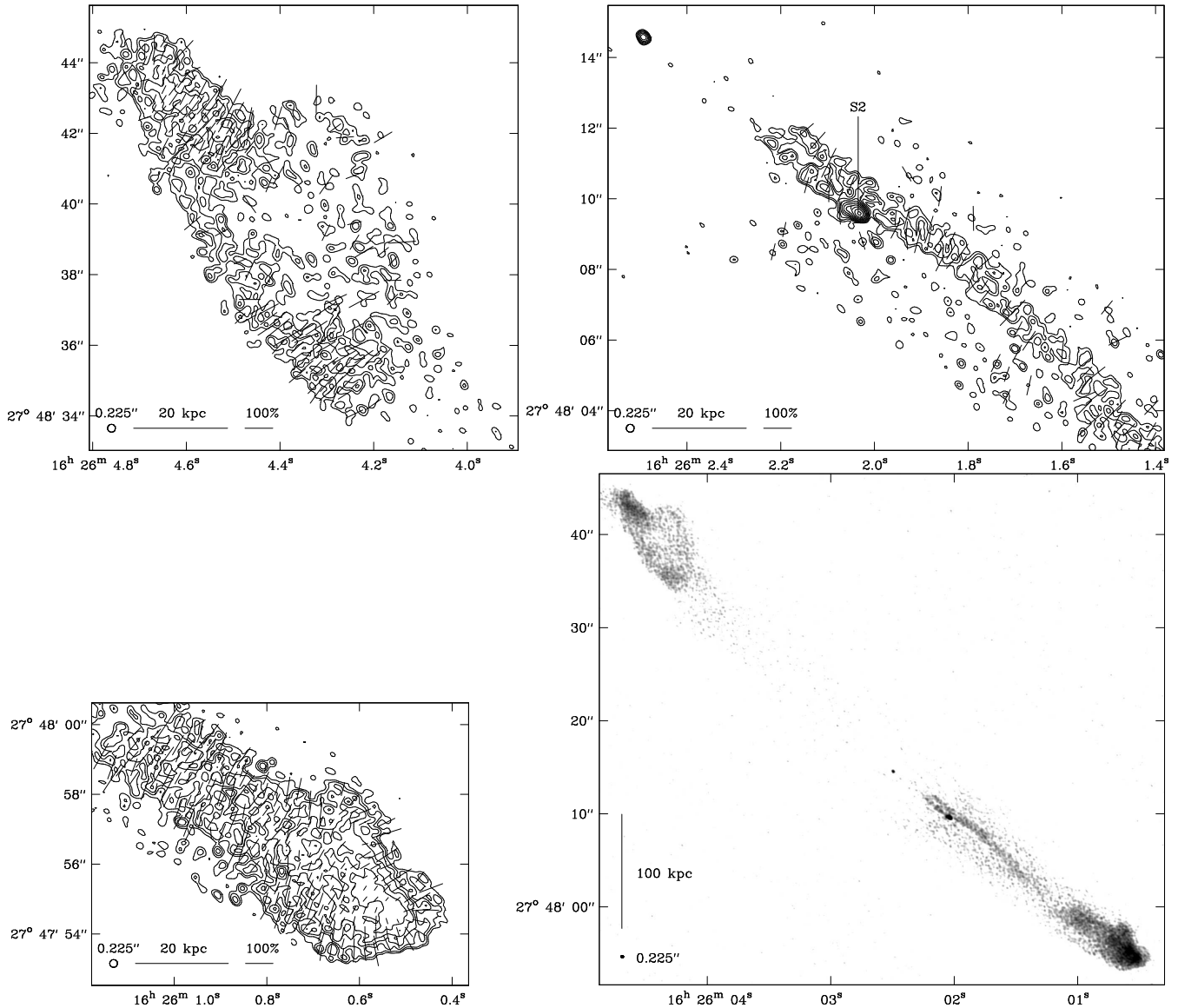


Figure 56. 3C 341 at 0.225-arcsec resolution. Contours at $0.085 \times (-1, 1, \sqrt{2}, 2, \dots)$ mJy beam^{-1} . Above left: Northern hotspot. The peak intensity is $0.338 \text{ mJy beam}^{-1}$. Above right: Southern jet. The peak intensity is $2.11 \text{ mJy beam}^{-1}$. Below left: Southern hotspot. The peak intensity is $0.673 \text{ mJy beam}^{-1}$. Below right: Whole source

The northern lobe is distinctive for its unusually prominent hotspot pair. Higher resolution images of this region (Fig. 58) show a complex, distorted morphology. Again following Bridle et al. (1994), we suggest that the compact feature N5 is the primary hotspot; it is connected to the inner jet and core by faint filamentary structure N3 (Fig. 57) and N4 (Fig. 58) which is also visible in the images of Bridle et al. The more relaxed structure (N6) is identified as a secondary hotspot. Both N5 and N6 have optical counterparts (Lähteenmäki & Valtaoja 1999). The synchrotron lifetime for optical electrons is shorter than the light travel time between the two components suggesting that they must be accelerated locally. Brunetti et al. (2001b) and Hardcastle et al. (2002) have detected X-rays from N5 and N6 with Chandra; Hardcastle et al. comment that this emission is

difficult to explain with a synchrotron self-Compton model and describe alternative models.

3.25 3C 427.1

The 1.5-GHz VLA image of 3C427.1 (Neff, Roberts & Hutchings 1995) shows bridge emission extending back to the associated galaxy. However the 0.45-arcsec and 0.25-arcsec images of 3C 427.1 at 8.4 GHz (Figs 61 and 62) appear very similar, both of them showing the northern and southern lobes extending only halfway back towards the core; this suggests that the bridge structure is of very low surface brightness at this frequency.

The northern lobe (Fig 61) shows a definite jet (N1 to N3) leading to a diffuse bright region (N4). The compact nature, and higher brightness of N3 leads to its classification

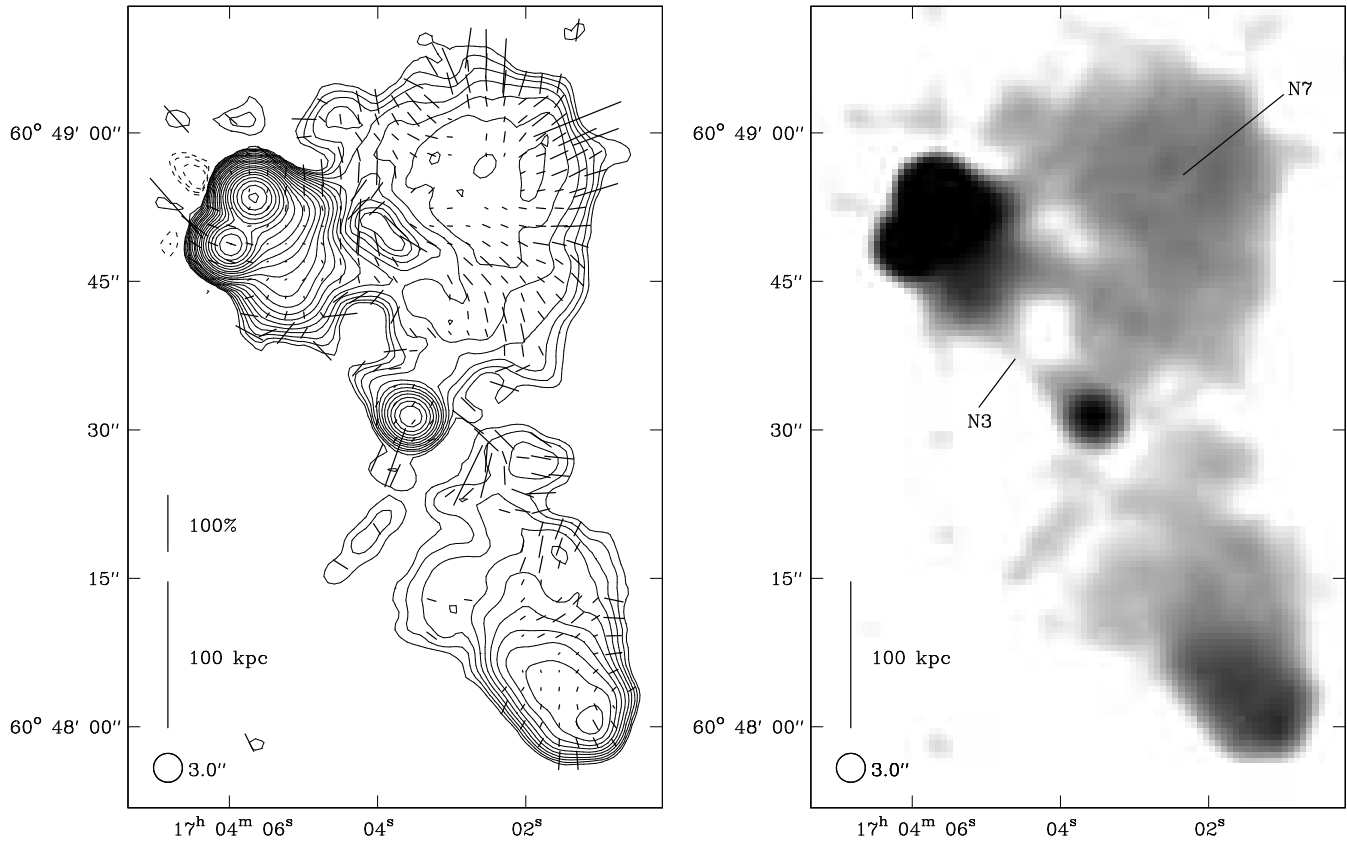


Figure 57. 3C 351 at 3.0-arcsec resolution. Contours at $0.200 \times (-2, -\sqrt{2}, -1, 1, \sqrt{2}, 2, \dots)$ mJy beam $^{-1}$. The peak intensity is 311 mJy beam $^{-1}$.

as the primary hotspot by many criteria, with N4 being a secondary hotspot. However, it is possible that N3 represents a jet knot and N4 a single diffuse hotspot. The jet is unusual in that it first appears over half-way to the lobe tip, after which it can be followed continuously to N3.

The southern lobe (Fig. 62) has an unusual structure. Bright components S1, S2 and S3 sit upon a larger lobe of relatively uniform brightness. As with the northern lobe it is difficult to provide a definitive hotspot classification. S1 is very compact and fits the criteria for the primary hotspot – its position in the lobe and its structure are very similar to that of N3 in the northern lobe; however, S2 and S3, which are further from the core, are also possible hotspot candidates. To the east of these components there is a distinct arc of emission (S4, S5) with a noticeable dip at X1.

3.26 3C 455

3C 455 is one of the smallest sources in the sample with an angular size of 3.9 arcsec, corresponding to a linear size of $D = 33$ kpc; it is associated with a quasar at a redshift of 0.543. The VLA A-configuration 5-GHz image is shown in Fig. 63. Unfortunately, due to an error on our part, the MERLIN observations of this source were not made. The lower frequency (1.4 GHz) observations of Akujor & Garrington (1995) show little difference from the 5-GHz image presented here.

A possible radio core is detected in the 8-GHz VLA observations of Bogers et al. (1994) at a position coincident

with the dip in emission between the two lobes. The position is close to the optical identification but slightly beyond the error limits given by LRL.

A faint ridge of emission leading from the core position towards the peak in the southern lobe could be identified as a jet. The higher-resolution 8-GHz image of Bogers et al. (1994) does not show any bridge emission and the jet-like feature appears more prominently. The stronger polarization of the southern lobe together with the possible jet detection strongly suggests that it is the closer lobe.

The image of Bogers et al. (1994) shows that the peak of emission in the northern lobe occurs close to the core. It may indicate the position of a recessed hotspot or bright jet knot.

3.27 3C 457

With a linear size of nearly 1500 kpc, 3C 457 is the largest source in the sample (Fig. 64). The lobe emission extends further back towards the core in lower-frequency images (e.g. 1.4 GHz, Leahy & Perley 1991) although it does not form a complete bridge. The image of Leahy & Perley also shows evidence for a jet about 30 arcsec in length extending from the core into the northern lobe.

The northern lobe displays a number of complex features (Fig. 65) with several distinct compact components. Its position at the tip of the lobe possibly makes N4 the most likely candidate for the primary hotspot, although N2 is slightly brighter and more compact. Faint trails of emis-

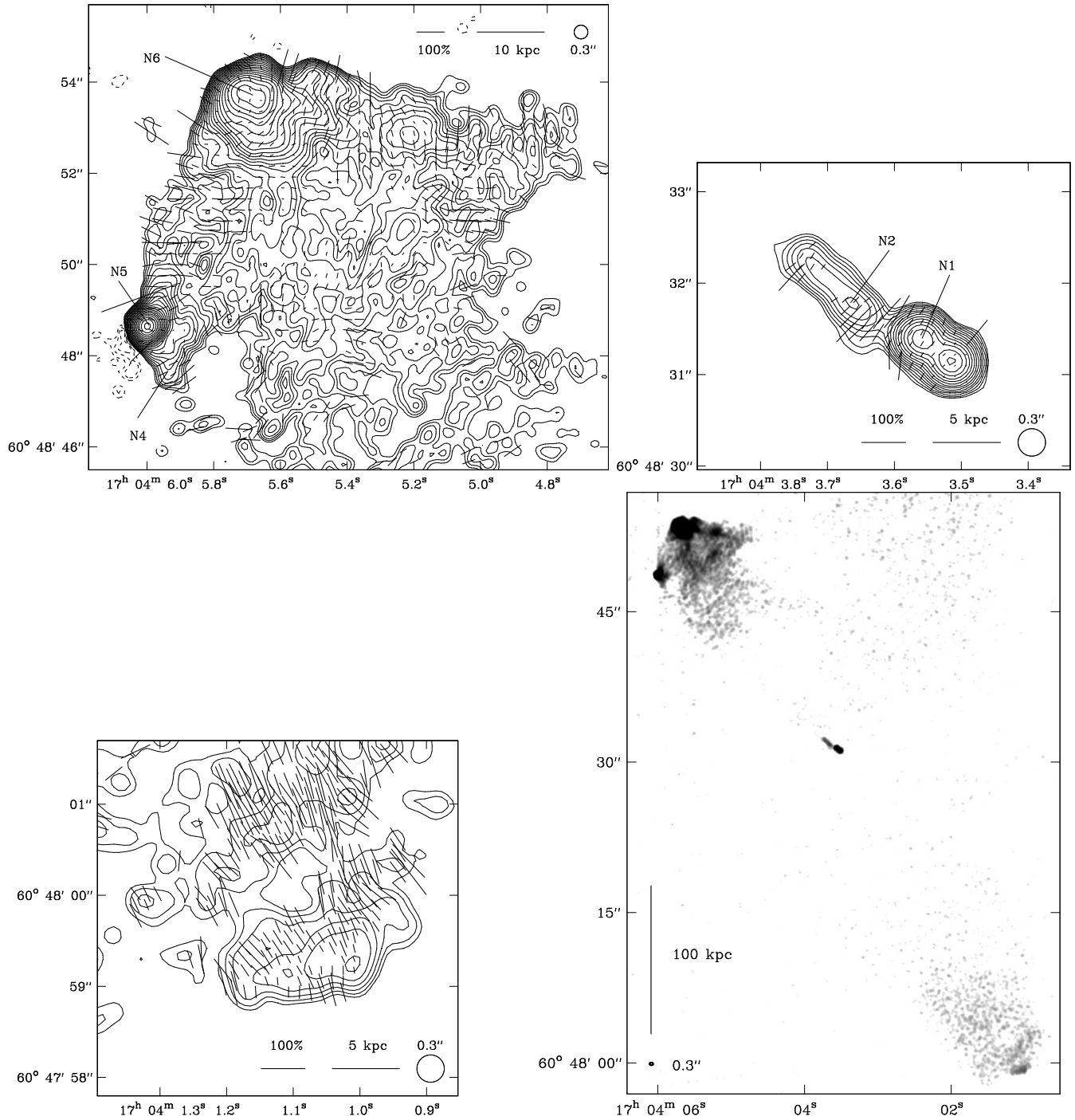


Figure 58. 3C 351 at 0.3-arcsec resolution. Contours at $0.060 \times (-2, -\sqrt{2}, -1, 1, \sqrt{2}, 2, \dots)$ mJy beam⁻¹. Top left: Northern hotspot. The peak intensity is 96.0 mJy beam⁻¹. Top right: Core and inner jet. The peak intensity is 5.78 mJy beam⁻¹. Bottom left: Southern hotspot. The peak intensity is 0.366 mJy beam⁻¹. Bottom right: Whole source.

sion link N1 and N2 to N3 and N4. The components are resolved out at 0.25-arcsec resolution. The polarization is unusually patchy with some regions of high polarization (~ 40 per cent) and some others which are unpolarized.

The southern lobe (Fig. 66) shows a more straightforward morphology with a compact primary hotspot at S1. A secondary hotspot at S2 leads to a small ridge of emission (S3) curving back in the direction of the core. Unlike

the components in the northern lobe, S1 and S2 are quite compact at 0.25-arcsec resolution (Fig. 66, below). As for the northern lobe, the polarization is very patchy with some unpolarized areas and some reaching 40 per cent or more in places.

The unresolved source X1 to the south of the southern hotspot is unpolarized and clearly separated from the main structure; it has a rising spectrum with a flux density of 5

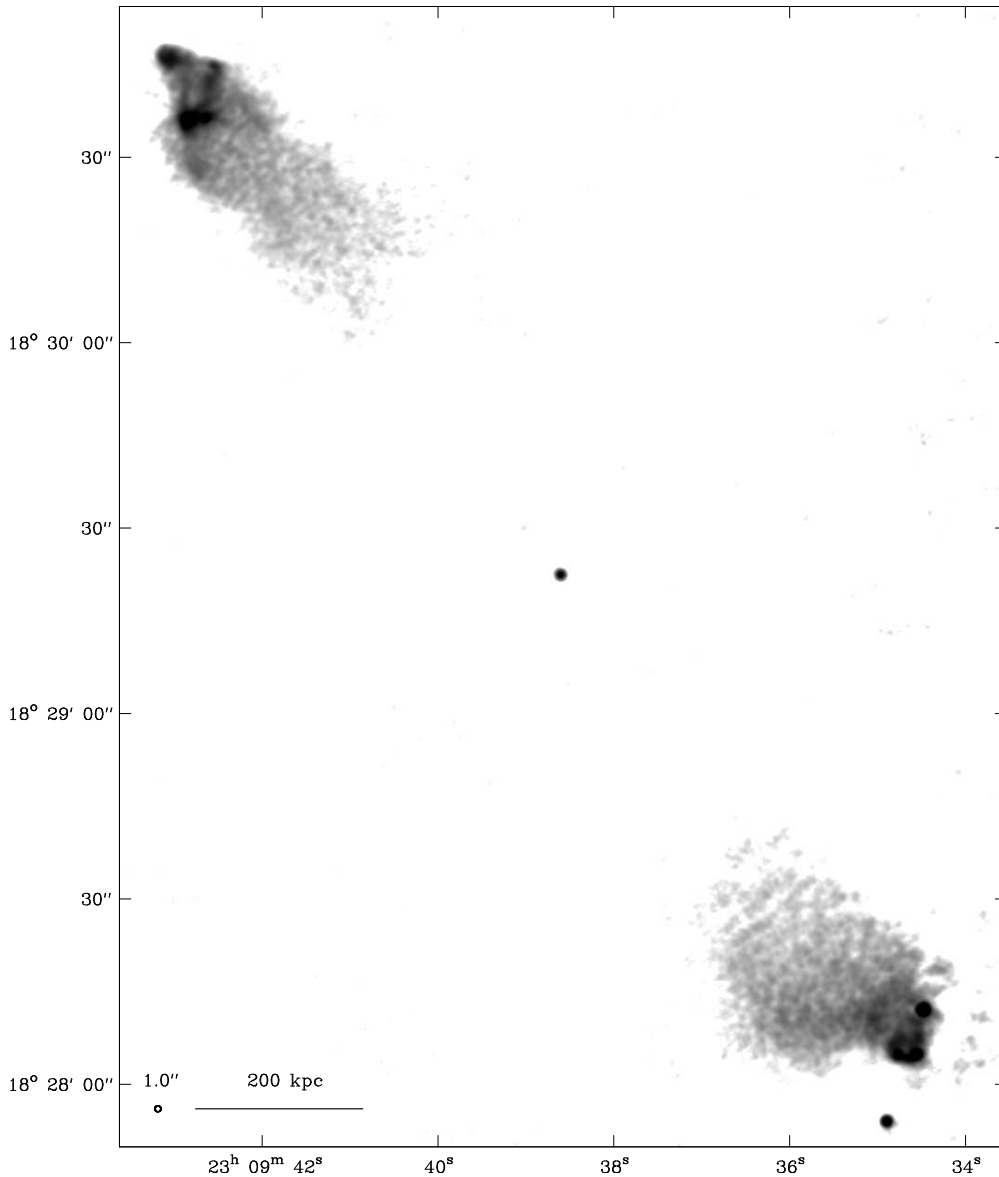


Figure 64. 3C 457 at 1.0-arcsec resolution. The peak intensity is $16.0 \text{ mJy beam}^{-1}$.

mJy at 1.5 GHz (Leahy & Perley 1991) and 6.7 mJy at 8.4 GHz. It is therefore most likely to be a background source.

4 DISCUSSION

27 sources have been mapped in detail, with a spatial resolution approaching 2 kpc in most cases; a summary of the properties of the hotspots and jets is given in Table 6. From the observations presented here, it is evident that the structures of both the lobes and the compact features they contain show some different trends from those of their lower-power and lower-redshift counterparts observed by B92, L97 and H97. A few qualitative comments on the properties of the current sample and comparisons with the lower-redshift samples are made here; quantitative analysis of the properties of the objects in all these samples will be carried out in later papers.

4.1 Lobes

The lobes in the 8-GHz images presented here are generally narrower than those in the lower-redshift samples. Also, in contrast with the lower-redshift sample, in a high proportion of the sources the emission at 8-GHz cannot be traced back to the central object and bridges and wings are not seen; this is, however, evidently a sensitivity limitation, since bridge emission shows up in the images at lower frequencies. This contrast between the low- and high-redshift samples is almost certainly a consequence of the known correlation between spectral index and radio power or redshift – the hotspots and lobes in the higher-redshift/higher power sources having steeper spectra, particularly at high frequencies (e.g. Laing & Peacock 1980, Blundell, Rawlings & Willott 1999). In several lobes (e.g. 3C 228 South) the hotspot lies at the edge of a large plateau of approximately constant brightness; there is an abrupt change in brightness on the edge closest to the core followed by another extensive lower-brightness plat-

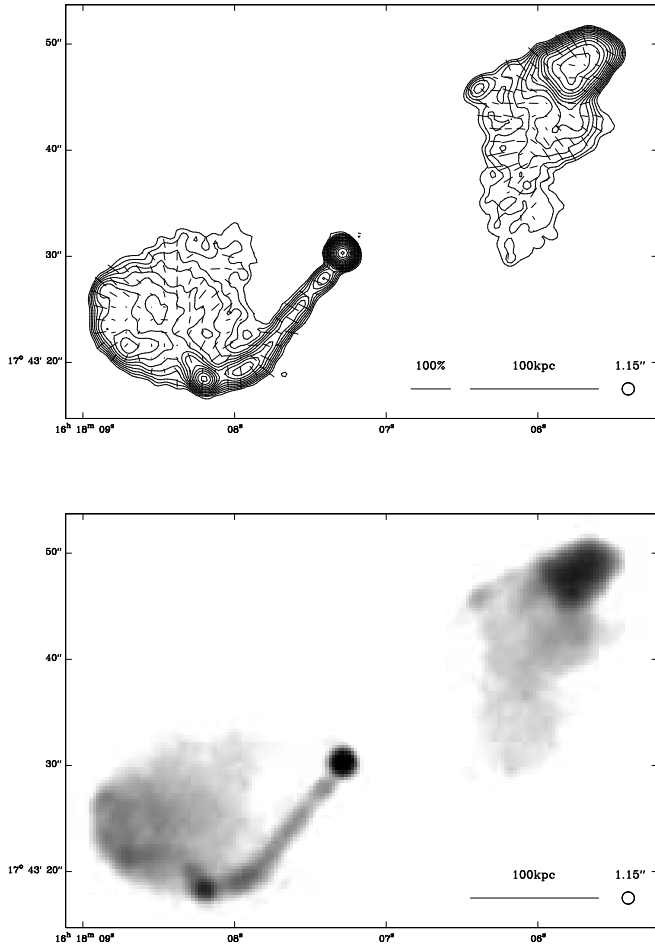


Figure 52. 3C 334 at 5 GHz and 1.15-arcsec resolution. Contours at $0.25 \times (-1, 1, \sqrt{2}, 2, \dots)$ mJy beam⁻¹. The peak intensity is 138 mJy beam⁻¹.

eau. With one exception (3C 349 North, H97), such structure is not seen in the lower-power sources of B92, L97 and H97. There are, in addition, several objects in the current sample with short high-brightness lobes which apparently fade to nothing very abruptly far from the core (e.g. 3C 172); these may also have this stepped-plateau structure with the low-brightness bridge falling below the noise level.

In most of the sources in the current sample the hotspots lie in regions which are comparable in width with the rest of the lobe, with the tips of the lobes being rounded and dominated by either the small region at the hotspot (e.g. 3C 42 South) or a wider structure the size of the lobe (e.g. 3C 47 North and South). By contrast, in the lower-power samples of B92, L97 and H97, there are a number of sources in which the hotspot occurs in a narrow region extending beyond the much wider lobe (e.g. 3C 132).

The lobes of the quasars in the current sample are generally wider and more distorted than those of the radio galaxies. Of the seven quasars in the sample one (3C 455) is poorly resolved, and only one (3C 47) has comparatively symmetric lobe structure. 3C 275.1 has no visible lobes at 8 GHz; it does have an extensive bridge at lower frequencies (Liu & Pooley 1990) but this has not been imaged with suffi-

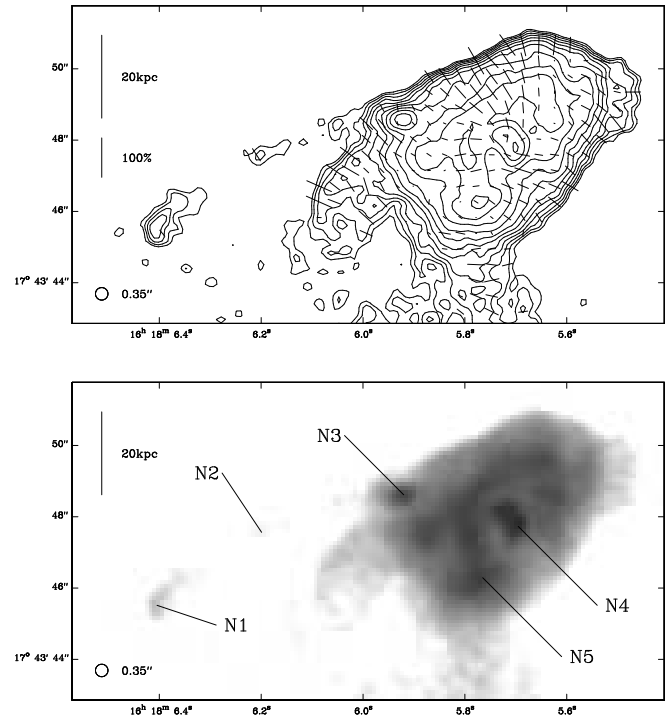


Figure 53. Northern lobe of 3C 334 at 5 GHz and 0.35-arcsec resolution. Contours at $0.0625 \times (-1, 1, \sqrt{2}, 2, \dots)$ mJy beam⁻¹. The peak intensity is 2.89 mJy beam⁻¹.

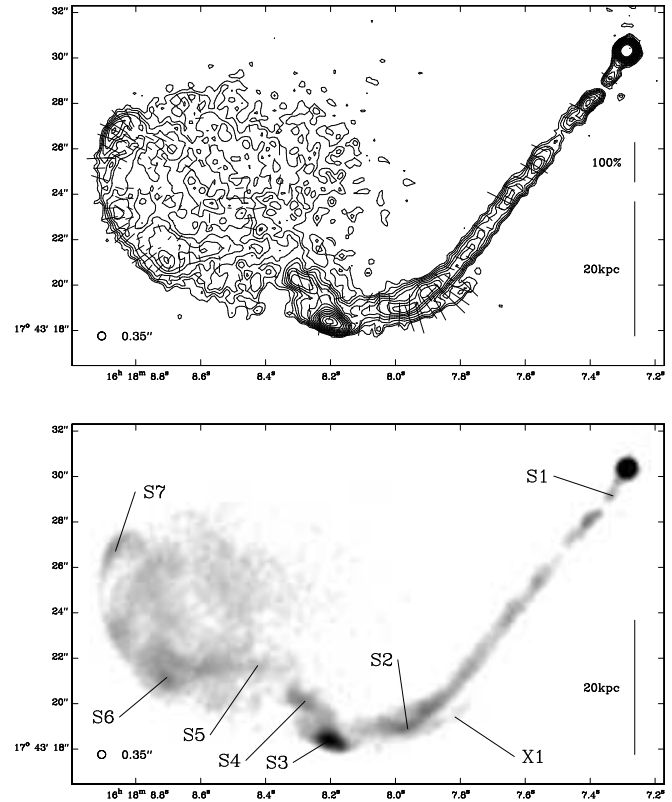


Figure 54. Southern lobe of 3C 334 at 5 GHz and 0.35-arcsec resolution. Contours at $0.0625 \times (-1, 1, \sqrt{2}, 2, \dots)$ mJy beam⁻¹. The peak intensity is 130 mJy beam⁻¹.

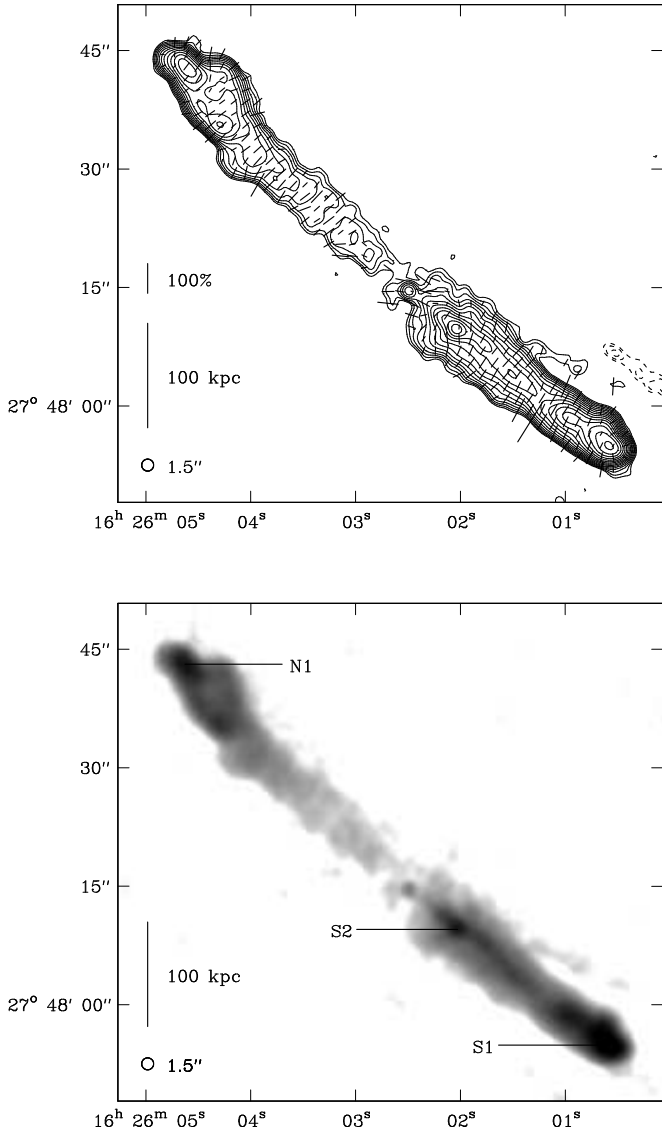


Figure 55. 3C 341 at 1.5-arcsec resolution. Contours at $0.120 \times (-2, -\sqrt{2}, -1, 1, \sqrt{2}, 2, \dots)$ mJy beam $^{-1}$. The peak intensity is 16.7 mJy beam $^{-1}$.

cient resolution to reveal its structure in detail. In 3C 215, 3C 249.1, 3C 334 and 3C 351 the lobes on the jet sides appear to have very similar structures, with large areas of relatively uniform brightness emission, offset from the jet and core – hotspot axes. On the other hand, the lobes on the counter-jet sides have comparatively normal structures with the brightest (hotspot) regions close to the lobe tips and the brightness decreasing rather more monotonically towards the cores. In 3C 215, 3C 249.1, 3C 275.1 and 3C 334 it is unclear which component on the jet side is the primary hotspot, but it is certainly not at the tip of the lobe. Although the numbers are small, it is striking that these unusual lobe structures occur in over 50 per cent of the quasars in the current sample and always on the jet side; if the observed distortions are solely due to projection effects it is difficult to understand why the counter-jet lobes should then have such a ‘normal’ appearance. (It is interesting to note that the lobe on the

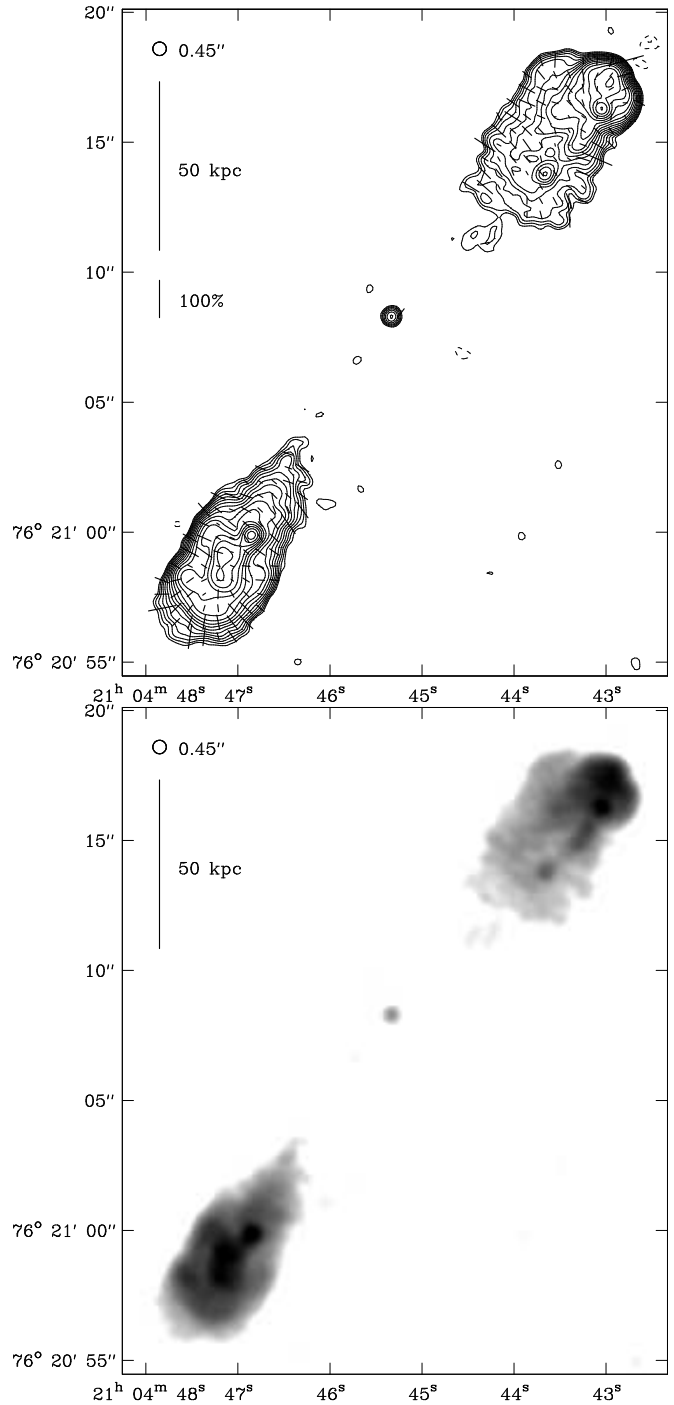


Figure 59. 3C 427.1 at 0.45-arcsec resolution. Contours at $0.095 \times (-\sqrt{2}, -1, 1, \sqrt{2}, 2, \dots)$ mJy beam $^{-1}$. The peak intensity is 21.4 mJy beam $^{-1}$.

jet side in 3C200, the only radio galaxy in the sample with a jet as prominent as those in the quasars 3C 215, 3C 249.1, 3C 334 and 3C 351, also has very similar properties.)

4.2 Jets

Jets which meet the criteria of Bridle & Perley (1984) are detected in 13 of the 27 sources (see Table 6), comparable with the fractions found by B92, L97 and H97. There are

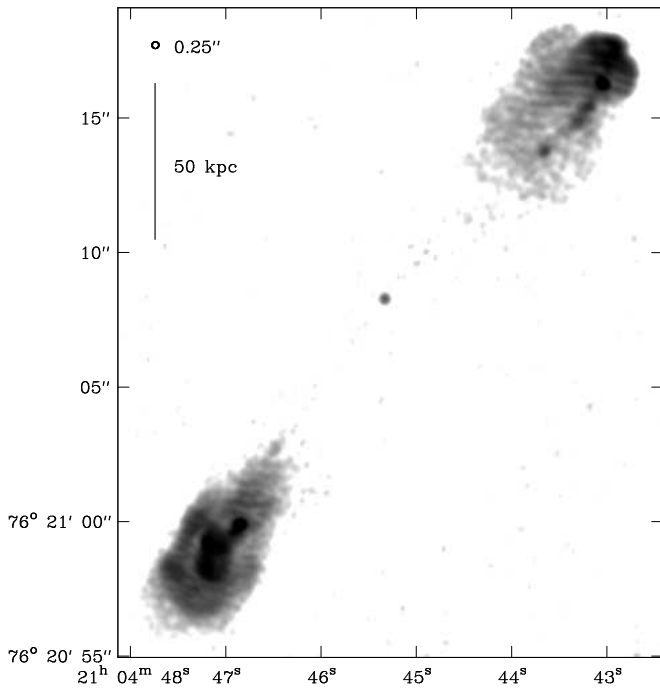


Figure 60. 3C 427.1 at 0.25-arcsec resolution.

four additional possible jet detections (see Table 6), giving an overall total of ~ 60 per cent definite and possible jet detections, compared to ~ 75 per cent in the other three samples. Analysis of these values is however complicated by the jet-like structure seen in the smallest sources which may be imaging artefacts (e.g. 3C 67) and by the statistically small sample size. Additionally, due to the increased distance, the lower spatial resolution of the present sample will reduce the observability of small-scale structure such as jets.

In the majority of sources with jets whose paths can be traced along most of the source extent (e.g. 3C 47, 3C 109, 3C 200, 3C 275.1, 3C 334) the jet structures are similar. Each jet appears to follow a straight path from the core to the end of the lobe where it bends sharply before terminating, often in a bright hotspot embedded on the side wall of the lobe. In no case in either the present sample or that of Bridle et al. (1994) does the jet follow a straight path from the core to the hotspot.

In two cases (3C 200 and 3C 334), at the point where the jet bends, a secondary jet-like structure is apparent on the outside edge of the bend. The reality of this feature in 3C 334 is confirmed since it is seen at different frequencies and epochs in images made by different authors; it is, however, far from clear how it is related to the structure and bending of the jet.

4.3 Hotspots

For comparison with L97 and H97 we have tabulated the positions and multiplicities of the hotspots in Table 6. We have attempted to use comparable classifications, as summarized in the notes to Table 6. In a number of objects the hotspots are resolved out in the full-resolution maps, as discussed in the notes on the individual sources; in these cases the hotspot region was classified at the highest resolution

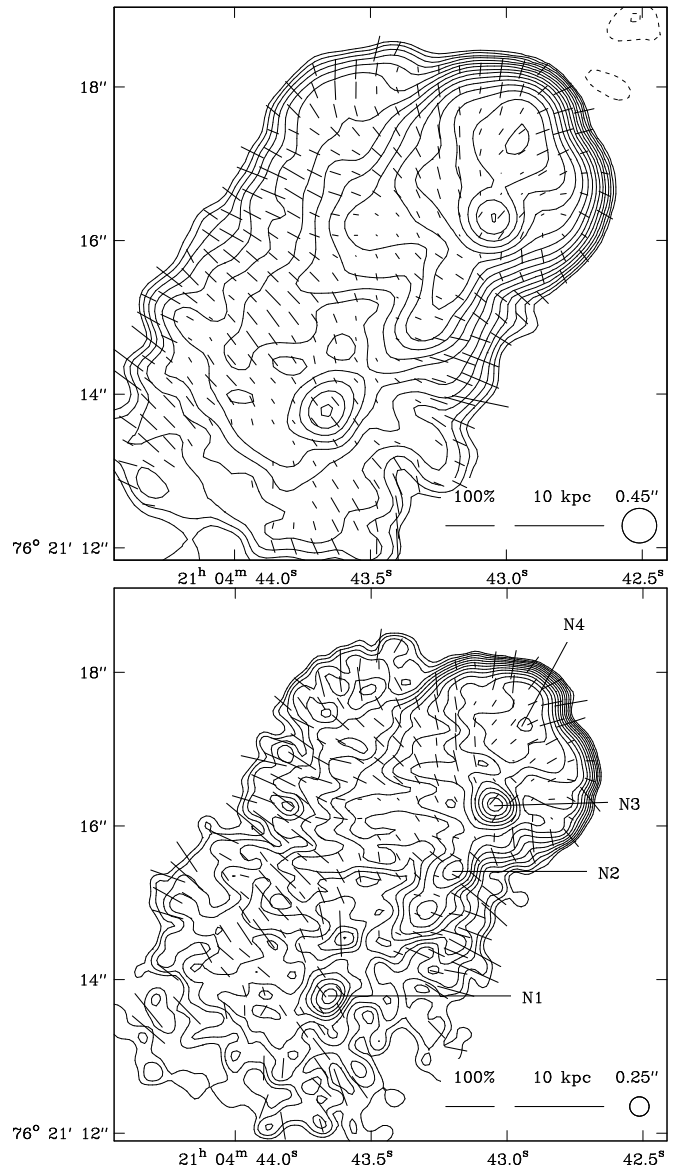


Figure 61. Northern tip of 3C 427.1. Above: At 0.45-arcsec resolution, contours at $0.095 \times (-\sqrt{2}, -1, 1, \sqrt{2}, 2, \dots)$ mJy beam^{-1} . The peak intensity is $17.5 \text{ mJy beam}^{-1}$. Below: At 0.25-arcsec resolution, contours at $0.070 \times (-1, 1, \sqrt{2}, 2, \dots)$ mJy beam^{-1} . The peak intensity is $11.0 \text{ mJy beam}^{-1}$.

for which at least one feature in the region has the defining properties of a hotspot. There are two lobes, 3C 16N and 3C 268.3S, which do not have hotspots according to the definitions used here; however, in both cases, the tip and edge of the lobe are edge brightened in a manner characteristic of FR II sources. There are no images of the quasar 3C 455 with sufficient resolution to distinguish the hotspots; here the tip of the southern lobe is edge brightened whilst the peak of the northern lobe lies in the middle of the lobe.

A wide variety of hotspot structures is observed across the sample. At high resolution most lobes (e.g. 3C 330 South) contain multiple compact bright regions and classification into just a primary and secondary hotspot is clearly inadequate. In some lobes (e.g. 3C 457 North) there are multiple termination points which appear to be linked; this

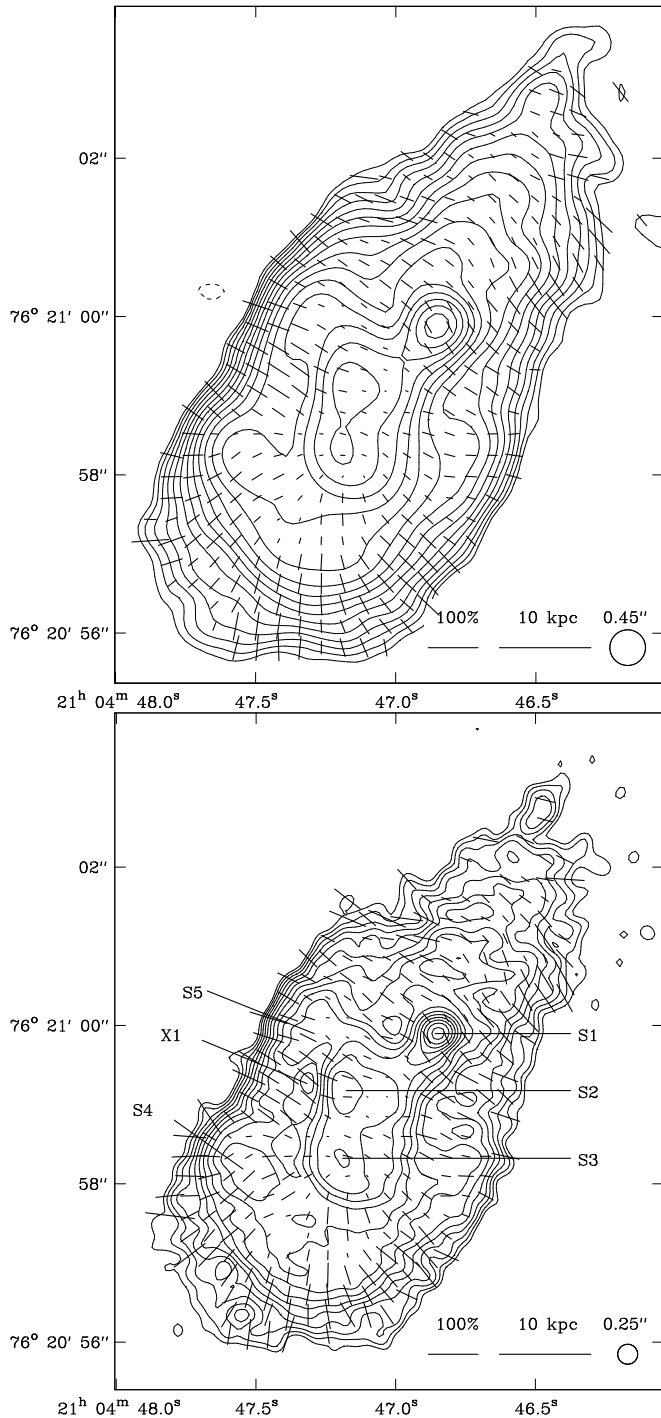


Figure 62. Southern tip of 3C 427.1. Above: At 0.45-arcsec resolution, contours at $0.095 \times (-\sqrt{2}, -1, 1, \sqrt{2}, \dots)$ mJy beam^{-1} . The peak intensity is $21.4 \text{ mJy beam}^{-1}$. Below: At 0.25-arcsec resolution, contours at $0.070 \times (-1, 1, \sqrt{2}, \dots)$ mJy beam^{-1} . The peak intensity is $15.5 \text{ mJy beam}^{-1}$.

may be a result of jet material being fed from one region to another (e.g. splatter-spots; Williams & Gull 1985) or a moving or discontinuous beam (e.g. Scheuer 1982; Cox, Gull & Scheuer 1991). A further class of structure is found in lobes such as 3C 19 South which show an extended region of uniform brightness bounded by a region of high brightness gradient and no evidence for any compact knots. Others

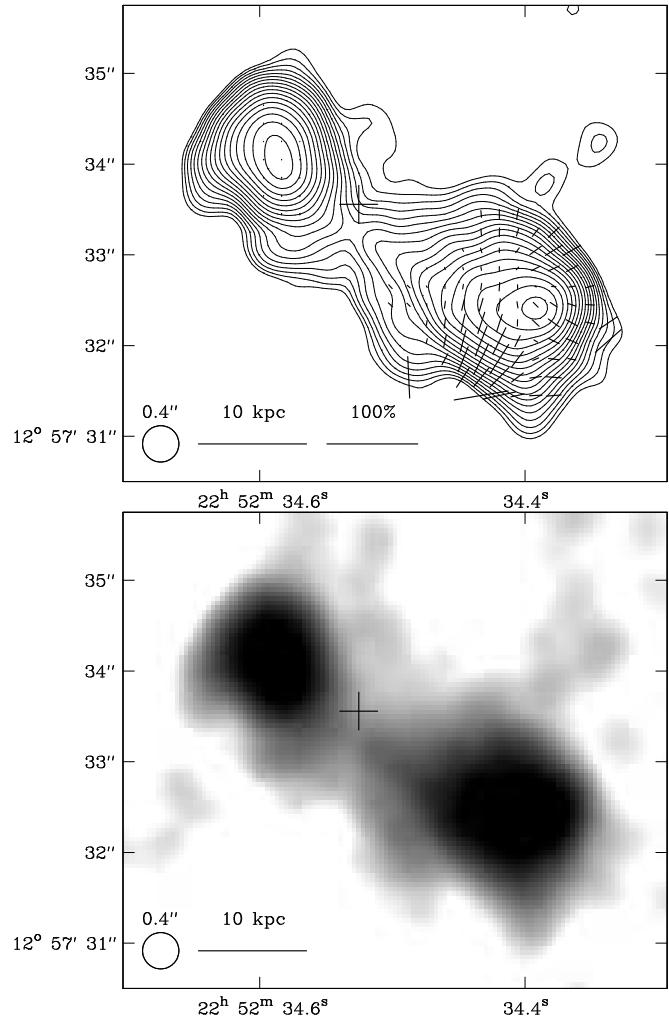


Figure 63. 3C 455 at 5 GHz and 0.4-arcsec resolution. Contours at $0.33 \times (-1, 1, \sqrt{2}, 2, \dots)$ mJy beam^{-1} . The peak intensity is $136 \text{ mJy beam}^{-1}$.

(e.g. 3C 341 North) show a weak hotspot at low resolution but no structure at all as the resolution is increased.

The observed position of hotspots within a lobe is indicated in Table 6. The standard model of a double radio source suggests that the hotspot should occur at the end of the lobe and mark the termination point of the beam and the region of lobe advance into the external medium. Many lobes (e.g. 3C 200 North) however show hotspots significantly recessed from the lobe edge and others (e.g. 3C 172 South) show compelling evidence for continuing outflow away from the core. Others (e.g. 3C 42 North, 3C 172 North) appear to have only a very narrow neck of emission attaching them to the main lobe. It can be seen from Table 6 that of the 50 lobes with hotspot regions, 40 are at the lobe tip and 10 are on the side or in the middle of the lobe (assuming that the knot in the middle of 3C 244.1 South is *not* a hotspot - see below). Five of the ten lobes with recessed hotspots are associated with quasars. This supports the evidence (Gilbert & Riley 1999) that broad-lined radio galaxies have hotspots which are very much more recessed than their narrow-lined counterparts, possibly indicating that the position of hotspots

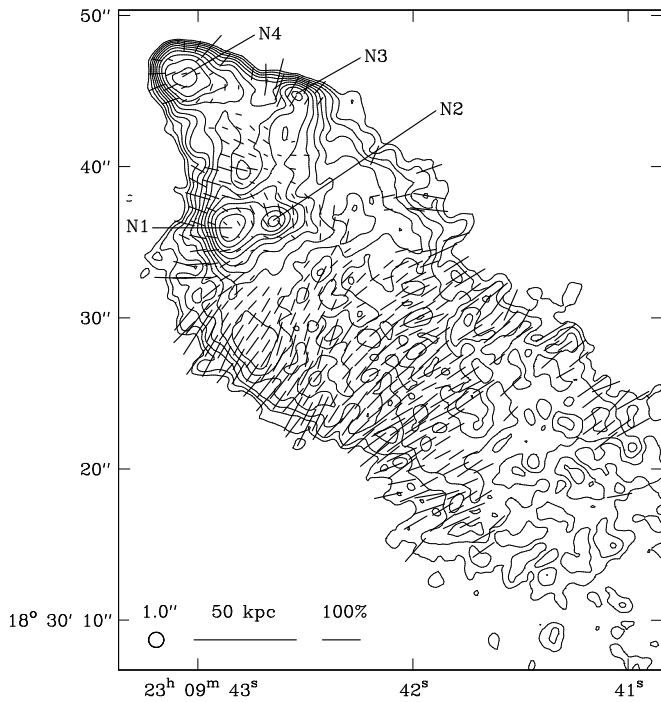


Figure 65. Northern tip of 3C 457 at 1.0-arcsec resolution. Contours at $0.060 \times (-1, 1, \sqrt{2}, 2, \dots)$ mJy beam $^{-1}$. The peak intensity is 3.83 mJy beam $^{-1}$.

in the lobes is orientation dependent. In this context it is again interesting to note that the narrow-lined radio galaxy 3C 200, which has a one-sided jet as prominent as that of the quasars, also has recessed hotspots.

In three lobes (3C 427.1 North and South and 3C 244.1 South) a strongly polarized unresolved bright region is observed. These points all lie on the lobe axis and would be classified as hotspots apart from the fact that they are considerably recessed from the lobe tip with more likely candidates appearing towards the end. The number observed, their position and their polarization make it unlikely that they are background sources; equally it is not clear that they can be classified as jet knots as they are neither elongated along the source axis nor are they polarized either parallel or perpendicular to the axis. Their classification is therefore somewhat uncertain. Similar knots are observed in the powerful radio galaxy 3C 294 (McCarthy et al. 1990) which also has hotspots at the ends of the lobes; in this case, however, the knots are slightly extended along the source axis. They occur near the edge of an extended Ly α cloud surrounding the source and McCarthy et al. suggest that they may result from the sudden changes in the surroundings.

ACKNOWLEDGMENTS

GMG and JC acknowledge studentships from the UK Particle Physics and Astronomy Research Council (PPARC); MJH thanks the Royal Society for a research fellowship. We are grateful to Beverley Wills and Paddy Leahy for giving us VLA uv data obtained for other programs, to Debora Katz-Stone and Rick Perley for supplying the 8-GHz VLA images of 3C 67 and 3C 295 respectively, to Everton

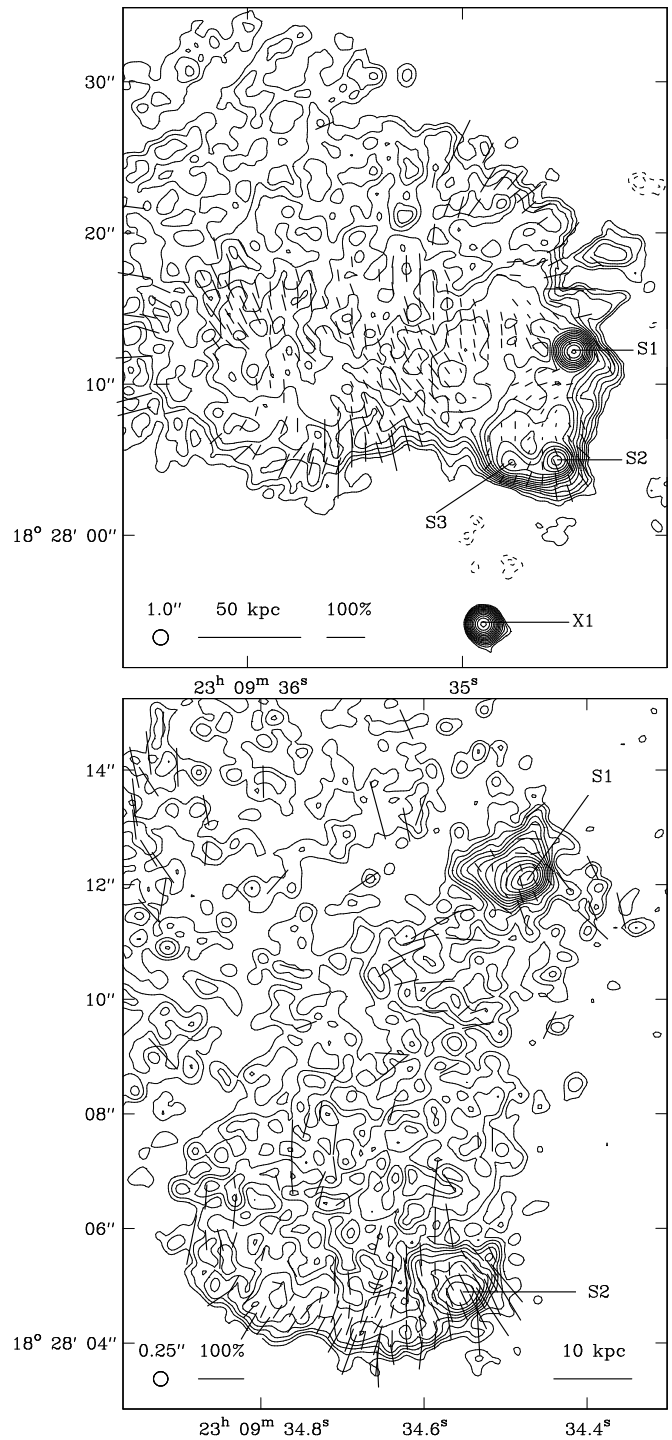


Figure 66. Southern tip of 3C 457. Above: At 1.0-arcsec resolution, contours at $0.060 \times (-\sqrt{2}, -1, 1, \sqrt{2}, 2, \dots)$ mJy beam $^{-1}$. The peak intensity is 16.0 mJy beam $^{-1}$. Below: At 0.25-arcsec resolution, contours at $0.060 \times (-1, 1, \sqrt{2}, 2, \dots)$ mJy beam $^{-1}$. The peak intensity is 4.84 mJy beam $^{-1}$.

Table 6. Hotspots and jets

Lobe	Type	Location	Comment	Jet?
3C 16N	0		tip and side of lobe edge brightened	Y?
3C 16S	1	tip	diffuse	Y?
3C 19N	1	tip	tail	Y?
3C 19S	2	tip	primary at side	Y?
3C 42N	2+1	tip	nearly equal size and brightness	
3C 42S	1	tip		
3C 46N	1+M	tip		
3C 46S	2	tip	recessed secondary	
3C 47N	1	tip	extended	
3C 47S	1+1	tip	jet enters hotspot; primary at side	Y
3C 67N	2	tip	recessed primary	
3C 67S	1	tip	extended; at side	
3C 109N	1	tip	slightly recessed primary	
3C 109S	1+1	tip	jet enters primary? primary at side	Y
3C 172N	1	tip		
3C 172S	1+2	tip	rim	
3C 200N	1	middle	extended	Y?
3C 200S	1	middle	diffuse	Y
4C 14.27N	1	tip	diffuse	
4C 14.27S	1	tip	diffuse	
3C 215N	1	middle	diffuse	Y?
3C 215S	1?	side?	FR I-like lobe? jet enters hotspot?	Y
3C 225BN	2	tip	recessed primary?	Y?
3C 225BS	1	tip		Y?
3C 228N	1	tip	extended	
3C 228S	2	tip	one hotspot could be jet knot	Y
3C 244.1N	2	tip	secondary recessed?	
3C 244.1S ^a	2	tip	secondary recessed?	
	1	middle	hotspot or jet knot?	
3C 249.1E	1?	side	FR I-like lobe? jet enters hotspot?	Y
3C 249.1W	1	tip	diffuse and recessed	
3C 268.3N ^b	2	middle		
3C 268.3S ^b	0		tip and side of lobe edge brightened	
3C 274.1N	1	tip	recessed	
3C 274.1S	2	tip	diffuse; recessed secondary?	
3C 275.1N	1?+M?	middle	hotspot or jet knot? jet enters hotspot?	Y
3C 275.1S	1+1	middle	extended	Y?
3C 295N ^c	2	tip		
3C 295S ^c	1	side	diffuse	
3C 299N	M	tip	hotspots or jet knots?	
3C 299S	1	tip	extended	
3C 330N	1	tip	extended	
3C 330S	M	tip		
3C 334N	2	tip	hotspot or jet knot at side? diffuse, recessed secondary?	Y?
3C 334S	1+M	tip	rim; primary at side; jet enters hotspot	Y
3C 341N	1	tip	very diffuse	
3C 341S	1	tip	very diffuse	Y
3C 351N	2+M	tip	primary at side; jet enters hotspot?	Y
3C 351S	1	tip	diffuse	
3C 427.1N	2	tip	recessed primary or jet knot? jet enters hotspot?	Y
3C 427.1S	M	middle	recessed primary or jet knot?	
3C 455N				
3C 455S ^d				Y
3C 457N ^e	M+1	tip	recessed secondaries, primary or jet knots?	Y
3C 457S	2	tip	primary at side	

Column 2: Hotspot class – 1 (single), 2 (double) or M (multiple); components 10 times fainter than the peak brightness of the hotspot complex are counted after a plus sign, so that ‘2+1’ means ‘double with an additional faint component’. Column 3: Location of the hotspot complex – tip (at the very end of the lobe), side (on the lobe boundary but not at the end) or middle (anywhere else in the lobe). Column 4: Comments – diffuse (little compact structure at the resolution of the map used), extended (bright hotspot which is significantly extended), rim (multiple hotspots forming a bright rim); other comments are self-explanatory. Column 5: Jet detection – Y (definite jet), Y? (possible jet)

^a See notes.

^b Classification made from images by Fanti et al. (1985).

^c Classification made from images by Perley & Taylor (1991).

^d Jet detected in image by Leahy & Perley (1991).

^e Jet detected in image by Bogers et al. (1994)

Lüdke for supplying the 5-GHz MERLIN image of 3C 268.3 and to Tom Muxlow for help with MERLIN data reduction. The National Radio Astronomy Observatory is operated by Associated Universities Inc., under cooperative agreement with the National Science Foundation. MERLIN is operated by the University of Manchester on behalf of PPARC. This project made use of STARLINK facilities. This research has made use of the NASA/IPAC Extragalactic Database (NED) which is operated by the Jet Propulsion Laboratory, California Institute of Technology, under contract with the National Aeronautics and Space Administration.

REFERENCES

- Akujor C. E., Garrington S. T., 1995, *A&AS*, 112, 235
 Akujor C. E., Spencer R. E., Wilkinson P. N., 1990, *MNRAS*, 244, 362
 Akujor C. E., Lüdke, E., Browne I. W. A., Leahy J. P., Garrington S. T., Jackson N., Thomasson P., 1994, *A&AS*, 105, 247
 Antonucci R. R. J., 1985, *ApJS*, 59, 499
 Bennett A. S., 1962, *MemRAS*, 68, 163
 Black A. R. S., Baum S. A., Leahy J. P., Perley R. A., Riley J. M., Scheuer P. A. G., 1992, *MNRAS*, 256, 186 (B92)
 Blundell K. M., Rawlings S., Willott C. J., 1999, *AJ*, 117, 677
 Bogers W. J., Hes R., Barthel P. D., Zensus J. A., 1994, *A&AS*, 105, 91
 Bridle A. H., Perley R. A., 1984, *ARAA*, 22, 319
 Bridle A. H., Hough D. H., Lonsdale C. J., Burns J. O., Laing R. A., 1994, *AJ*, 108, 766
 Brunetti G., Cappi M., Setti G., Feretti L., Harris D. E., 2001a, *A&A*, 372, 755
 Brunetti G., Bondi M., Comastri A., Pedani M., Varano S., Setti G., Hardcastle M. J., 2001b, *ApJ*, 561, 157
 Burns, J. O., Basart J. P., De Young D. S., Ghiglia D. C., 1984, *ApJ*, 283, 515
 Carilli C. L., Perley R. A., Dreher J. M., Leahy J. P., 1991, *ApJ*, 383, 554
 Carilli C. L., Kurk J. D., van der Werf P. P., Perley R. A., Miley G. K., 1999, *AJ*, 118, 2581
 Cox C. L., Gull S. F., Scheuer P. A. G., 1991, *MNRAS*, 252, 558
 Crawford C. S., Fabian A. C., 2003, *MNRAS*, 339, 1163
 Crawford C. S., Fabian A. C., Johnstone R. M., 1988, *MNRAS*, 235, 183
 de Koff S., Baum S. A., Sparks W. B., Biretta J., Golombek D., Macchetto F., McCarthy P., Miley G. K., 1996, *ApJS*, 107, 621
 Dennett-Thorpe J., 1996, Ph. D. Thesis, University of Cambridge
 Ellington E., Yee H. K. C., Green R. F., 1991, *ApJ*, 371, 49
 Fanaroff B., Riley, J. M., 1974, *MNRAS*, 167, 31P
 Fanti C., Fanti R., Parma P., Schilizzi R. T., van Breugel W. J. M., 1985, *A&A*, 143, 292
 Fernini I., 2001, *AJ*, 122, 83
 Fernini I., 2002, *AJ*, 123, 132
 Fernini I., Burns J. O., Perley R. A., 1997, *AJ*, 114, 2292
 Fernini I., Burns J. O., Leahy, J. P., Basart J. P., 1991, *ApJ*, 381, 63
 Garrington S. T., Conway R. G., Leahy J. P., 1991, *MNRAS*, 250, 171
 Garrington S. T., Leahy J. P., Conway R. G., Laing R. A., 1988, *Nat*, 331, 147
 Gilbert G. M., Riley J. M., 1999, *MNRAS*, 309, 681
 Giovannini G., Feretti L., Venturi T., Lara L., Marcaide J., Rioja M., Spangler S. R., Wehrle A. E., 1994, *ApJ*, 435, 116
 Hardcastle M. J., Worrall D. M., 1999, *MNRAS*, 309, 969
 Hardcastle M. J., Alexander P., Pooley G. G., Riley J. M., 1997, *MNRAS*, 288, 859 (H97)
 Hardcastle M. J., Alexander P., Pooley G. G., Riley J. M., 1999, *MNRAS*, 304, 135
 Hardcastle M. J., Birkinshaw, M., Cameron, R. A., Harris, D. E., Looney, L. W., Worrall D. M., 2002, *ApJ*, 581, 948
 Harris D. E. et al. , 2000, *ApJ*, 530, L81
 Harvanek M., Hardcastle M. J., 1998, *ApJS*, 119, 25
 Hintzen P., 1984, *ApJS*, 55, 533
 Hintzen P., Boeshaar G. O., Scott J. S., 1981, *ApJ*, 246, L1
 Hough D. H., Readhead A. C. S., Wood D. A. Jr., Feldmeier J. J., 1992, *ApJ*, 393, 81
 Hutchings J. B., Gower A. C., Ryneveld S., Dewey A., 1996, *AJ*, 111, 2167
 Jenkins C. J., Scheuer P. A. G., 1976, *MNRAS*, 174, 327
 Jenkins C. J., Pooley G. G., Riley J. M., 1977, *MemRAS*, 84, 61
 Kaiser C. R., Alexander, P., 1997, *MNRAS*, 286, 215
 Komissarov, S. S., Falle S. A. E. G., 1998, *MNRAS*, 297, 1087
 Krause, M., 2003, *A&A*, 398, 113
 Kronberg P. P., Clarke J. N., van den Bergh S., 1980, *AJ*, 85, 973
 Lähteenmäki A., Valtaoja E., 1999, *AJ*, 117, 1168
 Laing R. A., 1981, *ApJ*, 248, 87
 Laing R. A., 1988, *Nat*, 331, 149
 Laing R. A., 1989, in Meisenheimer K., Röser H. -J., eds, *Hotspots in Extragalactic Radio Sources*. Springer-Verlag, Heidelberg, p. 27
 Laing R. A., Peacock, J. A., 1980, *MNRAS*, 190, 903
 Laing R. A., Riley J. M., Longair M. S., 1983, *MNRAS*, 204, 151 (LRL)
 Laing R. A., Jenkins C. R., Wall J. V., Unger S. W., 1994, in Bicknell G. V., Dopita M. A., Quinn P. J., eds, *ASP Conf.Ser.Vol.54, The First Stromlo Symposium: The Physics of Active Galaxies*. Astron. Soc. Pac., San Francisco, p. 201
 Leahy J. P., 1996, *Vistas Astr.*, 40, 173
 Leahy J. P., Perley R. A., 1991, *AJ*, 102, 527
 Leahy J. P., Williams A. G., 1984, *MNRAS*, 210, 929
 Leahy J. P., Pooley G. G., Riley J. M., 1986, *MNRAS*, 222, 753
 Leahy J. P., Muxlow T. W. B., Stephens P. W., 1989, *MNRAS*, 239, 401
 Leahy J. P., Bridle A. H., Strom R. G., 2000, *DRAGN Atlas*, <http://www.jb.man.ac.uk/atlas>
 Leahy J. P., Black A. R. S., Dennett-Thorpe J., Hardcastle M. J., Komissarov S., Perley R. A., Riley J. M., Scheuer P. A. G., 1997, *MNRAS*, 291, 20 (L97)
 Liu R., Pooley G. G., 1990, *MNRAS*, 245, 17
 Liu R., Pooley G. G., 1991, *MNRAS*, 253, 669
 Lonsdale C. J., Morison I., 1983, *MNRAS*, 203, 803
 Lüdke, E., Garrington S. T., Spencer R. E., Akujor C. E., Muxlow T. W. B., Sanghera H. S., Fanti C., 1998, *MNRAS*, 299, 467
 McCarthy P. J., Spinrad H., van Breugel W., 1995, *ApJS*, 99, 27
 McCarthy P. J., Spinrad H., van Breugel W., Liebert, J., Dickinson, M., Djorgovski, S., Eisenhardt, P., 1990, *ApJ*, 365, 487
 Muxlow T. W. B., Garrington S. T., 1991, in Hughes P. A., ed., *Beams and Jets in Astrophysics*. Cambridge Univ. Press, Cambridge, p. 52
 Neff S. G., Roberts L., Hutchings J. B., 1995, *ApJS*, 99, 349
 Pearson, T. J., Readhead A. C. S., Perley, R. A., 1985, *AJ*, 90, 738
 Perley R. A., 1989, in Meisenheimer K., Röser H. -J., eds, *Hotspots in Extragalactic Radio Sources*. Springer-Verlag, Heidelberg, p. 1
 Perley R. A., Taylor G. B., 1991, *AJ*, 101, 1623
 Reynolds, C. S., Heinz, S., Begelman, M. C., 2002, *MNRAS*, 332, 271
 Riley J. M., Pooley G. G., 1975, *MemRAS*, 80, 105
 Sanghera, H. S., Saikia, D. J., Lüdke E., Spencer R. E., Foulsham P. A., Akujor C. E., Tzioumis A. K., 1995, *A&A*, 295, 629
 Saxton, C. J., Sutherland, R. S., Bicknell, G. V., Blanchet, G. F., Wagner, S. J., 2002, *A&A*, 393, 765

- Scheuer P. A. G., 1982, in Heeschen D. S., Wade C. M., eds, IAU Symposium 97, Extragalactic Radio Sources. Reidel, Dordrecht, p. 163
- Schoenmakers A. P., de Bruyn A. G., Röttgering H. J. A., van der Laan H., Kaiser C. R., 2000, MNRAS, 315, 371
- Simard-Normandin M., Kronberg P. P., Button S., 1981, ApJS, 45, 97
- Simmons J. F. L., Stewart B. G., 1985, A&A, 142, 100
- Spencer R. E., Muxlow T. W. B., Schilizzi R. T., Fanti C., Fanti R., Parma P., van Breugel W. J. M., Venturi T., Muxlow T. W. B., Rendong Nan, 1991, MNRAS, 250, 225
- Spinrad H., Marr, J., Aguilar L., Djorgovski S., 1985, PASP, 97, 932
- Stoche J. T., Burns J. O., Christiansen W. A., 1985, ApJ, 299, 799
- Stockton A., MacKenty J. W., 1983, Nat, 305, 678
- Strom R. G., Riley, J. M., Spinrad H., van Breugel W. J. M., Djorgovski S., Liebert J., McCarthy P. J., 1990, A&A, 227, 19
- Taylor G. B., Perley R. A., 1992, A&A, 262, 417
- van Breugel W. J. M., Miley G., Heckman T., 1984, AJ, 89, 5
- van Breugel W. J. M., Fanti C., Fanti R., Stanghellini C., Schilizzi R. T., Spencer R. E., 1992, A&A, 256, 56
- Vermeulen R. C., Bernstein R. A., Hough D. H., Readhead A. C. S., 1993, AAS, 182, 5302
- Williams A. G., Gull S.F., 1985, Nat, 313, 34

This paper has been produced using the Royal Astronomical Society/Blackwell Science L^AT_EX style file.